

Doctoral theses at NTNU, 2021:366

Olav Rømcke

# Colliding jamming fronts in a dense suspension

ISBN 978-82-326-6114-5 (printed ver.)  
ISBN 978-82-326-6812-0 (electronic ver.)  
ISSN 1503-8181 (printed ver.)  
ISSN 2703-8084 (electronic ver.)

Doctoral theses at NTNU, 2021:366

**NTNU**  
Norwegian University of  
Science and Technology  
Thesis for the degree of  
Philosophiae Doctor  
Faculty of Engineering  
Department of Energy and Process Engineering

 **NTNU**  
Norwegian University of  
Science and Technology

 NTNU

 **NTNU**  
Norwegian University of  
Science and Technology

Olav Rømcke

# Colliding jamming fronts in a dense suspension

Thesis for the degree of Philosophiae Doctor

Trondheim, November 2021

Norwegian University of Science and Technology  
Faculty of Engineering  
Department of Energy and Process Engineering



Norwegian University of  
Science and Technology

**NTNU**

Norwegian University of Science and Technology

Thesis for the degree of Philosophiae Doctor

Faculty of Engineering

Department of Energy and Process Engineering

© Olav Rømcke

ISBN 978-82-326-6114-5 (printed ver.)

ISBN 978-82-326-6812-0 (electronic ver.)

ISSN 1503-8181 (printed ver.)

ISSN 2703-8084 (electronic ver.)

Doctoral theses at NTNU, 2021:366



Printed by Skipnes Kommunikasjon AS

# Abstract

Mixtures of liquids and solid particles, known as suspensions, are a quite common material both in natural and industrial processes. For a high concentration of particles, some of these mixtures exhibit a quite remarkable phenomenon whereby they act liquid-like when perturbed lightly, but presents impressive resistance when exposed to an impact or otherwise large stress. In the extreme case, flow is arrested and the material appears solid-like, a phenomenon known as dynamic jamming. The last decade has seen significant progress in our understanding of how the material transitions between these two states. Probably the most famous example of such a material is a cornstarch and water suspension; this stress induced jamming explains how it is possible to stay afloat while running across a cornstarch suspension. The transient development of the solid-like state is observed as fronts of high strain rate propagating through the suspension leaving a jammed state in its wake. Earlier experiments have observed this transition when the sample is subjected to pushing, pulling or shearing, independently, when the shear front is freely propagating or interacting with a solid boundary.

This thesis presents an experimental study of the dynamic jamming phenomenon in dense cornstarch suspensions where two jamming fronts are generated simultaneously for the first time. The experiments are two dimensional and both the velocity field and features of the free surface are used to assess the state of the suspension. We expand upon the previous observations by developing an experimental setup where the flow is visualized for the full field surrounding the perturbing body where pushing, pulling and shearing are observed in a single experiment. By introducing two perturbing bodies, the response of the suspension is investigated as the

front collides.

Key accomplishments include the observation of an unjammed pocket in the collision region between the perturbing bodies. Velocity measurements alone do not capture the shape of this pocket. However, it is clearly indicated by the free surface texture. Furthermore, a method is developed which is capable of quantifying the orientation of the features on the free surface. As shown by the literature, a scalar measure of the local accumulated strain of the material is a sufficient measure for the solid-liquid transition as the front propagates unimpeded through the suspension. However, this thesis reveals that both the shape of the unjammed pocket and the orientation of the surface features are closely linked to the direction of principle strain.

# Preface

This thesis is submitted to the Norwegian University of Science and Technology (NTNU) for partial fulfillment of the requirements for the degree of philosophiae doctor. The doctoral work has been carried out in the Thermo Fluids Group at the Department of Energy and Process Engineering (EPT), from August 2018 to August 2021. The work has been supervised by R. Jason Hearst and co-supervised by Ivo R. Peters.

The research was funded by the Department of Energy & Process Engineering at NTNU.

The thesis is made up of four chapters and three scientific papers. The first three chapters introduce the field, review literature, and explain the theory, the experimental setup and methods. The research articles are summarized in Chapter four and are included in full text at the end of the thesis.

## *Article I*

### **Getting jammed in all directions: Dynamic shear jamming around a cylinder towed through a dense suspension**

Olav Rømcke, Ivo R. Peters, R. Jason Hearst

*Physical Review Fluids*, **6**, 063301, (2021)

<https://doi.org/10.1103/PhysRevFluids.6.063301>

*Authors' contributions:* O.R. performed the experiment and evaluated the results. I.R.P. and R.J.H. provided technical guidance and ideas. O.R. wrote the draft. All authors contributed to editing the manuscript.

*Article II***Characterizing the surface texture of a dense suspension undergoing dynamic jamming**

Olav Rømcke, Ivo R. Peters, R. Jason Hearst

*Experiments in Fluids* **62**, 226 (2021)<https://doi.org/10.1007/s00348-021-03323-3>

*Authors' contributions:* O.R. conceived of the project, performed the experiment and developed the method. I.R.P. and R.J.H. provided technical support and guidance. O.R. wrote the draft. All authors contributed to editing the manuscript.

*Article III***Collision of dynamic jamming fronts in a dense suspension**

Olav Rømcke, Ivo R. Peters, R. Jason Hearst

*Physical Review Fluids*, **6**, 103301, (2021)<https://doi.org/10.1103/PhysRevFluids.6.103301>

*Authors' contributions:* I.R.P. and R.J.H. conceived of the project. O.R. performed the experiment and evaluated the results. All authors contributed to writing and editing the manuscript.

Additional article and abstracts not formally included in the thesis include:

**The impact of upstream turbulence on a plane jet**

Md Kamaruzzaman, Olav Rømcke, R. Jason Hearst

*Experiments in Fluids, Volume 62, January 2021, Article no. 18*<https://doi.org/10.1007/s00348-020-03106-2>**A projection method for solid-liquid phase transitions with natural convection**

Olav Rømcke, R. Jason Hearst

*71st American Physical Society Division of Fluid Dynamics Meeting, At-*

*lanta, Georgia, Nov 19, 2018*

**Dynamic jamming around a cylinder moving through a shear thickening suspension**

Olav Rømcke, Ivo R. Peters, R. Jason Hearst

*72nd American Physical Society Division of Fluid Dynamics Meeting, Seattle, Washington, Nov. 24, 2019*

Trondheim, 22.08.2021

Olav Rømcke





# Acknowledgements

Though a PhD can feel lonesome at times, this project could not have been completed without the help and support of the people who have surrounded me the last three years, to whom I would like to extend my gratitude.

First of all I would like to thank my supervisors. My main supervisor, R. Jason Hearst, has provided much needed support and insight, and shown a level of patience I can only thank you for. The time, dedication and effort you put into the Fluids Lab at NTNU, EPT have thoroughly impressed me, and will remain a source of inspiration. My co-supervisor, Ivo R. Peters, has been a key source of knowledge. Having a cornstarch-guru on board has been very helpful and your ideas and know-how have been extremely valuable.

To the PhD students and post docs of the Thermo fluids group; you have made the last years very enjoyable both inside and outside the lab. A special thanks go to my office mates (you know who you are). Activities ranging from the comatose coffee break to the infamous and competitive "Fluids Bowls" have been much needed intermissions from the work.

Finally, my friends and family who have shown support and understanding. In particular, my wife: You know me too well.



# Contents

<b>Abstract</b>	<b>iii</b>
<b>Preface</b>	<b>iv</b>
<b>Acknowledgements</b>	<b>vii</b>
<b>Contents</b>	<b>ix</b>
<b>Nomenclature</b>	<b>xiii</b>
<b>1 Introduction</b>	<b>1</b>
1.1 Background . . . . .	2
1.1.1 Viscosity and volume fraction . . . . .	2
1.1.2 Mechanisms for shear thickening . . . . .	4
1.2 Dynamic jamming . . . . .	7
1.2.1 Jamming below $\phi_{\max}$ . . . . .	7
1.2.2 Shear fronts . . . . .	11
1.3 Free surface features . . . . .	14
1.4 The goal of this study . . . . .	17

<b>2 Experiments and Material</b>	<b>19</b>
2.1 The suspension . . . . .	19
2.2 Jamming front experiments . . . . .	21
2.2.1 Experimental Rig . . . . .	22
2.2.2 Preparation and Protocol . . . . .	22
<b>3 Methods</b>	<b>27</b>
3.1 Particle image velocimetry . . . . .	27
3.1.1 Processing . . . . .	28
3.1.2 Kinematic properties . . . . .	29
3.2 Surface texture analysis . . . . .	33
<b>4 Summaries of the research articles and future work</b>	<b>35</b>
<b>Bibliography</b>	<b>38</b>
<i>Article I: Getting jammed in all directions: Dynamic shear jamming around a cylinder towed through a dense suspension</i>	<b>53</b>
<i>Article II: Characterizing the surface texture of a dense suspension undergoing dynamic jamming</i>	<b>75</b>
<i>Article III: Collision of Dynamic Jamming Fronts in a Dense Suspension</i>	<b>90</b>

# Nomenclature

This section summarises abbreviations, physical parameters and notation used throughout the introductory part of the thesis. In the individual publications, which are appended at the end of the thesis, the nomenclature might differ slightly, but is always clearly defined therein.

## Greek Symbols

$\alpha$	exponent in the $\eta$ - $\phi$ relation
$\beta$	starch water content
$\epsilon$	scalar strain
$\epsilon_c$	onset strain
$\eta$	viscosity
$\eta_0$	suspending fluid viscosity
$\eta_r$	dimensionless viscosity
$\Gamma$	surface tension
$\gamma$	shear
$\gamma^*$	characteristic shear
$\dot{\gamma}$	shear rate
$\kappa$	boltzmann constant

$\lambda$	stretch eigenvalues
$\mu$	friction coefficient
$\nu$	kinematic viscosity
$\phi$	volume fraction
$\phi_{\max}$	jamming volume fraction
$\phi_m$	frictional jamming volume fraction
$\phi_0$	frictionless jamming volume fraction
$\phi_{\text{eff}}$	effective jamming volume fraction
$\phi_J$	isotropic jamming volume fraction, granular
$\phi_S$	lower shear jamming volume fraction, granular
$\phi_V$	porosity corrected volume fraction
$\phi_W$	weight fraction
$\rho$	density
$\rho_s$	density, solid phase
$\rho_l$	density, liquid phase
$\rho_w$	density, water
$\Sigma$	shear stress
$\Sigma^*$	characteristic shear stress
$\xi$	porosity
$\zeta$	strain eigenvalues

**Latin symbols**

$Ca$	capillary number
$D$	cylinder diameter
$\mathbf{D}$	rate of strain tensor
$\bar{D}$	particle diffusion coefficient

---

$d_s$	particle diameter
$\mathbf{e}$	Eulerian logarithmic strain tensor
$\mathbf{F}$	deformation gradient tensor
$f$	fraction of frictional contacts
$g$	gravitational acceleration
$I$	image intensity
$\hat{I}$	Fourier transformed image intensity
$k$	front propagation factor
$k_t$	transverse front propagation factor
$k_l$	longitudinal front propagation factor
$l$	surface roughness
$m_s$	mass, solid phase
$m_l$	mass, liquid phase
$\mathbf{N}$	stretch and strain eigenvector, undeformed configuration
$\mathbf{n}$	stretch and strain eigenvector, deformed configuration
$P$	particle pressure
$P^*$	characteristic particle pressure
$Pe$	peclet number
$\mathbf{R}$	rotation tensor
$St$	stokes number
$T$	temperature
$t$	time
$\mathbf{U}$	right stretch tensor
$U_0$	perturbing speed
$U_f$	front speed



$u$	$x$ velocity component
$\mathbf{u}$	velocity vector
$\mathbf{u}_A$	velocity, aft frame
$\mathbf{u}_F$	velocity, fore frame
$u_s$	settling speed
$\mathbf{V}$	left stretch tensor
$w_{S,A}$	stitch weight, aft frame
$w_{S,F}$	stitch weight, fore frame
$w_H$	filter weight, Hanning window
$\mathbf{X}$	position, undeformed configuration
$x$	coordinate axis parallel to perturbation direction
$\mathbf{x}_P$	position, deformed configuration
$x_f$	front position
$y$	coordinate axis normal to perturbation direction

**Abbreviations**

CST	Continuous Shear Thickening
DST	Discontinuous Shear Thickening
F	Fragile
FFT	Fast Fourier Transform
PIV	Particle Image Velocimetry
PSD	Power Spectral Density
SJ	Shear Jamming
WC	Wyart and Cates

# Chapter 1

## Introduction

Suspensions exist all around us e.g. clay, slurry, foods and cosmetics, and appear in both industrial and geological processes such as the flow of fresh concrete, sediment transport and landslides. Though a suspension is simply a mixture of solid particles and a fluid, they can exhibit complex and curious behaviour. Suspensions with a high concentration of particles share many properties with granular material such as gravel, sand and powders. They have the ability to flow, such as in an hour glass, but can clog up pipes and conduits and can form a rigid foundation for our roads and pavements. Understanding the underlying mechanisms for when a material flows or not is interesting in and of itself from an academic perspective, and is of paramount importance in terms of how we design our infrastructure when accounting for mud slides, avalanches and clogged drain pipes.

The focus in this work is on dense cornstarch suspensions, which have the ability to flow when subjected to a low stress, but appear to turn into a solid when subjected to a sudden impact or otherwise large stress. The process is reversible and once the stress is released the suspension returns to a liquid state. Particle-particle contacts and friction are some of the driving mechanisms for this behaviour. An important parameter describing the behaviour of the suspension is the ratio between the volume occupied by the solid and the total volume, this is referred to as the packing or volume fraction ( $\phi$ ). However, the volume fraction alone is not enough to fully describe the suspension. The role of particle shape, size as well as chemical composition can radically affect the observed behaviour. As such, the study of suspensions in general covers a wide set of topics and scales ranging from large geological systems to effects only observed at the nano scale as well as

the interaction between these. This in turn leads to strange, and at times counter-intuitive, phenomenology.

The last decade has seen a significant development in our understanding of the underlying mechanisms for dynamic jamming. Of particular interest here is the transient response: how the material locally transitions into a jammed state and successively spreads into the otherwise unjammed suspension when influenced by a perturbing body. The transition is seen as a front of high shear rate moving through the suspension, leaving a jammed state in its wake. The aim of this study is to observe how two such jamming fronts interact. As such, this introduction is not intended to give a full review on suspension research, but to present the development and relevant literature with regards to dynamic jamming phenomenon. Section 1.1 gives a brief history of suspension research and presents some of the key mechanisms for shear thickening, while section 1.2 focuses on dynamic jamming. Section 1.3 presents some of the features observed at the free surface, which will be used as a tool for identifying different regions of the flow. Finally, the goal of this study is presented in section 1.4.

## 1.1 Background

### 1.1.1 Viscosity and volume fraction

Viscosity ( $\eta \equiv \Sigma/\dot{\gamma}$ ) describes how easily the material flows and is the relation between shear stress ( $\Sigma$ ) and shear rate ( $\dot{\gamma}$ ). For low shear rate and volume fractions ( $\phi$ ), analytic corrections to the viscosity when adding particles to the flow can be found in the work by Einstein (1906, 1911) and Batchelor and Green (1972). For a suspension of hard spheres and a fluid with viscosity  $\eta_0$ , the relation

$$\eta/\eta_0 = 1 + 2.5\phi + O(\phi^2), \quad (1.1)$$

by Einstein is valid for  $\phi$  up to  $\sim 0.03$ . Batchelor later calculated expressions up to terms of order  $O(\phi^2)$ , showing agreement with experiments up to  $\phi \sim 0.15$  (Guazzelli and Pouliquen, 2018). Batchelor's success was not only to establish the hydrodynamic contributions between particles, but to acknowledge the importance of microstructure (Mewis and Wagner, 2012); as the contribution to  $\phi^2$  is in part due to pairwise interactions between neighbouring particles, their relative position in the flow is important, and as such the second order expansion depends on the type of flow (Stickel and Powell, 2005; Shewan and Stokes, 2015; Guazzelli and Pouliquen, 2018).

Beyond the semi-dilute regime discussed above, increasing the volume frac-

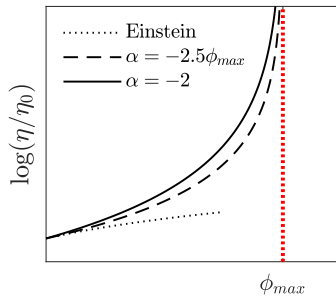


Figure 1.1: Viscosity as a function of volume fraction, showing equations (1.1) and (1.2) with  $\alpha = -2.5\phi_{\max}$  (Krieger and Dougherty, 1959) and  $-2$  (Maron and Pierce, 1956; Quemada, 1977).

tion leads to a dramatic increase in viscosity, up to some point ( $\phi_{\max}$ ) where flow ceases (Mewis and Wagner, 2012) and solid-like behaviour such as fracturing has been observed (Metzner and Whitlock, 1958; Denn et al., 2018). Computing the viscosity for higher volume fractions is mathematically complex and exact analytic solutions do not exist. Rather, several semi-empirical relations have been developed (Ferrini et al., 1979; Zarraga et al., 2000; Mendoza and Santamaría-Holek, 2009) capturing the diverging behaviour in the dense range. A commonly used expression takes the form (Krieger and Dougherty, 1959; Maron and Pierce, 1956; Quemada, 1977)

$$\eta/\eta_0 = (1 - \phi/\phi_{\max})^\alpha, \quad (1.2)$$

where  $\phi_{\max}$  represents the volume fraction at which viscosity diverges. Comparisons between several  $\eta - \phi$  relations as well as experimental and simulation results is readily available in the literature (Stickel and Powell, 2005; Guazzelli and Pouliquen, 2018). Here, two commonly used values for  $\alpha$  together with equation (1.1) are shown in figure 1.1.

In the previous paragraphs, the viscosity has only been presented as a function of the volume fraction. Both inertial and Brownian effects can influence the behaviour, which is characterized by the Stokes ( $St = \rho_s d_s^2 \dot{\gamma} / \eta_0$ ) and Peclet numbers ( $Pe = \eta_0 d_s^3 \dot{\gamma} / \kappa T$ ), respectively. Here,  $\rho_s$ ,  $d_s$ ,  $\kappa$  and  $T$  represent particle density, diameter, Boltzmann constant and temperature, respectively. For  $St > 1$  inertial effects will influence the behaviour and for  $Pe < 1$  Brownian effects become significant. Assuming a non-Brownian ( $Pe \gg 1$ ), non-inertial ( $St \ll 1$ ), hard sphere suspension a dimensional analysis suggests that the viscosity is a function of the volume fraction only (Stickel and Powell, 2005; Denn et al., 2018). That is, at a given volume fraction,

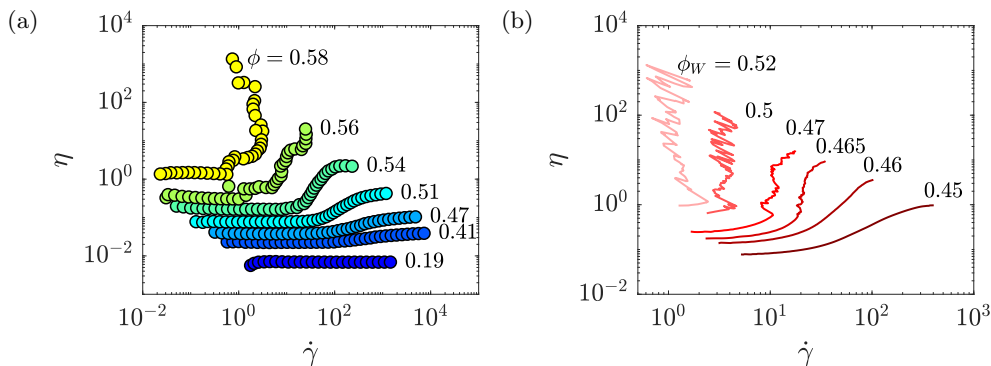


Figure 1.2: Continuous and discontinuous shear thickening in suspensions of (a) poly-methylmethacrylate and (b) cornstarch particles. Note the extreme viscosity jump for the highest particle concentrations, spanning several orders of magnitude. The data for the flow curves are from (a) figure 1c in [Guy et al. \(2015\)](#) and (b) figure 1a in [Hermes et al. \(2016\)](#).  $\phi_W$  indicates weight- rather than volume fraction.

the behaviour can be assumed to be Newtonian. However, this falls short of adequately describing the non-Newtonian behaviour observed in many real non-Brownian, non-inertial suspensions ([Hoffman, 1972](#); [Wyart and Cates, 2014](#); [Brown and Jaeger, 2014](#)).

For the scope of this work the observed shear thickening is of particular interest, that is when increasing the shear rate,  $\dot{\gamma}$ , the viscosity  $\eta$  also increases, a phenomenon not captured by equations (1.1) and (1.2). The shear thickening observed in dense suspensions becomes more dramatic with increasing volume fraction ([Barnes, 1989](#)). Figures 1.2a and 1.2b show viscosity measurements by [Guy et al. \(2015\)](#) and [Hermes et al. \(2016\)](#), respectively. Both experiments are examples of non-Brownian, non-inertial suspension systems. Note how the curves gradual transition from a smooth and *Continuous Shear Thickening* (CST) to an abrupt viscosity increase or *Discontinuous Shear Thickening* (DST) with increasing  $\phi$ . The latter behaviour shows an impressive viscosity jump spanning several orders of magnitude.

### 1.1.2 Mechanisms for shear thickening

The observed shear thickening has puzzled scientists for decades, and several mechanisms have been proposed ([Brown and Jaeger, 2014](#)). One such mechanism is the order-disorder transition developed by [Hoffman \(1974, 1982\)](#). In

some cases the transition to DST with increasing shear rate corresponded to a change in microstructure from ordered layers to a disordered state. However, it was shown that this is not a requirement for DST to occur (Maranzano and Wagner, 2002; Egres and Wagner, 2005; Egres et al., 2006). A second mechanism is hydroclustering proposed by Brady and Bossis (1985). This framework suggests that particles tend to push together into clusters when subjected to shear. As lubrication forces between two approaching spheres diverge, this rearrangement of particles leads to increased resistance to flow (Wagner and Brady, 2009). The hydrocluster mechanism has successfully reproduced CST viscosity curves. However, this framework has not been able to reproduce DST (Brown and Jaeger, 2014).

Dilation has been pointed out as an important mechanism in dense suspensions. Dilation of dense granular material was first described by Reynolds (1885). In short, when a granular material is sheared, the granules have to move past each other. If the packing is sufficiently dense, the granular structure needs to expand in order for this to happen, which induces normal stresses pushing against the boundary (Fall et al., 2008; Brown and Jaeger, 2012). Common for experimental configurations is that the sample is confined between solid boundaries and an air-liquid interface. Brown and Jaeger (2012) explained the extreme shear thickening as a result of a *frustrated* dilation. That is, upon applying shear, the sample wants to dilate. However, due to the boundary confinement (either due to the solid walls, or surface tension effects), the particles are instead pushed into contact. These particle-particle contacts can be a significant contributor to the overall stress in the sample. A connection between shear thickening and dilation has been known for a long time, to the degree that the words dilatancy and shear thickening are in some of the older sources used interchangeably (Barnes, 1989).

As indicated by the mechanisms mentioned above as well as noted by Batchelor's early work, the key to a better description of the dynamic behaviour of suspensions lies in a proper understanding of the interactions at the particle scale. Evidence of a shear induced structure has been shown experimentally in shear reversal experiments (Gadala-Maria and Acrivos, 1980). The underlying idea behind shear reversal is simply that immediately upon shear reversal, contact stresses vanish, however, the hydrodynamic stresses remain due to the reversibility of Stokes flow. Gadala-Maria and Acrivos (1980) observed a difference in the nominal stress before and after shear reversal, and attributed this to a developing anisotropic particle structure (Parsi and Gadala-Maria, 1987). Contact forces and friction are important mechan-

ism in dense suspensions (Huang et al., 2005; Lootens et al., 2005; Comtet et al., 2017). Taking inspiration from dry granular rheology, Boyer et al. (2011) showed that particle contacts contribute significantly to the effective viscosity in the dense regime. Simulations have given valuable insight into particle scale phenomena of shear thickening suspensions. This approach makes it possible to explore a vast parameter space such as shape and size of particles, friction and other contact forces (Sivadasan, 2020). Shear reversal experiments and simulations by Lin et al. (2015) as well as steady state simulations (Seto et al., 2013; Mari et al., 2014, 2015a,b) provided further evidence that particle contacts and friction (Fernandez et al., 2013; Heussinger, 2013; Seto et al., 2013) have a significant contribution to the observed shear thickening.

The onset of DST gives further insight into the underlying mechanisms. Earlier sources focus on the shear rate at which the sudden viscosity jump occurs (Barnes, 1989). However, later sources show that the onset can be characterized by an onset stress independent of volume fraction and the viscosity of the suspending fluid (Frith et al., 1996; Maranzano and Wagner, 2001; Shenoy and Wagner, 2005; Brown and Jaeger, 2009). The existence of a stress scale independent of hydrodynamic parameters is explained by a repulsive force between particles (Brown and Jaeger, 2014). The repulsive force could be Brownian (Bertrand et al., 2002; Kawasaki and Berthier, 2018), electro static potential (Maranzano and Wagner, 2001), steric (Hoffman, 1998; Guy et al., 2015; Comtet et al., 2017), etc. Importantly, this force sets a stress scale above which the particles have frictional contact which greatly increases the resistance to flow. When contacts become frictional,  $\phi_{max}$  decreases (Mari et al., 2014; Morris, 2018). In the context of the  $\eta - \phi$  curve in figure 1.1, this moves the point where viscosity diverges to the left.

This stress induced thickening can be summarized by the steady state Wyart and Cates (2014) (WC) model. In the spirit of equation (1.2), subjecting the sample to a shear stress changes the effective jamming volume fraction <sup>1</sup>

$$\eta/\eta_0 = (1 - \phi/\phi_{\text{eff}}(\Sigma))^{-2}. \quad (1.3)$$

Here, the stress dependent jamming volume fraction is a simple interpolation between a frictional  $\phi_m$  and lubricated  $\phi_0$  jamming volume fractions

---

<sup>1</sup>In the original work by Wyart and Cates (2014) the model is formulated in terms of the particle pressure  $P$ . Here we have done the substitution  $\Sigma = \mu P$  (Hermes et al., 2016; Han et al., 2019a; Guy et al., 2020), where the friction coefficient  $\mu$  is assumed to be constant.

such that  $\phi_{\text{eff}}(\Sigma) = f(\Sigma)\phi_m + [1 - f(\Sigma)]\phi_0$ , where  $\phi_m < \phi_0$  as noted in the previous paragraph. The parameter  $f(\Sigma) = 1 - e^{-\Sigma/\Sigma^*}$  represents the fraction of particles in frictional contacts. The onset stress  $\Sigma^*$  sets the scale for where the lubricated-frictional transition occurs. For a given  $\phi$ , increasing the stress ruptures the lubrication films between particles causing the fraction of frictional contacts to increase. This in turn decreases  $\phi_{\text{eff}}(\Sigma)$  which results in a viscosity increase shown in figure 1.3a. The exponent from equation (1.2) takes the value  $\alpha = -2$  in equation (1.3) capturing the roughly  $(\phi_{\text{max}} - \phi)^{-2}$  viscosity scaling in the dense regime (Boyer et al., 2011; Guy et al., 2015) and commonly used for these systems (Hermes et al., 2016; Han et al., 2019a).

Resulting flow curves are plotted in figure 1.3b. Both CST and DST curves are shown as a transition between two quasi-Newtonian states. However, DST occurs when the flow curves are S-shaped in terms of  $\dot{\gamma}$ . In rate controlled experiments, a viscosity jump is observed, as the viscosity only takes on one value. However, careful stress controlled systems (Pan et al., 2015; Mari et al., 2015a), reveal these S-shaped features. For volume fractions in the range  $\phi_m < \phi < \phi_0$  the WC model predicts that the viscosity diverges at a non-zero stress as  $\phi_{\text{eff}}$  approaches  $\phi$ . Here the flow is rather counter-intuitively arrested, or *Shear Jammed* (SJ) (Seto et al., 2013; Peters et al., 2016), discussed in section 1.2. These properties of the flow curves makes it possible to construct a phase diagram shown in figure 1.3c. Regions where the different regimes can be accessed are noted in the diagram.

In this brief history of suspension research a few key mechanisms have been identified that contribute to the extreme shear thickening observed in some dense, non-inertial, non-Brownian suspension systems. Though viscous effects play a role at this scale, contacts between particles become increasingly important with increasing volume fraction. Beyond the hard sphere model, this typically means that friction forces also contribute to the stress in the system. A repulsive force between particles sets a stress at which contacts occur. As such the emerging explanation for shear thickening emphasized by the WC model is that it is a stress ( $\Sigma$ ) rather than a strain rate ( $\dot{\gamma}$ ) induced transition from lubricated to frictional contacts between particles.

## 1.2 Dynamic jamming

### 1.2.1 Jamming below $\phi_{\text{max}}$

In the previous section, the focus was on shear thickening. However, some studies have also reported the existence of a jammed state for volume frac-



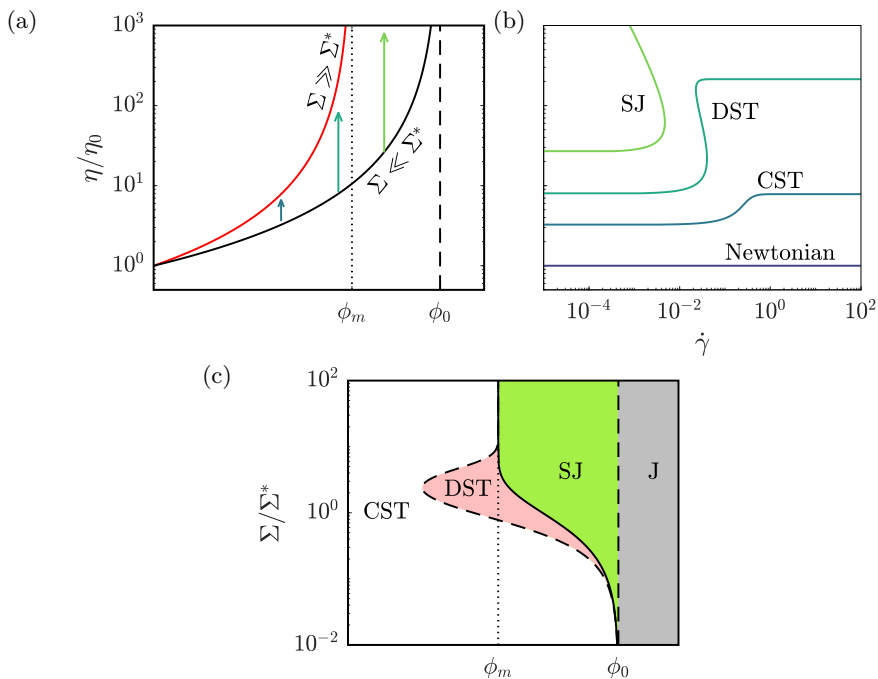


Figure 1.3: A summary of the [Wyart and Cates \(2014\)](#) model. (a) High and low stress viscosity as a function of  $\phi$ . Arrows indicate the location of the (b)  $\eta$ - $\dot{\gamma}$  flow curves. (c) Phase diagram constructed from equations (1.3). Including the definition  $\eta \equiv \Sigma/\dot{\gamma}$ , the CST-DST transition is identified by  $d\dot{\gamma}/d\Sigma = 0$ , while the DST-SJ transition is identified by  $\dot{\gamma} = 0$  for  $\Sigma > 0$ .

tions below  $\phi_{\max}$  (Bertrand et al., 2002; Fall et al., 2008, 2012, 2015; Peters et al., 2016). Jamming is understood as the existence of a non-zero yield stress, below which flow does not occur (Liu and Nagel, 1998, 2010; O’Hern et al., 2003; Brown and Jaeger, 2009). There is a close connection between DST and jamming in dense suspensions (Brown and Jaeger, 2014), as shown by the WC model introduced above. Insight from dry granular systems has been fruitful for understanding suspensions in the dense regime (Boyer et al., 2011; Lerner et al., 2012; DeGiuli et al., 2015). This is probably most revealing when comparing their respective phase diagrams.

Figure 1.4 shows phase diagrams of suspensions and dry granular materials both with and without frictional interactions. For granules without friction, jamming is controlled by the volume fraction, a scenario proposed by Liu and Nagel (1998) shown here in 1.4a. As noted in the beginning of section 1.1.1 and exemplified by equation 1.2, for suspensions flow ceases beyond  $\phi_{\max}$  (Metzner and Whitlock, 1958; Mewis and Wagner, 2012; Denn et al., 2018), shown schematically in figure 1.4b. However, the theoretical scenario by Cates et al. (1998) proposes a shear induced solidification whereby the material develops force chains, which are capable of supporting the applied stress, which differs from the density induced jamming scenario by Liu and Nagel (1998).

Evidence of this theoretical scenario was first shown by Bi et al. (2011) who investigated the impact of friction on a system of photo-elastic, disk-shaped grains, making it possible to quantify the force network in the material (Majmudar and Behringer, 2005) (see also Zhang et al. (2010); Ren et al. (2013); Sarkar et al. (2016); Wang et al. (2018); Zadeh et al. (2019) for similar experiments). Over a range of volume fractions ( $\phi_S < \phi < \phi_J$ ), non-zero stresses developed as the material was strained, showing an anisotropic force network eventually spanning the whole domain. This state was defined as shear jammed, and importantly, depending on the volume fraction, there is a minimum stress and strain needed to enter a SJ state (Bi et al., 2011; Sarkar et al., 2016; Behringer and Chakraborty, 2018). The anisotropy tends to vanish when approaching  $\phi_J$  and jamming at  $\phi \geq \phi_J$  is referred to as an isotropically jammed state. Bi et al. (2011) presented a modification to the phase diagram suggested by Liu and Nagel (1998) shown here in 1.4c. Similarly, Peters et al. (2016), studying both the steady-state and transient response of a dense cornstarch suspension, identified a shear induced jammed state for volume fractions below  $\phi_{\max}$ , shown in figure 1.4d. The two systems exhibit several striking similarities, most notably the shear induced jammed state. Both studies show that a sufficient amount of stress

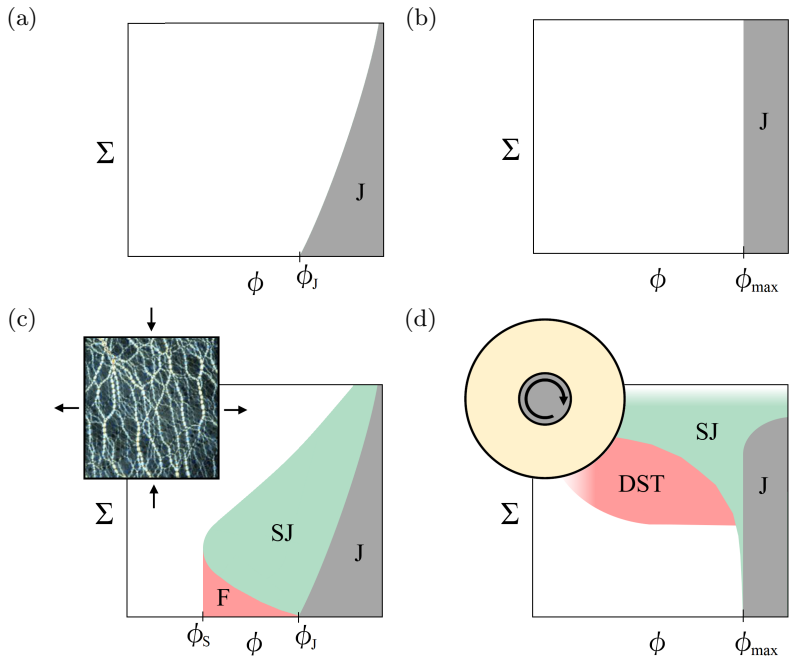


Figure 1.4: Schematic representation of (a) granular and (b) suspension phase diagrams without frictional interactions. (c) Granular phase diagram with frictional interactions. The inset shows a shear jammed state with strain directions indicated by the arrows. The fragile regime (F) is a state where the contact network does not span the whole extension direction. (a) and (c) are from [Bi et al. \(2011\)](#). (d) Phase diagram measured for a cornstarch suspension from [Peters et al. \(2016\)](#). The inset indicates the wide gap Couette cell used in the experiment.

and strain is required to reach this regime. In addition, [Peters et al. \(2016\)](#) suggested that DST corresponds to the fragile state (F) in granular matter ([Vitelli and van Hecke, 2011](#)), in that these states are not fully jammed, but a precursor to shear jamming.

It is worth noting the qualitative similarities between the WC model in figure 1.3c and the phase diagram by [Peters et al. \(2016\)](#) in figure 1.4d. In the dense regime, both the model and the measurements show a transition from a viscous regime through DST behaviour, ending in a shear jammed state as the stress is increased. From the concept that shear thickening is stress induced ([Frith et al., 1996](#); [Maranzano and Wagner, 2001](#); [Shenoy and Wagner, 2005](#); [Brown and Jaeger, 2009, 2014](#)), the WC model provides a basis for where shear jamming is expected to be observed. With few fitting parameters, it is a useful tool for understanding macroscopic behaviour, and has provided a framework and a source of study ([Hermes et al., 2016](#); [Royer et al., 2016](#); [Guy et al., 2015, 2020](#); [Han et al., 2018, 2019a](#); [Gillissen et al., 2019](#); [Singh et al., 2020](#)). However, as microscopic properties are not directly included in the model, it is worth pointing out that effects from the chemical composition ([Clavaud et al., 2017](#); [James et al., 2018](#)), particle shape ([Brown et al., 2011](#); [James et al., 2019](#)) and poly dispersity ([Guy et al., 2020](#)) can also influence the macroscopic behaviour. Furthermore, in steady state experiments above  $\phi_m$  the flow is observed to be unsteady ([Hermes et al., 2016](#)) and flow curves in this regime generally deviate from the WC model ([Baumgarten and Kamrin, 2019b](#)). Nevertheless, the range  $\phi_m < \phi < \phi_0$  will be used here as a basis for where we conduct our dynamic jamming front experiments ([Han et al., 2018, 2019a](#)).

### 1.2.2 Shear fronts

The concept of dynamic jamming fronts was first introduced by [Waitukaitis and Jaeger \(2012\)](#). In cornstarch suspensions it was observed that upon impact, the transition into a solid-like state occurred locally. The transition was initiated at the point of impact before propagating into the otherwise unjammed suspension transforming it to a jammed state. The front was identified as the separation between the quiescent, unjammed region and the region translating at the speed of the impactor ( $U_0$ ). The location of the front ( $x_f$ ) is typically identified by the  $0.5U_0$  velocity contour separating the two states ([Waitukaitis et al., 2013](#)). This seminal work sparked the study of shear jamming fronts. Later studies have observed this phenomenon when subjected to shear ([Peters et al., 2016](#); [Han et al., 2018, 2019a](#)), extension ([Majumdar et al., 2017](#)) as well as other impact experiments ([Peters and Jaeger, 2014](#); [Han et al., 2016, 2019b](#); [Allen et al., 2018](#))

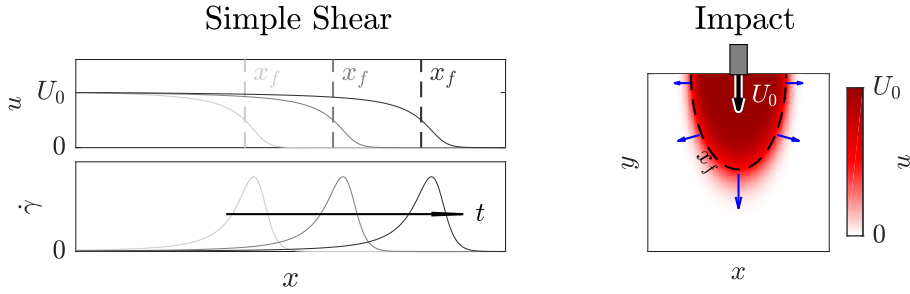


Figure 1.5: Shear jamming fronts in 1D simple shear showing consecutive realisations of the velocity ( $u$ ) and shear rate ( $\dot{\gamma}$ ) as well as a snapshot of the velocity field in a 2D impact configurations. The location of the front ( $x_f$ ) is indicated by the dashed lines. Blue arrows indicate the front speed ( $U_f$ ). These plots are schematics recreated from Han et al. (2016, 2018) and intended to give the reader an intuition for how the front propagates through the suspension.

and over a wide range of sizes from centimeters scales in the lab (Peters et al., 2016; Han et al., 2016; Majumdar et al., 2017) to kilometer scale geological flows (Peters et al., 2015). A typical measure for these types of flows is the front propagation factor,  $k$ , defined as the relationship between the speed of the front ( $U_f$ ) and the perturbing body ( $k \equiv U_f/U_0$ ). A schematic of this process is provided in figure 1.5.

Experimental studies on dynamic shear jamming fronts have typically used dense cornstarch suspensions. As the material is opaque, this poses some challenges with regards to measuring the flow field. Both X-ray (Waitukaitis and Jaeger, 2012) and ultrasound (Han et al., 2016, 2019b) imaging techniques have been developed in order to view the internal flow field. However, by constructing an approximately 2D set-up, the movement of the optically accessible free surface has been used to quantify the velocity field (Peters and Jaeger, 2014; Han et al., 2018), circumventing the spatial and temporal limitations of X-ray and ultrasound approaches. Here, a centimeter thick layer of suspension floats atop a high density, low viscosity oil (Fluorinert), creating a near stress free bottom boundary, similar to Loimer et al. (2002). Microscopically, the jamming mechanism is fully three-dimensional as the thickness of the suspension layer is much larger than the particle size. However, macroscopically, the front propagation is confined to the suspension layer, making its propagation approximately 2D (Peters and Jaeger, 2014; Han et al., 2018). Common for all these approaches is that the velocity field

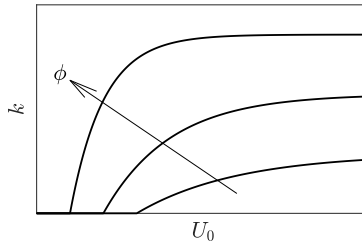


Figure 1.6: Phenomenological behaviour of the front propagation factor,  $k$ , as a function of  $U_0$  and  $\phi$ . The plots qualitatively follows the curve fit used by Han et al. (2016).

is constructed from successive images of the suspension using particle image velocimetry (PIV). This make it possible to retrieve details of the local kinematic properties of the flow, such as front propagation factor, strains and strain rates.

For volume fractions in the range  $\phi_m < \phi < \phi_0$  at low perturbing speeds ( $U_0$ ), the suspensions is viscous and the front position ( $x_f$ ) does not propagate (Peters et al., 2016). In contrast, at sufficiently high speeds, the behaviour transitions into friction dominated interactions between particles due to the high stresses (Han et al., 2016). Here, the front propagates with a constant velocity through the suspension and the front propagation factor,  $k$ , is independent of  $U_0$ . The front propagation factor increases, while the minimum speed at which the front is observed to propagate decreases with volume fraction shown schematically in figure 1.6. Though  $k$  is relatively constant during the course of an experiment, the front is observed to propagate at different speeds depending on the direction relative to the perturbing body (Peters and Jaeger, 2014; Han et al., 2016, 2019b). For a given volume fraction, the front propagation factor is roughly twice as fast in the direction of perturbation relative to the transverse direction as indicated in figure 1.5. An early model for the observed impact-activated solidification proposed that the impactor pushed particles closer until the local volume fraction reached  $\phi_0$  (Waitukaitis and Jaeger, 2012).

The compaction model explains the phenomenon that the front speed increases with volume fraction, as the particles are originally situated closer together (Waitukaitis et al., 2013). However, jamming fronts are observed for different deformation modes such as simple shear (Han et al., 2018) and extension (Majumdar et al., 2017), which is not captured by this model.

Ultrasound measurements of the suspension during jamming indicated that the volume fraction does not increase nearly enough to reach  $\phi_0$  (Han et al., 2016). Rather, it was proposed that a finite amount of strain ( $\epsilon_c$ ) independent of the deformation mode was needed to be achieved in order for the suspension to transition into a jammed state (Fall et al., 2012; Peters et al., 2016). This onset strain was shown to be related to the front propagation as  $k \propto 1/\epsilon_c$  (Han et al., 2016). In addition, the existence of an onset strain also explains why  $k$  was observed to propagate twice as fast when subjected to pure shear (extension/compression) compared to simple shear. As such, this scenario successfully explained the 1 : 2 relationship observed between the transverse and longitudinal front propagation factor (Peters and Jaeger, 2014; Han et al., 2016, 2019b).

By extending the Wyart and Cates (2014) framework to account for the local shear deformation ( $\gamma$ ), Han et al. (2019a) was able to model a freely propagating jamming front in a 1D simple shear system. The underlying idea was to modify the expression for the fraction of frictional contacts ( $f$ ) such that  $f(\gamma, \Sigma) = (1 - e^{-\gamma/\gamma^*})(1 - e^{-\Sigma/\Sigma^*})$ , requiring the addition of only a single fitting parameter,  $\gamma^*$ . Independently, Baumgarten and Kamrin (2019a) developed a fully general 3D model for dense suspension flows. In their work, modelling the fraction of frictional contacts was approached slightly differently. Rather than defining  $f$  directly, the time derivative,  $\dot{f}$ , was modelled as a sum of construction and destruction mechanisms of the granular contact network. These mechanisms include exceeding the repulsive stress scale, stress induced force chain buckling, plastic and diffusion driven rearrangement. No explicit strain scale is introduced in this model, however, the numerical results shows agreement with a wide range of experimental studies, even capturing the 1 : 2 relationship between the transverse and longitudinal front propagation factor. More fitting parameters are introduced in this general approach and details can be found in Baumgarten and Kamrin (2019a,b).

### 1.3 Free surface features

A free surface is present in most experimental set-ups studying dense suspension flow in one form or another (Guazzelli and Pouliquen, 2018; Denn et al., 2018). Though the free surface to volume ratio of a sample in traditional rheometer configurations such as Couette cells, cone-and-plate or parallel-plate are relatively small, this is not the case for some of the untraditional set-ups. In particular, the quasi-2D set-ups used to study the transient phenomena of dynamic shear jamming fronts have a large free

surface deliberately employed to gain optical access in order to measure the velocity field (Peters and Jaeger, 2014; Han et al., 2018).

Dilatancy is a visible surface feature in some dense suspension systems. As noted in section 1.1.2, it is the phenomena whereby the granular structure expands when sheared (Reynolds, 1885; Brown and Jaeger, 2012, 2014). Due to conservation of mass, the expansion of the solid phase causes a suction in the liquid phase (Fall et al., 2012; Jerome et al., 2016; Majumdar et al., 2017). As such, at the free surface individual particles start to protrude through the air liquid interface (Brown and Jaeger, 2012). A schematic representation of this process is presented in figure 1.7a. This roughening of the surface is observed at a large scale as a transition from smooth to matte surface texture indicated in figure 1.7b associated with large stresses applied to the suspension (Bischoff White et al., 2010; Smith et al., 2010; Brown and Jaeger, 2012; Roché et al., 2013; Brown and Jaeger, 2014; Allen et al., 2018; Maharjan et al., 2021). These shear induced normal stresses pushing particles towards the air-liquid interface is counteracted by surface tension forces. The curving of the liquid surface around a particle sets up a restoring force, which functions as a confining stress (Brown and Jaeger, 2012). For cornstarch-water suspensions this is at the order  $\Gamma/d_s \sim 10^3$  Pa, where  $\Gamma$  is the surface tension. Following the concept that the observed DST and jamming in dense suspension is a consequence of a frustrated dilation (Brown and Jaeger, 2012, 2014), this level of confining stress is significant relative to the onset of shear thickening measured in the range  $10^0$  to  $10^1$  Pa for cornstarch suspensions (Brown and Jaeger, 2014; Hermes et al., 2016; Han et al., 2018). Instead,  $\Gamma/d_s$  is found to scale approximately with the upper stress limit of the shear thickening regime for a wide range of suspensions and particle sizes. In fact, a similar scaling with the upper limit of shear thickening was found when the sample was confined between solid boundaries, substituting  $\Gamma$  with the stiffness of the wall (Brown and Jaeger, 2012). This supports the idea that the observation of shear thickening and jamming is linked to the ability of the system to set up confining stresses on the sample.

Several studies have shown the formation of a corrugated free surface in dense suspension flow (Loimer et al., 2002; Timberlake and Morris, 2005; Singh et al., 2006; Kumar et al., 2016). These surface features appear in the form of waves moving with the local velocity of the suspension (see figure 5 in Loimer et al. (2002)). The corrugations are shown to vary with particle size, concentration, surface tension, shear rate and viscosity (Loimer et al., 2002; Kumar et al., 2016). From balancing the shear induced particle flux



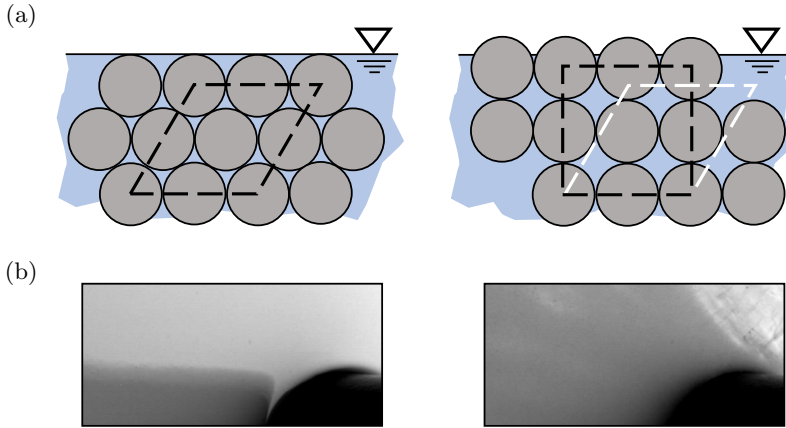


Figure 1.7: (a) Schematic representation of the dilation process. (b) Smooth to matte transition. Note how the cylinder shadow is clearly outlined in the left pane, which is not seen when the surface show dilation.

at the free surface with an inward flux due to the restoring force from the surface tension, [Loimer et al. \(2002\)](#) developed an expression for the relative surface roughness  $(l/d_s)^2 \propto \eta_r(\phi)\bar{D}(\phi)Ca$ . Here,  $Ca = \eta_0\dot{\gamma}d_s/\Gamma$  is the capillary number, while  $\eta_r = \eta/\eta_0$  and  $\bar{D}$  are the dimensionless viscosity (equation (1.2)) and particle diffusion coefficient ([Leighton and Acrivos, 1987](#)), respectively, assumed by [Loimer et al. \(2002\)](#) to be monotonically increasing functions of  $\phi$ . The above relation is presented here to indicate the general trend that the free surface roughness tends to increase with volume fraction and shear rate. However, this simple expression does not capture the full picture. First, it is worth noting that [Kumar et al. \(2016\)](#) observed a decrease in surface roughness at sufficiently high volume fraction  $\phi$  in their open channel flow. Secondly, both 1D ([Loimer et al., 2002](#); [Singh et al., 2006](#)) and 2D ([Timberlake and Morris, 2005](#)) spatial power spectra of surface images indicate the existence of structures over a wide range of scales both smaller and larger than the particle size. In addition, these power spectra indicate some anisotropy in the structures. That is, the features appear differently, depending on the orientation. These latter features indicate a fascinating phenomenology, not fully explored. Investigating how the free surface topology relates to both micro- and macroscopic properties of the material could be a fruitful endeavour and is particularly useful for opaque systems, such as cornstarch suspensions

## 1.4 The goal of this study

The last decade has seen significant progress in our understanding of the extreme shear thickening observed in dense frictional suspensions (Brown and Jaeger, 2014). Today this is understood as a stress induced transition from lubricated to frictional interactions between particles, which at sufficiently high volume fractions can lead to a shear induced jammed state known as dynamic jamming (Peters et al., 2016). Very recent macroscale continuum modeling has captured the transient development of this jammed state (Baumgarten and Kamrin, 2019a; Han, 2020). The transition occurs locally, and is observed as shear fronts propagating through the suspension leaving a jammed state in their wake (Waitukaitis and Jaeger, 2012; Peters and Jaeger, 2014; Han et al., 2016; Peters et al., 2016; Majumdar et al., 2017; Han et al., 2018, 2019b). Specifically, the consequence of an underlying strain scale controlling when the material locally transitions (Han et al., 2019a) explains both why the shear jamming fronts occur, and why they propagate with different speeds relative to the perturbing body (Han et al., 2016). Nonetheless, these experimental observations constitute relatively simple geometries with a single perturbing body, where the front is propagating freely through the suspension. More complex flows, i.e., how the suspension responds to multiple perturbing bodies and how shear fronts interact with each other are open questions.

Previous shear front experiments have largely identified the solid-like region from kinematic properties (Waitukaitis and Jaeger, 2012; Peters and Jaeger, 2014; Han et al., 2016; Majumdar et al., 2017; Han et al., 2019b). Though recent developments have been able to estimate the local stresses from the velocity field for a freely propagating shear front in a 1D simple shear system (Han et al., 2018, 2019a), kinematic properties alone might not be sufficient to identify the solid-like region in more complex flows. However, dilation, an observable feature of the free surface, is shown to be associated with the applied stress (Brown and Jaeger, 2012; Maharjan et al., 2021). The curving of the free surface around protruding particles provides a confining stress, and is observed as a transition into a matte surface (Allen et al., 2018). As such, this feature provides a qualitative measure for assessing the local stress state in the system.

The aim of this thesis is to experimentally address how two shear jamming fronts interact. The articles provided with this document present a step-by-step approach to observe how two shear jamming fronts interact, from constructing the experimental set-up, to developing techniques and

identifying relevant measures, to actually creating a collision between two jamming fronts. This work is intended to contribute to the existing literature on dynamic shear jamming in particular, and provide new insights into the fascinating and broad subject of dense suspension research in general.

## Chapter 2

# Experiments and Material

### 2.1 The suspension

Cornstarch-water suspensions are known to exhibit dynamic shear jamming (Peters et al., 2016). In this section the fundamental properties of the material used in this study are summarized. Several studies have explored the steady state properties of cornstarch-water suspensions (Fall et al., 2008, 2012, 2015; Brown and Jaeger, 2009). It is a commonly used material for studying transient shear jamming front phenomena (Waitukaitis and Jaeger, 2012; Peters and Jaeger, 2014; Peters et al., 2016; Han et al., 2016, 2018, 2019b,a), which is the reason for its use here.

Throughout this work cornstarch (*Maizena Maisstivelse*) is used as the solid phase of the suspension, while a 50 % by weight water-sucrose solution is used as the liquid phase. The volume fraction of a sample is calculated from the measured liquid ( $m_l$ ) and solid ( $m_s$ ) masses as

$$\phi = \frac{(1 - \beta)m_s/\rho_s}{(1 - \beta)m_s/\rho_s + m_l/\rho_l + \beta m_s/\rho_w}, \quad (2.1)$$

where  $\beta$  represents the starch water content, while  $\rho_s$ ,  $\rho_l$  and  $\rho_w$  represent the solid, liquid and water densities respectively. Cornstarch particles are porous, which in some studies is corrected for by  $\phi_V = \phi/(1 - \xi)$  where the porosity is measure to be  $\xi = 0.31$  for cornstarch (Han et al., 2017). Here, we report the value calculated from equation (2.1), without adjustment. Estimating  $\phi$  is notoriously difficult for cornstarch suspensions. Uncertainty and batch-to-batch variation in  $\beta$  might cause small variations in  $\phi$ , which can have significant impact on measured quantities. This is particularly

Parameter	Value	Parameter	Value
$\rho_l$ [kg m <sup>-3</sup> ]	1230	$\phi_0$ [-]	0.400
$\rho_w$ [kg m <sup>-3</sup> ]	995	$\phi_m$ [-]	0.327
$\rho_s$ [kg m <sup>-3</sup> ]	1630	$\Sigma^*$ [Pa]	10.2
$\eta_0$ [Pa s]	0.016	$\beta$ [-]	0.09 - 0.11
$d_s$ [m]	$15 \times 10^{-6}$	$\xi$ [-]	0.31

Table 2.1: Physical parameters for the suspension of cornstarch and sucrose-water solution.

pronounced in the dense regime close to  $\phi_0$  where the apparent viscosity diverges. As such, some studies simply report the weight rather than the volume fraction (Hermes et al., 2016; Maharjan et al., 2021) or use measured quantities such as the onset shear rate for DST (Maharjan and Brown, 2017) or the front propagation factor (Peters and Jaeger, 2014).

The steady state properties of the suspension are measured in a stress controlled parallel plate rheometer, details of which can be found in *Article I*. The goal is to identify the volume fraction range where dynamic jamming occurs. In summary, measurements over a wide range of volume fractions are fitted to the Wyart and Cates (2014) model, which establishes both the critical volume fractions  $\phi_m$  and  $\phi_0$ , as well as the onset stress,  $\Sigma^*$  (Han et al., 2018; Baumgarten and Kamrin, 2019a). Properties of the material used here are presented in table 2.1. As a result, for the remainder of this work the focus is on volume fractions in the range  $\phi_m < \phi < \phi_0$  where a shear jammed state is accessible.

To avoid the effects of gravity, a common practice is density matching the solid and fluid phase, particularly for long duration experiments (Merkel et al., 2004; Fall et al., 2008; Pan et al., 2015; Saint-Michel et al., 2018). However, as starch particles are small, gravitational forces have little effect on the system and depending on the experiment (Waitukaitis and Jaeger, 2012; Hermes et al., 2016; James et al., 2018) a perfect density matching might not be necessary (Brown and Jaeger, 2012, 2014). Pressure caused by gravitational forces could influence the onset of shear thickening (Brown and Jaeger, 2012, 2014). However, here  $\Delta\rho g d_s \ll \Sigma^*$  and should not influence the lubrication-frictional transition. The use of a sucrose solution as the liquid phase is deliberately employed here to mitigate settling over time. In transient experiments,  $\phi \geq 0.35$  is used, well within the dynamic jamming range. Accounting for porosity, the settling velocity when left undisturbed  $u_s(\phi) \approx u_s(0)(1 - \phi_V)^{3.7}$  is  $\sim 10^{-7}$  m/s (Richardson and Zaki, 1997), which

results in a total settling distance of a few particle diameters from the time a sample is loaded until it is discarded and thus considered negligible here.

This section has presented the material used in this study. The constituents are readily available (cornstarch, sucrose and water), making it feasible to mix large quantity batches. Through steady state measurements of the suspensions rheological properties, the range of volume fractions where dynamic jamming occurs has been identified, and thus where the focus will be in the remainder of this work.

## 2.2 Jamming front experiments

Experimental studies on dynamic shear jamming fronts are readily available in the literature (Waitukaitis and Jaeger, 2012; Peters and Jaeger, 2014; Peters et al., 2016; Han et al., 2016; Majumdar et al., 2017; Han et al., 2018, 2019b,a). As noted in section 1.2.2, both free surface (Peters and Jaeger, 2014; Peters et al., 2016; Han et al., 2018), X-ray (Waitukaitis and Jaeger, 2012) and ultrasound PIV (Han et al., 2016; Majumdar et al., 2017; Han et al., 2019b) have been used to extract time resolved velocity fields. Though the latter two are capable of visualizing the internal flow field, X-ray and ultrasound suffer from temporal (Waitukaitis, 2015) or spatial (Han, 2020) limitations, respectively. Some of these limitations can be avoided by constructing an approximately two dimensional system (Peters and Jaeger, 2014; Han et al., 2018). In such systems, the layer of suspension floats on top of a high density, low viscosity oil (Fluorinert) similar to Loimer et al. (2002), creating a near stress free bottom boundary. Velocities are measured by the movement of the optically accessible free surface, and both spatial and temporal limitations are set by the resolution and frame rate of the camera, exceeding those of X-ray and ultrasound imaging

In this work we are ultimately studying the collision of jamming fronts created from two perturbing bodies. The development of the flow in the collision region is studied without the interference of the confining boundary. The domain used here needs to be sufficiently large, such that the jamming front can freely propagate through the suspension before colliding with the solid boundary of our domain. As such, an approximate 2D set-up similar to Peters and Jaeger (2014) is utilized here. This allows for a relatively large measurement domain with a high temporal and spatial resolution for the PIV measurements capturing the suspension movement. Throughout this work, time-resolved planar PIV has been conducted, which yields a 2D realization of the flow. As such no information of the vertical movement is captured by this technique. However, as demonstrated by Peters and

Jaeger (2014), the momentum change in such systems based on the planar velocities match almost perfectly with the force measured at the perturbing body confirming that the system is a satisfactory 2D approximation.

### 2.2.1 Experimental Rig

The laboratory set-up employed herein consist of a traverse (Bosch-Rexroth MKR 15-65) towing a (two) partially submerged cylinder(s) through a layer of cornstarch suspension. The suspension floats atop a layer of high density ( $\rho = 1.7$  g/ml), low viscosity ( $\nu = 0.7$  cSt) oil (Fluorinert, FC-74). The domain is illuminated by LEDs and images of the suspension surface are captured with high-speed cameras (4-megapixels at 1080 fps, Photron FASTCAM Mini WX100). With this set-up, both the velocity field and the surface texture are captured, and only minor adjustments to the lighting is needed to change between the two techniques. In short, the velocity field is captured using PIV. The suspension surface is seeded with black pepper serving as tracer particles (Peters and Jaeger, 2014; Peters et al., 2016; Han et al., 2018), while the illumination by the LEDs is indirect. In order to enhance the visibility of the surface features, the surface is not seeded while a back lit semi-transparent acrylic plate is deliberately positioned such that the cameras capture the direct reflection of the suspension surface. The acrylic plate ensures a near homogeneous illumination of the suspension. A schematic of the lab set-up, with resulting raw particle and texture images are presented in figure 2.1. A detailed description of the experimental set-up is provided in the articles appended to this thesis. *Article I* presents the PIV set-up, while *Article II* and *III* describes the adjustments needed in order to enhance the visibility of the surface features.

Experiments conducted in *Article I* had a domain size of  $0.36 \text{ m} \times 0.31 \text{ m}$ . In order to study multiple perturbing bodies without interference of the boundary, a larger domain was needed. As such, in *Articles II* and *III* we employed a domain size of  $1 \text{ m} \times 0.5 \text{ m}$ . Different regions of the domain are investigated and a summary is provided in figure 2.2.

### 2.2.2 Preparation and Protocol

A large batch of suspension was mixed at a specific volume fraction (equation (2.1)) in a cement mixer. In order for the mixture to become homogeneous and to allow for the porous starch particles to fully soak in the liquid, the suspension was mixed for a minimum of an hour. A sample from the batch was extracted whenever an experiment was conducted. As noted in section 2.1, the solid and liquid phase are not perfectly density matched,

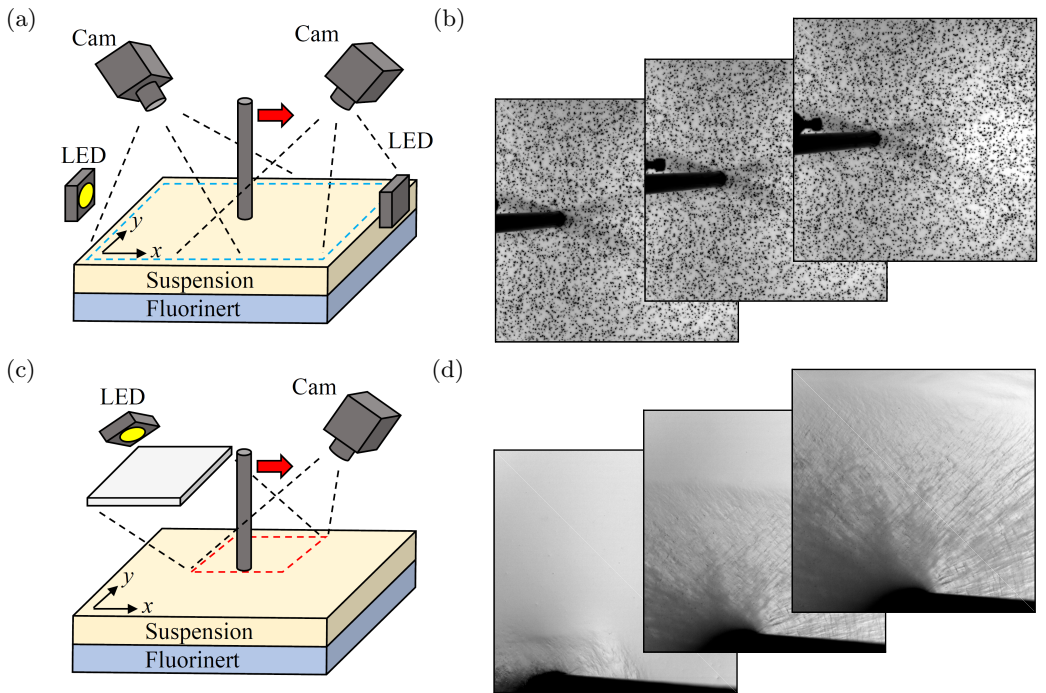


Figure 2.1: Schematic representation of the single cylinder experiment. (a) The PIV set-up with (b) resulting particle images and (c) the texture set-up with (d) resulting texture images

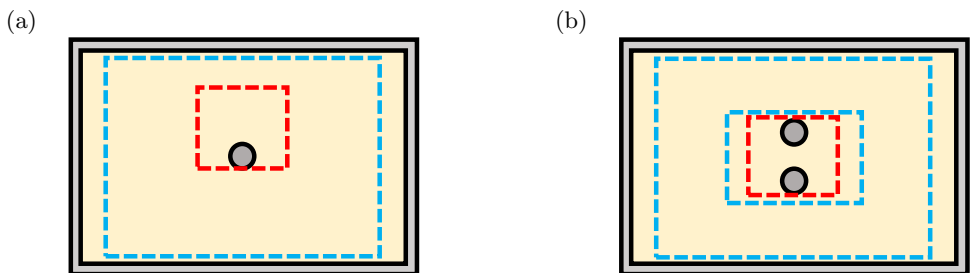


Figure 2.2: Birds eye view of the experimental set-up. Blue squares indicates the regions used for PIV while red squares indicate the region used for texture measurements. (a) Single cylinder set-up with the region of analysis employed in *Article I* and *Article II*. (b) Two cylinder set-up for studying colliding jamming fronts with the region of analysis employed in *Article III*.



thus the time span of an experiment was such that settling is not expected to influence the behaviour. In a rheometer configuration, [Hermes et al. \(2016\)](#) employed a 50 % glycerol solution ( $\eta_0 = 6$  mPa s, density  $\rho_l = 1.17$  g/ml) and reported settling effects after 30 min. Similarly, [Brown and Jaeger \(2012\)](#) with both a  $\eta_0 = 1$  mPa s,  $\rho_l = 1.41$  g/ml and a  $\eta_0 = 80$  mPa s,  $\rho_l = 1.34$  g/ml liquid phase reports settling time to be several hours. In our experiments, from loading to discarding the sample is limited to 15 minutes, which results in an estimated settling distance of a few particle diameters, and is considered negligible. The protocol employed herein is as follows:

1. A batch of suspension was mixed as described above and a sample was loaded into the tank floating on the layer of Fluorinert.
2. The suspension surface was seeded with black pepper which served as tracer particles for the PIV analysis.
3. The sample is pre-sheared at the driving speed ( $U_0$ ) back/forth in the lab frame four times in order to reach a repeatable state.
4. For an experimental run,
  - (a) The cylinder was driven back (or forth) in the lab frame at the driving speed,  $U_0$ .
  - (b) The high speed cameras were triggered once the cylinder movement is initiated.
  - (c) For the subsequent experimental run, the cylinder is driven forth (or back) in the lab frame at the driving speed,  $U_0$ .
5. When the camera memory was full (typically 12-14 runs, depending on frame rate and duration), the recordings were stored and the sample discarded. A new sample was loaded, and the procedure was repeated.

Though the cylinder was translated “back” or “forth” in the lab frame, the field of view was rotated during post processing such that the cylinder is always presented as translating in the positive  $x$ -direction. More details regarding how the data was processed are presented in chapter 3.

Pre-shearing is a common practice in rheological measurements ([Brown and Jaeger, 2009, 2012](#); [Fernandez et al., 2013](#)) in order to avoid effects of the specific loading procedure. A similar approach is employed with the protocol used here. As indicated by [Han et al. \(2018\)](#), some anisotropy is expected to be retained in the suspension, which here results in a somewhat slower front propagation than what is expected from the 1D model by [Han et al. \(2019a\)](#). In a small sample subjected to impact ([Han et al., 2019b](#)), a gentle shake between experimental runs was applied. Further discussion is

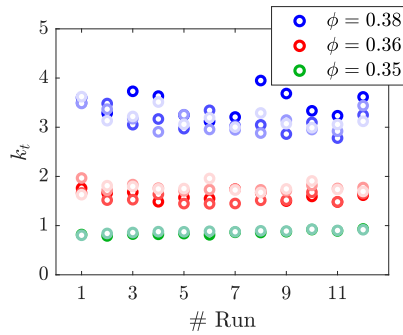


Figure 2.3: Front propagation in the transverse direction ( $k_t$ ) relative to the cylinder velocity for several batches. Color intensity represents different samples from the same batch and the  $x$ -axis indicates the experimental run.

provided in *Article I*. Here, we emphasise the repeatability where the specific deformation history is effectively the same for all experimental runs.

The protocol outlined above results in a repeatable measurement for each batch. Figure 2.3 shows front propagation (see section 1.2.2) for three batches with different samples and experimental runs indicated on the plot. It is worth noting that even though there might be several hours between the first and last sample from a batch, the results are highly repeatable, as demonstrated by figure 2.3.



# Chapter 3

## Methods

### 3.1 Particle image velocimetry

Particle image velocimetry (PIV) is an optical method for the quantification of instantaneous flow fields. From images of the fluid movement, the PIV algorithm is a statistical method for determining the local displacement of features in the flow between consecutive images. In order to observe the movement of the fluid, the material is seeded with tracer particles. It is the movement of ensembles of tracer particles that gives the displacement between frames. This work does not attempt to give a complete review on the vast number of techniques or applications of PIV. The reader is instead referred to the book by [Raffel et al. \(2018\)](#), which gives an excellent introduction and an extensive overview of the subject. Rather, the basic concept of PIV is presented here. In addition, how the measurements are processed for our application is also presented in order to give the reader an overview of how the results are arrived at.

In contrast to measuring velocity with probes inserted into the flow such as pitot tubes or hot wires, PIV is non-intrusive. Rather than giving measurements at one location in the flow, PIV yields a discrete velocity field limited by the size and resolution of the recording and the ability to illuminate the field of interest. As the suspension is opaque, gaining optical access inside the bulk suspension is challenging. As noted in section [1.2.2](#) both X-ray and ultrasound techniques have been developed for quantifying the movement inside the suspension ([Waitukaitis and Jaeger, 2012](#); [Han et al., 2016, 2019b](#)). However, due to temporal and size limitations of these techniques, the approach used here measures velocities at the free surface ([Peters and](#)

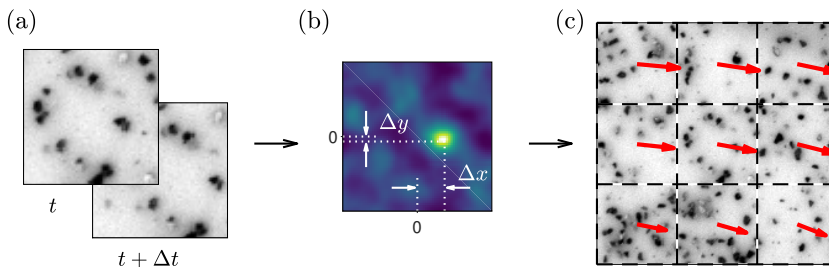


Figure 3.1: PIV evaluation. (a) Interrogation windows from two consecutive images. (b) Cross correlation between the two interrogation windows. The displacement between the frames is measured by the location of the peak. (c) Resulting vectors for several interrogation windows.

Jaeger, 2014; Peters et al., 2016; Han et al., 2018). Details regarding the experimental set-up employed in the current work, as well as justification of its use, can be found in section 2.2.

In order to evaluate the PIV recordings, the images are divided into sub-areas named *interrogation windows*. The ensemble displacement of tracer particles in an interrogation window is determined by the location of the peak in the cross-correlation between two consecutive images. The velocity is thus determined from the displacement and time step between images. Repeating this for all interrogation windows yields a discrete velocity field for the whole field of view. Figure 3.1 shows the process presented above. The results are shown in the image plane and a calibration is needed in order to map the results into the spatial plane.

### 3.1.1 Processing

Here, the commercially available software DaVis 8.4.0 from LaVision was used to evaluate the PIV recordings. Recordings were done at two magnifications in this work. A coarse and fine grained pepper were used as tracer particles for the large and small field of view, respectively, ensuring that the minimum recommended,  $\sim 10$ , tracers particles are within in the smallest interrogation windows (Raffel et al., 2018). A multi pass evaluation of the images was performed. The processing varied slightly depending on the experiment. However, 2-3 passes at  $96 \times 96$  pixel interrogation window, followed by 2-3 passes with a circular interrogation window with decreasing size between passes ending at  $48 \times 48$  pixels typically yielded a final correlation coefficient  $> 0.9$ . In order to decrease the final vector spacing of the velocity field, a 50 % overlap between neighbouring interrogation windows

was used here.

To achieve full optical access around the perturbing body, two cameras with partially overlapping fields of view were used; one in front of, and one behind the perturbing body as seen in figure 2.1. The PIV evaluation thus yields two time resolved velocity fields, which were stitched together. The velocities in the overlapping region are a weighted average between the fore ( $\mathbf{u}_F$ ) and aft velocity fields ( $\mathbf{u}_A$ ).

$$\mathbf{u} = w_{S,F}\mathbf{u}_F + w_{S,A}\mathbf{u}_A, \quad \text{where} \quad w_{S,F} + w_{S,A} = 1. \quad (3.1)$$

The basic stitching concept is shown in figure 3.2 for the velocity component in the  $x$ -direction. The width of the stitch region covers  $\sim 15\%$  of the field of view where the stitch weights were a smooth transition between zero and unity. The cylinder and the mounting mechanism partially blocked the field of view in the fore and aft frames. From the original particle images, a mask was defined such that the regions where this occurred could be identified. If the field of view was blocked in the fore (aft) frame the weight function was set to zero for the fore (aft) frame and unity for the aft (fore) frame. The region optically obstructed in both frames coincided with the location where the cylinder penetrated the free surface. As such, values in this region are ignored for the remainder of this work.

The velocity fields were time filtered. At each spatial node, the velocity time series was convolved with a moving Hanning window  $u_{\text{Filtered}} = u_{\text{Raw}} * w_H$ . The weights ( $w_H$ ) were defined by the Hanning function, which is normalized such the sum of the weights added to unity. Figure 3.3a shows an example of a measured velocity time series and a weight function. The filtered velocity depended on the window size of the weight function, as shown in figure 3.3b. In this example a window size of 31 frames removed the majority of the noise, without attenuating the signal in the fast changing region.

### 3.1.2 Kinematic properties

As noted in chapter 1, the local strain rate and accumulated strain are important measures for these types of flows. The material deforms differently depending on the location in the flow. As such we will use a tensorial measure of the strain, which allows us to not only quantify the amount the material has deformed, but also in which direction. The PIV analysis gives time resolved, two dimensional velocity fields  $\mathbf{u}(\mathbf{x}, t)$  and is the basis from which the strains and strain rates are estimated.

The scalar instantaneous strain rate,  $\dot{\gamma}$ , is calculated directly from the velocity fields. The velocity gradient tensor ( $\nabla\mathbf{u}$ ) is estimated with a second

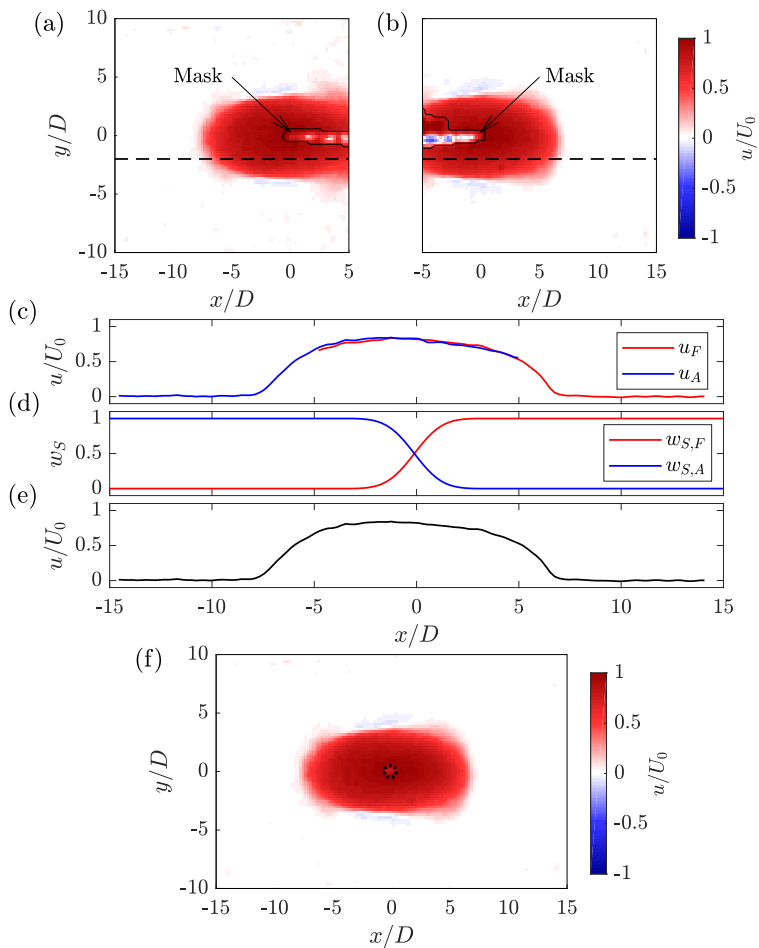


Figure 3.2: Stitching process. (a) Aft ( $u_A$ ) and (b) fore ( $u_F$ ) velocity fields. The region optically obstructed by cylinder and mounting structure is indicated in each figure. (c) Velocity profiles taken at the dashed lines from the fore and aft views, as well as (d) fore and aft stitching weights ( $w_{S,F}$  and  $w_{S,A}$ ). (e) The resulting stitched velocity profile. (f) Shows the final velocity field.  $x$  and  $y$  are normalized with the cylinder diameter,  $D$ .

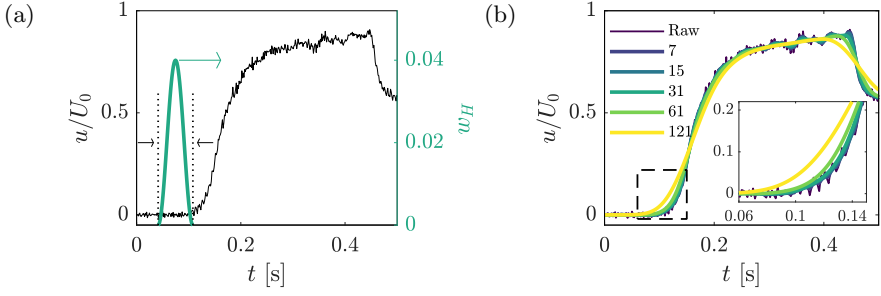


Figure 3.3: (a) Example weight function with window size of 31 frames and measured velocity. (b) filtered velocity for different window sizes. The inset shows a close up of the interval where the velocity is changing rapidly.

order central difference scheme. The rate of strain tensor is constructed as

$$\mathbf{D} = \frac{1}{2}(\nabla \mathbf{u} + (\nabla \mathbf{u})^T), \quad (3.2)$$

where the the scalar strain rate is calculated as (Irgens, 2008, 2014)

$$\dot{\gamma} = \sqrt{2\mathbf{D} : \mathbf{D}} = \sqrt{2D_{ij}D_{ij}}. \quad (3.3)$$

For a measure of local strain, inspiration is taken from common measures in solid mechanics. A starting point for measuring deformations is to know how neighbouring points in the material move relative to each other. The movement of a point following the material ( $\mathbf{x}_P = (x_P, y_P)$ ) is estimated from the PIV data by numerically integrating the velocity field

$$\mathbf{x}_P(\mathbf{X}, t) = \mathbf{X} + \int_0^t \mathbf{u}(\mathbf{x}_P(\tau), \tau) d\tau \quad (3.4)$$

where  $\mathbf{X} = \mathbf{x}_P(t = 0)$ . The deformation gradient tensor,  $\mathbf{F}$ , represents the relative movement of neighbouring material points and is calculated as

$$\mathbf{F} = \frac{\partial \mathbf{x}_P}{\partial \mathbf{X}} \quad (3.5)$$

which transforms a line element ( $\Delta \mathbf{X}$ ) from the undeformed to the deformed configuration as  $\Delta \mathbf{x}_P = \mathbf{F} \Delta \mathbf{X}$ . This is shown schematically in figure 3.4a. From a polar decomposition it is possible to separate out the rigid rotation and pure stretching components of the deformation gradient

$$\mathbf{F} = \mathbf{R}\mathbf{U} = \mathbf{V}\mathbf{R} \quad (3.6)$$



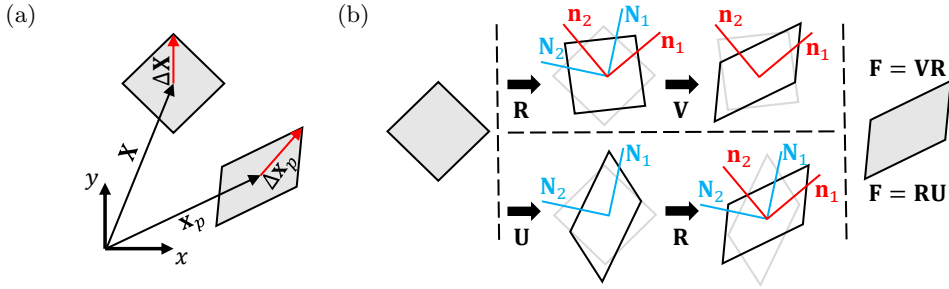


Figure 3.4: (a) A material parcel in the deformed and undeformed configurations. (b) Schematic representation of the polar decomposition, either as a pure stretch followed by a rigid rotation ( $\mathbf{R}\mathbf{U}$ ) or a rigid rotation followed by a pure stretch ( $\mathbf{V}\mathbf{R}$ ).

where the symmetric positive-definite tensors  $\mathbf{U}$  and  $\mathbf{V}$  are called the right- and left stretch tensors, and the proper orthogonal matrix  $\mathbf{R}$  represents rotation. Schematic representation of the polar decomposition is shown in figure 3.4b. The spectral representation of the stretch tensors is (Nemat-Nasser, 2004)

$$\mathbf{V} = \sum_i \lambda_i \mathbf{n}_i \otimes \mathbf{n}_i \quad \text{and} \quad \mathbf{U} = \sum_i \lambda_i \mathbf{N}_i \otimes \mathbf{N}_i \quad (3.7)$$

where  $\lambda_i$  are the eigenvalues of the stretches while  $\mathbf{n}_i$  and  $\mathbf{N}_i$  are the corresponding eigenvectors relative to the deformed and the undeformed configurations, respectively. Here a choice must be made whether the strain directions should be presented relative to the deformed (Eulerian) or undeformed (Lagrangian) configuration.

In this work, the strain will be presented along side and directly compared to instantaneous velocity fields captured as the suspension is deforming. As such, the left stretch tensor ( $\mathbf{V}$ ) will be used here moving forward. This has no consequence for the magnitude of stretch as  $\mathbf{U}$  and  $\mathbf{V}$  have the same principle values.

The logarithmic strain, from the Seth-Hill family of strain tensors, is used here as a strain measure. From the stretch tensor, the eigenvalues of the strain tensor are calculated as  $\zeta = (\lambda^{2m} - 1)/2m$ , where  $m$  is a real number. The limit  $m = 0$  yields  $\zeta = \ln(\lambda)$ , which is identified as the logarithmic strain. Using the left stretch ( $\mathbf{V}$ ) the Eulerian logarithmic strain tensor then becomes

$$\mathbf{e} = \sum_i \ln(\lambda_i) \mathbf{n}_i \otimes \mathbf{n}_i. \quad (3.8)$$

The eigenvalues are ordered ( $\ln(\lambda_1) > \ln(\lambda_2)$ ) such that the associated eigenvectors  $\mathbf{n}_1$  and  $\mathbf{n}_2$  represent direction of stretch and compression, respectively. Logarithmic strain is sometimes referred to as true-, natural- or Hencky strain, and more details can be found in the literature (Xiao et al., 1997; Nemat-Nasser, 2004; Rees, 2006; Butcher and Abedini, 2017).

As a scalar measure of the accumulated strain we use the norm of the strain tensor

$$\epsilon = \sqrt{\mathbf{e} : \mathbf{e}} = \sqrt{\ln(\lambda_1)^2 + \ln(\lambda_2)^2}. \quad (3.9)$$

In summary,  $\epsilon$  and the vectors  $\mathbf{n}_1$  and  $\mathbf{n}_2$  thus represent the magnitude and directions of strain.

## 3.2 Surface texture analysis

Particle image velocimetry is a powerful technique, from which it is possible to estimate local kinematic properties. However, since PIV captures the velocity field, no direct information on local stresses is retrieved from this method. As noted in section 1.3, dilation of a dense suspension is observable at the free surface as a smooth-matte transition if sufficiently high stress is applied to the sample (Bischoff White et al., 2010; Smith et al., 2010; Brown and Jaeger, 2012; Roché et al., 2013; Maharjan et al., 2021). In *Article III*, this feature is used to qualitatively identify high stress regions of the flow. *Article II* investigates the corrugations observed to form on the free surface of dense suspensions (Loimer et al., 2002; Timberlake and Morris, 2005). Here, a method is presented capable of quantifying the orientation of the corrugations. Neither of these aspects are captured by PIV, as the specific lighting condition is key with regards to emphasizing the visibility of these surface features. More details regarding the experimental set-up are found in section 2.2.1.

Previous investigations of the surface corrugation have calculated the power spectral density (PSD) of the surface images. Timberlake and Morris (2005) presented an inclined plane experiment, and from calculating two dimensional PSD show that the structures exhibit anisotropy. Specifically, the corrugations tend to be shorter in flow direction. In these experiments the surface normal is oriented in the direction of velocity gradient. Loimer et al. (2002) present an approximate 2D experiment more closely related to the set-up utilized in this thesis. In their work the suspension floats on a layer of Fluorinert and movement is driven by two parallel belts moving in opposite directions, producing a simple shear deformation with the surface normal in the vorticity direction. Loimer et al. (2002) present 1D PSD curves in the

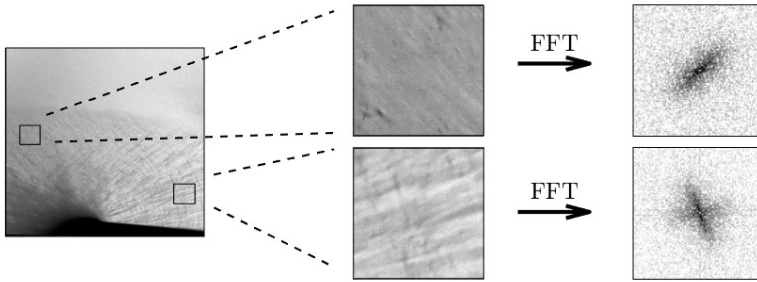


Figure 3.5: Surface corrugations in different parts of the flow, showing interrogation windows and resulting 2D PSD.

flow ( $x$ ) and gradient ( $y$ ) directions. Although an anisotropy is observed, it is unclear how these structures appear in the full 2D realisation of the PSD.

Both [Loimer et al. \(2002\)](#) and [Timberlake and Morris \(2005\)](#) present experiments where the bulk flow profile is relatively homogeneous in the region of analysis. This is not the case in the experiments presented in this work. As such, in order to gain local information of the surface features, the texture images are divided into interrogation windows, similar to the approach used in PIV. The PSD of an interrogation window is calculated as  $|\hat{I}|^2$ , where  $\hat{I}$  is the 2D *Fast Fourier Transform* (FFT) of the image intensity ( $I$ ). An example of a snapshot of the surface corrugations is given in figure 3.5. Even though the main flow direction is from left to right the orientation of the dominant surface features depend on the location in the flow. The PSD is the main building block for the method outlined in *Article II*, where the surface corrugations are compared to results acquired from PIV, particularly the local deformation.

## Chapter 4

# Summaries of the research articles and future work

This thesis has described an experimental study of dynamic jamming in dense suspensions, focusing on the transient response when perturbed by submerged cylinders. The work culminated in observing colliding jamming fronts and relevant methods and measures have been identified along the way. Chapter 1 presented the background and gave an overview of the recent studies on the subject, as well as motivated the topics that are investigated here. The experimental set-up, material and measurement devices used throughout this study were presented in Chapter 2. The experiments were deliberately designed to produce two dimensional jamming fronts and as such the movement and features of the free surface are used to characterize the state of the suspension. A relatively large measurement domain ( $1 \text{ m} \times 0.5 \text{ m}$ ) is employed herein, making it possible to investigate the response of the suspension without effects of the confining boundary. Chapter 3 provided an overview of the methods and measures used throughout this work.

In the next part of the thesis, the novel contributions of this work are presented as three articles. Common to the articles is that they all focus on the transient response of a dense suspension undergoing dynamic jamming. *Article I* and *II* focus on a single cylinder set-up, while in *Article III* a second perturbing body is introduced. Although a scalar measure of strain is sufficient when describing a freely propagating jamming front, a recurring theme throughout this work is how a tensorial strain measure can be a useful tool for understanding the response in more complex flows and geometries

undergoing dynamic jamming.

### *Article I*

#### **Getting jammed in all directions: Dynamic shear jamming around a cylinder towed through a dense suspension**

Olav Rømcke, Ivo R. Peters, R. Jason Hearst

*Physical Review Fluids*, **6**, 063301.

*Article I* introduces the experimental configuration and material used throughout this work. From rheometer measurements we identify the volume fractions where a dynamically jammed state can be accessed for our suspension. The experimental set-up consists of a single cylinder submerged into a layer of cornstarch suspension. The suspension itself floats on top of a high density, low viscosity oil which ensures a close to stress-free bottom boundary. This ensures that the front propagates in an approximately two-dimensional manner.

The velocity field is measured using particle image velocimetry on the free surface, where black pepper serves as tracer particles. Two cameras view the suspension, such that stitching the two resulting velocity fields gives a full view of the suspension surface. By varying the driving speed of the cylinder, we identify the region where jamming front propagation and cylinder velocity are independent. Though the fields are symmetric in the transverse direction relative to the cylinder velocity, we observe a fore-aft asymmetry, which we attribute to the moderately large strains observed in our system.

### *Article II*

#### **Characterizing the surface texture of a dense suspension undergoing dynamic jamming**

Olav Rømcke, Ivo R. Peters, R. Jason Hearst

*Experiments in Fluids*, **62**, 226

In this work the surface texture on the free surface as the suspension transitions into a jammed state is investigated. The suspension is perturbed by a single cylinder, and the focus is on the region next to the cylinder. Particle image velocimetry is used as a reference, while the primary focus is on high speed photography of the free surface. Here, a method is developed which

allows us to quantify the free surface features. In short, both how dominant the features are and in what direction they are oriented is extracted from the two dimensional fast Fourier transform of localised windows.

The surface features provide a clear visual difference between the quiescent and solid-like regions. By calculating the dot product between the eigenvectors of the strain tensor and the orientation vector of the surface features it is shown that the the surface features have a strong preference towards being oriented tangential or normal to the eigenvectors.

### *Article III*

#### **Collision of dynamic jamming fronts in a dense suspension**

Olav Rømcke, Ivo R. Peters, R. Jason Hearst

*Physical Review Fluids*, **6**, 103301

The work presented here is an extension of *Articles I* and *II* where we now introduce two perturbing bodies moving in parallel. The jamming fronts propagate from each cylinders as expected from our previous work and at some point the two fronts collide between the cylinders. Particle image velocimetry is used to capture the velocity field, while high speed images capture of the surface texture. As PIV only gives kinematic properties, the observed texture change on the free surface is used as a qualitative tool in order to assess the stress state of the suspension. Interestingly, we show that the region between the cylinders relaxes back to a quiescent, unstressed state after collision.

The accumulated strain and the surface texture images indicate different regions. This apparent discrepancy between the two measures is attributed to the fact that the strain does not account for the subsequent relaxation of the suspension. However, by plotting lines tangential to the eigenvectors of the strain tensor, it is shown that the shape of the quiescent region follows lines of principle strain.

## Future work

There are several interesting directions in which the work conducted in this thesis can be extended in the future. Throughout this work, cylinders have been used as the perturbing bodies. How the suspension would respond to different shapes, or if the cylinders move in different directions have not been explored. As demonstrated here, there is a close connection between eigenvectors of the strain tensor and the unjammed diamond shaped region after collision (*Article III*). Exploring different geometries and direction of perturbation could answer questions with regards to the robustness of our result.

The structures of the surface have been investigated by simple high speed images of the surface. Though the orientation of these features are quantified (*Article II*), our measurements provide no information on the out-of-plane displacement of these structures. Several non-intrusive methods are available, which could provide out-of-plane information. Stereoscopic PIV is one such approach which in addition to the planar components also measures velocity normal to the calibration plane. However, methods such as Fourier transform profilometry measure out of plane displacements directly. Though the latter method yields no information on the velocity field it could be an interesting approach with regards to investigating the surface topology.

The focus here has been on macroscopic quantities, as the resolution of our measurements is several times larger than the size of the particles. However, the free surface is an interesting boundary. Shear induced normal stresses distort the surface while surface tension provides a confining stress as the material is deformed. As shown both here and in the literature, these features are highly anisotropic and exist over a range of scales. How the surface topology is connected to the underlying granular micro structure could potentially be a fruitful endeavour for future research.

This work has focused on planar measurements in a 2D set-up. As such, an interesting extension would be to investigate how the concepts studied here behave in three dimensions. In this work, the dilation observed at the free surface is used to qualitatively assess the local stress state of the system, which would not be feasible in the 3D case. However, investigating the form of the full 3D strain tensor would be an important extension to this work.

# Bibliography

- B. Allen, B. Sokol, S. Mukhopadhyay, R. Maharjan, and E. Brown. System-spanning dynamically jammed region in response to impact of cornstarch and water suspensions. *Phys. Rev. E*, 97:052603, May 2018. doi: 10.1103/PhysRevE.97.052603. URL <https://link.aps.org/doi/10.1103/PhysRevE.97.052603>.
- H. A. Barnes. Shear-thickening (“dilatancy”) in suspensions of nonaggregating solid particles dispersed in newtonian liquids. *Journal of Rheology*, 33(2):329–366, 1989. doi: 10.1122/1.550017. URL <https://doi.org/10.1122/1.550017>.
- G. K. Batchelor and J. T. Green. The determination of the bulk stress in a suspension of spherical particles to order  $c^2$ . *Journal of Fluid Mechanics*, 56(3):401–427, 1972. doi: 10.1017/S0022112072002435.
- A. S. Baumgarten and K. Kamrin. A general constitutive model for dense, fine-particle suspensions validated in many geometries. *Proceedings of the National Academy of Sciences*, 116(42):20828–20836, 2019a. ISSN 0027-8424. doi: 10.1073/pnas.1908065116. URL <https://www.pnas.org/content/116/42/20828>.
- A. S. Baumgarten and K. Kamrin. A general fluid–sediment mixture model and constitutive theory validated in many flow regimes. *Journal of Fluid Mechanics*, 861:721–764, 2019b. doi: 10.1017/jfm.2018.914.
- R. P. Behringer and B. Chakraborty. The physics of jamming for granular materials: a review. *Reports on Progress in Physics*, 82(1):012601, nov 2018. doi: 10.1088/1361-6633/aadc3c. URL <https://doi.org/10.1088/1361-6633/aadc3c>.



- E. Bertrand, J. Bibette, and V. Schmitt. From shear thickening to shear-induced jamming. *Phys. Rev. E*, 66:060401, Dec 2002. doi: 10.1103/PhysRevE.66.060401. URL <https://link.aps.org/doi/10.1103/PhysRevE.66.060401>.
- D. Bi, J. Zhang, B. Chakraborty, and R. P. Behringer. Jamming by shear. *Nature*, 480(7377):355, 2011. ISSN 0028-0836. doi: 10.1038/nature10667. URL <https://doi.org/10.1038/nature10667>.
- E. E. Bischoff White, M. Chellamuthu, and J. P. Rothstein. Extensional rheology of a shear-thickening cornstarch and water suspension. *Rheologica acta*, 49(2):119–129, 2010. ISSN 0035-4511.
- F. Boyer, E. Guazzelli, and O. Pouliquen. Unifying suspension and granular rheology. *Phys. Rev. Lett.*, 107:188301, Oct 2011. doi: 10.1103/PhysRevLett.107.188301. URL <https://link.aps.org/doi/10.1103/PhysRevLett.107.188301>.
- J. F. Brady and G. Bossis. The rheology of concentrated suspensions of spheres in simple shear flow by numerical simulation. *Journal of Fluid Mechanics*, 155:105–129, 1985. doi: 10.1017/S0022112085001732.
- E. Brown and H. M. Jaeger. Dynamic jamming point for shear thickening suspensions. *Phys. Rev. Lett.*, 103:086001, Aug 2009. doi: 10.1103/PhysRevLett.103.086001. URL <https://link.aps.org/doi/10.1103/PhysRevLett.103.086001>.
- E. Brown and H. M. Jaeger. The role of dilation and confining stresses in shear thickening of dense suspensions. *Journal of Rheology*, 56(4):875–923, 2012. doi: 10.1122/1.4709423. URL <https://doi.org/10.1122/1.4709423>.
- E. Brown and H. M. Jaeger. Shear thickening in concentrated suspensions: phenomenology, mechanisms and relations to jamming. *Reports on Progress in Physics*, 77(4):046602, 2014. ISSN 0034-4885.
- E. Brown, H. Zhang, N. A. Forman, B. W. Maynor, D. E. Betts, J. M. DeSimone, and H. M. Jaeger. Shear thickening and jamming in densely packed suspensions of different particle shapes. *Phys. Rev. E*, 84:031408, Sep 2011. doi: 10.1103/PhysRevE.84.031408. URL <https://link.aps.org/doi/10.1103/PhysRevE.84.031408>.
- C. Butcher and A. Abedini. Shear confusion: Identification of the appropriate equivalent strain in simple shear using the logarithmic

- strain measure. *International Journal of Mechanical Sciences*, 134:273–283, 2017. ISSN 0020-7403. doi: <https://doi.org/10.1016/j.ijmecsci.2017.10.005>. URL <https://www.sciencedirect.com/science/article/pii/S0020740317320817>.
- M. E. Cates, J. P. Wittmer, J.-P. Bouchaud, and P. Claudin. Jamming, force chains, and fragile matter. *Phys. Rev. Lett.*, 81:1841–1844, Aug 1998. doi: 10.1103/PhysRevLett.81.1841. URL <https://link.aps.org/doi/10.1103/PhysRevLett.81.1841>.
- C. Clavaud, A. Bérut, B. Metzger, and Y. Forterre. Revealing the frictional transition in shear-thickening suspensions. *Proceedings of the National Academy of Sciences*, 114(20):5147–5152, 2017. ISSN 0027-8424. doi: 10.1073/pnas.1703926114. URL <https://www.pnas.org/content/114/20/5147>.
- J. Comtet, G. Chatte, A. Nigues, L. Bocquet, A. Siria, and A. Colin. Pairwise frictional profile between particles determines discontinuous shear thickening transition in non-colloidal suspensions. *Nature communications*, 8(1):15633–15633, 2017. ISSN 2041-1723.
- E. DeGiuli, G. Düring, E. Lerner, and M. Wyart. Unified theory of inertial granular flows and non-brownian suspensions. *Phys. Rev. E*, 91:062206, Jun 2015. doi: 10.1103/PhysRevE.91.062206. URL <https://link.aps.org/doi/10.1103/PhysRevE.91.062206>.
- M. M. Denn, J. F. Morris, and D. Bonn. Shear thickening in concentrated suspensions of smooth spheres in newtonian suspending fluids. *Soft Matter*, 14:170–184, 2018. doi: 10.1039/C7SM00761B. URL <http://dx.doi.org/10.1039/C7SM00761B>.
- R. G. Egres and N. J. Wagner. The rheology and microstructure of acicular precipitated calcium carbonate colloidal suspensions through the shear thickening transition. *Journal of Rheology*, 49(3):719–746, 2005. doi: 10.1122/1.1895800. URL <https://doi.org/10.1122/1.1895800>.
- R. G. Egres, F. Nettekheim, and N. J. Wagner. Rheo-sans investigation of acicular-precipitated calcium carbonate colloidal suspensions through the shear thickening transition. *Journal of Rheology*, 50(5):685–709, 2006. doi: 10.1122/1.2213245. URL <https://doi.org/10.1122/1.2213245>.
- A. Einstein. Eine neue bestimmung der moleküldimensionen. *Annalen der Physik*, 324(2):289–306, 1906. doi: <https://doi.org/10.1002/andp>.

19063240204. URL <https://onlinelibrary.wiley.com/doi/abs/10.1002/andp.19063240204>.

- A. Einstein. Berichtigung zu meiner arbeit: Eine neue bestimmung der moleküldimensionen. *Annalen der Physik*, 14(S1):406–407, 1911. doi: <https://doi.org/10.1002/andp.200590031>. URL <https://onlinelibrary.wiley.com/doi/abs/10.1002/andp.200590031>.
- A. Fall, N. Huang, F. Bertrand, G. Ovarlez, and D. Bonn. Shear thickening of cornstarch suspensions as a reentrant jamming transition. *Phys. Rev. Lett.*, 100:018301, Jan 2008. doi: 10.1103/PhysRevLett.100.018301. URL <https://link.aps.org/doi/10.1103/PhysRevLett.100.018301>.
- A. Fall, F. Bertrand, G. Ovarlez, and D. Bonn. Shear thickening of cornstarch suspensions. *Journal of Rheology*, 56(3):575–591, 2012. doi: 10.1122/1.3696875. URL <https://doi.org/10.1122/1.3696875>.
- A. Fall, F. Bertrand, D. Hautemayou, C. Mezière, P. Moucheront, A. Lemaître, and G. Ovarlez. Macroscopic discontinuous shear thickening versus local shear jamming in cornstarch. *Phys. Rev. Lett.*, 114:098301, Mar 2015. doi: 10.1103/PhysRevLett.114.098301. URL <https://link.aps.org/doi/10.1103/PhysRevLett.114.098301>.
- N. Fernandez, R. Mani, D. Rinaldi, D. Kadau, M. Mosquet, H. Lombois-Burger, J. Cayer-Barrioz, H. J. Herrmann, N. D. Spencer, and L. Isa. Microscopic mechanism for shear thickening of non-brownian suspensions. *Phys. Rev. Lett.*, 111:108301, Sep 2013. doi: 10.1103/PhysRevLett.111.108301. URL <https://link.aps.org/doi/10.1103/PhysRevLett.111.108301>.
- F. Ferrini, D. Ercolani, B. de Cindio, L. Nicodemo, L. Nicolais, and S. Ranaudo. Shear viscosity of settling suspensions. *Rheologica acta*, 18(2):289–296, 1979. ISSN 0035-4511.
- W. J. Frith, P. d’Haene, R. Buscall, and J. Mewis. Shear thickening in model suspensions of sterically stabilized particles. *Journal of Rheology*, 40(4):531–548, 1996. doi: 10.1122/1.550791. URL <https://doi.org/10.1122/1.550791>.
- F. Gadala-Maria and A. Acrivos. Shear-induced structure in a concentrated suspension of solid spheres. *Journal of Rheology*, 24(6):799–814, 1980. doi: 10.1122/1.549584. URL <https://doi.org/10.1122/1.549584>.

- J. J. J. Gillissen, C. Ness, J. D. Peterson, H. J. Wilson, and M. E. Cates. Constitutive model for time-dependent flows of shear-thickening suspensions. *Phys. Rev. Lett.*, 123:214504, Nov 2019. doi: 10.1103/PhysRevLett.123.214504. URL <https://link.aps.org/doi/10.1103/PhysRevLett.123.214504>.
- E. Guazzelli and O. Pouliquen. Rheology of dense granular suspensions. *Journal of Fluid Mechanics*, 852:P1, 2018. doi: 10.1017/jfm.2018.548.
- B. M. Guy, M. Hermes, and W. C. K. Poon. Towards a unified description of the rheology of hard-particle suspensions. *Phys. Rev. Lett.*, 115:088304, Aug 2015. doi: 10.1103/PhysRevLett.115.088304. URL <https://link.aps.org/doi/10.1103/PhysRevLett.115.088304>.
- B. M. Guy, C. Ness, M. Hermes, L. J. Sawiak, J. Sun, and W. C. K. Poon. Testing the wyart–cates model for non-brownian shear thickening using bidisperse suspensions. *Soft Matter*, 16:229–237, 2020. doi: 10.1039/C9SM00041K. URL <http://dx.doi.org/10.1039/C9SM00041K>.
- E. Han. *Transient Dynamics of Concentrated Particulate Suspensions under Shear*. Springer Theses. Springer International Publishing AG, Cham, 2020. ISBN 3030383474.
- E. Han, I. R. Peters, and H. M. Jaeger. High-speed ultrasound imaging in dense suspensions reveals impact-activated solidification due to dynamic shear jamming. *Nature Communications*, 7(1), 2016. ISSN 2041-1723. doi: 10.1038/ncomms12243.
- E. Han, N. Van Ha, and H. M. Jaeger. Measuring the porosity and compressibility of liquid-suspended porous particles using ultrasound. *Soft Matter*, 13:3506–3513, 2017. doi: 10.1039/C7SM00182G. URL <http://dx.doi.org/10.1039/C7SM00182G>.
- E. Han, M. Wyart, I. R. Peters, and H. M. Jaeger. Shear fronts in shear-thickening suspensions. *Phys. Rev. Fluids*, 3:073301, Jul 2018. doi: 10.1103/PhysRevFluids.3.073301. URL <https://link.aps.org/doi/10.1103/PhysRevFluids.3.073301>.
- E. Han, N. M. James, and H. M. Jaeger. Stress controlled rheology of dense suspensions using transient flows. *Phys. Rev. Lett.*, 123:248002, Dec 2019a. doi: 10.1103/PhysRevLett.123.248002. URL <https://link.aps.org/doi/10.1103/PhysRevLett.123.248002>.

- E. Han, L. Zhao, N. Van Ha, S. T. Hsieh, D. B. Szyld, and H. M. Jaeger. Dynamic jamming of dense suspensions under tilted impact. *Phys. Rev. Fluids*, 4:063304, Jun 2019b. doi: 10.1103/PhysRevFluids.4.063304. URL <https://link.aps.org/doi/10.1103/PhysRevFluids.4.063304>.
- M. Hermes, B. M. Guy, W. C. K. Poon, G. Poy, M. E. Cates, and M. Wyart. Unsteady flow and particle migration in dense, non-brownian suspensions. *Journal of Rheology*, 60(5):905–916, 2016. doi: 10.1122/1.4953814. URL <https://doi.org/10.1122/1.4953814>.
- C. Heussinger. Shear thickening in granular suspensions: Interparticle friction and dynamically correlated clusters. *Phys. Rev. E*, 88:050201(R), Nov 2013. doi: 10.1103/PhysRevE.88.050201. URL <https://link.aps.org/doi/10.1103/PhysRevE.88.050201>.
- R. Hoffman. Discontinuous and dilatant viscosity behavior in concentrated suspensions. ii. theory and experimental tests. *Journal of Colloid and Interface Science*, 46(3):491–506, 1974. ISSN 0021-9797. doi: [https://doi.org/10.1016/0021-9797\(74\)90059-9](https://doi.org/10.1016/0021-9797(74)90059-9). URL <https://www.sciencedirect.com/science/article/pii/0021979774900599>.
- R. L. Hoffman. Discontinuous and dilatant viscosity behavior in concentrated suspensions. i. observation of a flow instability. *Transactions of the Society of Rheology*, 16(1):155–173, 1972. doi: 10.1122/1.549250. URL <https://doi.org/10.1122/1.549250>.
- R. L. Hoffman. Discontinuous and dilatant viscosity behavior in concentrated suspensions iii. necessary conditions for their occurrence in viscometric flows. *Advances in Colloid and Interface Science*, 17(1):161–184, 1982. ISSN 0001-8686. doi: [https://doi.org/10.1016/0001-8686\(82\)80017-1](https://doi.org/10.1016/0001-8686(82)80017-1). URL <https://www.sciencedirect.com/science/article/pii/0001868682800171>.
- R. L. Hoffman. Explanations for the cause of shear thickening in concentrated colloidal suspensions. *Journal of Rheology*, 42(1):111–123, 1998. doi: 10.1122/1.550884. URL <https://doi.org/10.1122/1.550884>.
- N. Huang, G. Ovarlez, F. Bertrand, S. Rodts, P. Coussot, and D. Bonn. Flow of wet granular materials. *Phys. Rev. Lett.*, 94:028301, Jan 2005. doi: 10.1103/PhysRevLett.94.028301. URL <https://link.aps.org/doi/10.1103/PhysRevLett.94.028301>.
- F. Irgens. *Continuum Mechanics*. Springer Berlin Heidelberg, Berlin, Heidelberg, 2008. ISBN 9783540742975.

- 
- F. Irgens. *Rheology and Non-Newtonian Fluids*. Springer International Publishing, Cham, 2014 edition, 2014. ISBN 9783319010526.
- N. M. James, E. Han, R. A. L. de la Cruz, J. Jureller, and H. M. Jaeger. Interparticle hydrogen bonding can elicit shear jamming in dense suspensions. *Nature materials*, 17(11):965–970, 2018. ISSN 1476-4660.
- N. M. James, H. Xue, M. Goyal, and H. M. Jaeger. Controlling shear jamming in dense suspensions via the particle aspect ratio. *Soft Matter*, 15:3649–3654, 2019. doi: 10.1039/C9SM00335E. URL <http://dx.doi.org/10.1039/C9SM00335E>.
- J. J. S. Jerome, N. Vandenberghe, and Y. Forterre. Unifying impacts in granular matter from quicksand to cornstarch. *Phys. Rev. Lett.*, 117:098003, Aug 2016. doi: 10.1103/PhysRevLett.117.098003. URL <https://link.aps.org/doi/10.1103/PhysRevLett.117.098003>.
- T. Kawasaki and L. Berthier. Discontinuous shear thickening in brownian suspensions. *Phys. Rev. E*, 98:012609, Jul 2018. doi: 10.1103/PhysRevE.98.012609. URL <https://link.aps.org/doi/10.1103/PhysRevE.98.012609>.
- I. M. Krieger and T. J. Dougherty. A mechanism for non-newtonian flow in suspensions of rigid spheres. *Transactions of the Society of Rheology*, 3(1):137–152, 1959. doi: 10.1122/1.548848. URL <https://doi.org/10.1122/1.548848>.
- A. A. Kumar, B. J. Medhi, and A. Singh. Experimental investigation of interface deformation in free surface flow of concentrated suspensions. *Physics of Fluids*, 28(11):113302, 2016. doi: 10.1063/1.4967739. URL <https://doi.org/10.1063/1.4967739>.
- D. Leighton and A. Acrivos. The shear-induced migration of particles in concentrated suspensions. *Journal of Fluid Mechanics*, 181:415–439, 1987. doi: 10.1017/S0022112087002155.
- E. Lerner, G. Düring, and M. Wyart. A unified framework for non-brownian suspension flows and soft amorphous solids. *Proceedings of the National Academy of Sciences*, 109(13):4798–4803, 2012. ISSN 0027-8424. doi: 10.1073/pnas.1120215109. URL <https://www.pnas.org/content/109/13/4798>.
- N. Y. C. Lin, B. M. Guy, M. Hermes, C. Ness, J. Sun, W. C. K. Poon, and I. Cohen. Hydrodynamic and contact contributions to continuous

- shear thickening in colloidal suspensions. *Phys. Rev. Lett.*, 115:228304, Nov 2015. doi: 10.1103/PhysRevLett.115.228304. URL <https://link.aps.org/doi/10.1103/PhysRevLett.115.228304>.
- A. J. Liu and S. R. Nagel. Jamming is not just cool any more. *Nature (London)*, 396(6706):21–22, 1998. ISSN 1476-4687.
- A. J. Liu and S. R. Nagel. The jamming transition and the marginally jammed solid. *Annual Review of Condensed Matter Physics*, 1(1):347–369, 2010. doi: 10.1146/annurev-conmatphys-070909-104045. URL <https://doi.org/10.1146/annurev-conmatphys-070909-104045>.
- T. Loimer, A. Nir, and R. Semiat. Shear-induced corrugation of free interfaces in concentrated suspensions. *Journal of Non-Newtonian Fluid Mechanics*, 102(2):115–134, 2002. ISSN 0377-0257. doi: [https://doi.org/10.1016/S0377-0257\(01\)00173-2](https://doi.org/10.1016/S0377-0257(01)00173-2). URL <https://www.sciencedirect.com/science/article/pii/S0377025701001732>.
- D. Lootens, H. van Damme, Y. Hémar, and P. Hébraud. Dilatant flow of concentrated suspensions of rough particles. *Phys. Rev. Lett.*, 95:268302, Dec 2005. doi: 10.1103/PhysRevLett.95.268302. URL <https://link.aps.org/doi/10.1103/PhysRevLett.95.268302>.
- R. Maharjan and E. Brown. Giant deviation of a relaxation time from generalized newtonian theory in discontinuous shear thickening suspensions. *Phys. Rev. Fluids*, 2:123301, Dec 2017. doi: 10.1103/PhysRevFluids.2.123301. URL <https://link.aps.org/doi/10.1103/PhysRevFluids.2.123301>.
- R. Maharjan, E. O’Reilly, T. Postiglione, N. Klimenko, and E. Brown. Relation between dilation and stress fluctuations in discontinuous shear thickening suspensions. *Phys. Rev. E*, 103:012603, Jan 2021. doi: 10.1103/PhysRevE.103.012603. URL <https://link.aps.org/doi/10.1103/PhysRevE.103.012603>.
- T. S. Majmudar and R. P. Behringer. Contact force measurements and stress-induced anisotropy in granular materials. *Nature*, 435, 2005. doi: 10.1038/nature03805. URL <https://doi.org/10.1038/nature03805>.
- S. Majmudar, I. R. Peters, E. Han, and H. M. Jaeger. Dynamic shear jamming in dense granular suspensions under extension. *Phys. Rev. E*, 95:012603, Jan 2017. doi: 10.1103/PhysRevE.95.012603. URL <https://link.aps.org/doi/10.1103/PhysRevE.95.012603>.

- 
- B. J. Maranzano and N. J. Wagner. The effects of particle size on reversible shear thickening of concentrated colloidal dispersions. *The Journal of Chemical Physics*, 114(23):10514–10527, 2001. doi: 10.1063/1.1373687. URL <https://doi.org/10.1063/1.1373687>.
- B. J. Maranzano and N. J. Wagner. Flow-small angle neutron scattering measurements of colloidal dispersion microstructure evolution through the shear thickening transition. *The Journal of Chemical Physics*, 117(22):10291–10302, 2002. doi: 10.1063/1.1519253. URL <https://doi.org/10.1063/1.1519253>.
- R. Mari, R. Seto, J. F. Morris, and M. M. Denn. Shear thickening, frictionless and frictional rheologies in non-brownian suspensions. *Journal of Rheology*, 58(6):1693–1724, 2014. doi: 10.1122/1.4890747. URL <https://doi.org/10.1122/1.4890747>.
- R. Mari, R. Seto, J. F. Morris, and M. M. Denn. Nonmonotonic flow curves of shear thickening suspensions. *Phys. Rev. E*, 91:052302, May 2015a. doi: 10.1103/PhysRevE.91.052302. URL <https://link.aps.org/doi/10.1103/PhysRevE.91.052302>.
- R. Mari, R. Seto, J. F. Morris, and M. M. Denn. Discontinuous shear thickening in brownian suspensions by dynamic simulation. *Proceedings of the National Academy of Sciences*, 112(50):15326–15330, 2015b. ISSN 0027-8424. doi: 10.1073/pnas.1515477112. URL <https://www.pnas.org/content/112/50/15326>.
- S. H. Maron and P. E. Pierce. Application of ree-eyring generalized flow theory to suspensions of spherical particles. *Journal of Colloid Science*, 11(1):80–95, 1956. ISSN 0095-8522. doi: [https://doi.org/10.1016/0095-8522\(56\)90023-X](https://doi.org/10.1016/0095-8522(56)90023-X). URL <https://www.sciencedirect.com/science/article/pii/009585225690023X>.
- C. I. Mendoza and I. Santamaría-Holek. The rheology of hard sphere suspensions at arbitrary volume fractions: An improved differential viscosity model. *The Journal of chemical physics*, 130(4):044904–044904–7, 2009. ISSN 0021-9606.
- F. S. Merkt, R. D. Deegan, D. I. Goldman, E. C. Rericha, and H. L. Swinney. Persistent holes in a fluid. *Phys. Rev. Lett.*, 92:184501, May 2004. doi: 10.1103/PhysRevLett.92.184501. URL <https://link.aps.org/doi/10.1103/PhysRevLett.92.184501>.



- A. B. Metzner and M. Whitlock. Flow behavior of concentrated (dilatant) suspensions. *Transactions of the Society of Rheology*, 2(1):239–254, 1958. doi: 10.1122/1.548831. URL <https://doi.org/10.1122/1.548831>.
- J. Mewis and N. J. Wagner. *Colloidal suspension rheology*. Cambridge series in chemical engineering. Cambridge University Press, Cambridge, 2012. ISBN 9781107622807.
- J. F. Morris. Lubricated-to-frictional shear thickening scenario in dense suspensions. *Phys. Rev. Fluids*, 3:110508, Nov 2018. doi: 10.1103/PhysRevFluids.3.110508. URL <https://link.aps.org/doi/10.1103/PhysRevFluids.3.110508>.
- S. Nemat-Nasser. *Plasticity : a treatise on finite deformation of heterogeneous inelastic materials*. Cambridge monographs on mechanics. Cambridge University Press, Cambridge, 2004. ISBN 0521839793.
- C. S. O’Hern, L. E. Silbert, A. J. Liu, and S. R. Nagel. Jamming at zero temperature and zero applied stress: The epitome of disorder. *Phys. Rev. E*, 68:011306, Jul 2003. doi: 10.1103/PhysRevE.68.011306. URL <https://link.aps.org/doi/10.1103/PhysRevE.68.011306>.
- Z. Pan, H. de Cagny, B. Weber, and D. Bonn. S-shaped flow curves of shear thickening suspensions: Direct observation of frictional rheology. *Phys. Rev. E*, 92:032202, Sep 2015. doi: 10.1103/PhysRevE.92.032202. URL <https://link.aps.org/doi/10.1103/PhysRevE.92.032202>.
- F. Parsi and F. Gadala-Maria. Fore-and-aft asymmetry in a concentrated suspension of solid spheres. *Journal of Rheology*, 31(8):725–732, 1987. doi: 10.1122/1.549944. URL <https://doi.org/10.1122/1.549944>.
- I. R. Peters and H. M. Jaeger. Quasi-2d dynamic jamming in cornstarch suspensions: visualization and force measurements. *Soft Matter*, 10:6564–6570, 2014. doi: 10.1039/C4SM00864B. URL <http://dx.doi.org/10.1039/C4SM00864B>.
- I. R. Peters, J. M. Amundson, R. Cassotto, M. Fahnestock, K. N. Darnell, M. Truffer, and W. W. Zhang. Dynamic jamming of iceberg-choked fjords. *Geophysical Research Letters*, 42(4):1122–1129, 2015. doi: <https://doi.org/10.1002/2014GL062715>. URL <https://agupubs.onlinelibrary.wiley.com/doi/abs/10.1002/2014GL062715>.

- I. R. Peters, S. Majumdar, and H. M. Jaeger. Direct observation of dynamic shear jamming in dense suspensions. *Nature*, 532(7598):214–217, 2016. ISSN 00280836. URL <http://search.proquest.com/docview/1781536995/>.
- D. Quemada. Rheology of concentrated disperse systems and minimum energy dissipation principle - i. viscosity-concentration relationship. *Rheologica acta*, 16(1):82–94, 1977. ISSN 0035-4511.
- M. Raffel, C. Willert, F. Scarano, C. Kähler, S. Wereley, and J. Kompenhans. *Particle Image Velocimetry : A Practical Guide*. Springer International Publishing : Imprint: Springer, Cham, 3rd ed. 2018. edition, 2018. ISBN 3-319-68852-9.
- D. W. A. Rees. *Basic engineering plasticity : an introduction with engineering and manufacturing applications*. Elsevier/Butterworth-Heinemann, Boston, MA, 1st ed. edition, 2006. ISBN 1-280-96446-4.
- J. Ren, J. A. Dijksman, and R. P. Behringer. Reynolds pressure and relaxation in a sheared granular system. *Phys. Rev. Lett.*, 110:018302, Jan 2013. doi: 10.1103/PhysRevLett.110.018302. URL <https://link.aps.org/doi/10.1103/PhysRevLett.110.018302>.
- O. Reynolds. Lvii. on the dilatancy of media composed of rigid particles in contact. with experimental illustrations. *The London, Edinburgh, and Dublin Philosophical Magazine and Journal of Science*, 20(127):469–481, 1885. doi: 10.1080/14786448508627791. URL <https://doi.org/10.1080/14786448508627791>.
- J. Richardson and W. Zaki. Sedimentation and fluidisation: part 1. *Chemical Engineering Research & Design*, 75:S82–S99, 1997. ISSN 0263-8762.
- M. Roché, E. Myftiu, M. C. Johnston, P. Kim, and H. A. Stone. Dynamic fracture of nonglassy suspensions. *Phys. Rev. Lett.*, 110:148304, Apr 2013. doi: 10.1103/PhysRevLett.110.148304. URL <https://link.aps.org/doi/10.1103/PhysRevLett.110.148304>.
- J. R. Royer, D. L. Blair, and S. D. Hudson. Rheological signature of frictional interactions in shear thickening suspensions. *Phys. Rev. Lett.*, 116:188301, May 2016. doi: 10.1103/PhysRevLett.116.188301. URL <https://link.aps.org/doi/10.1103/PhysRevLett.116.188301>.
- B. Saint-Michel, T. Gibaud, and S. Manneville. Uncovering instabilities in the spatiotemporal dynamics of a shear-thickening cornstarch suspension.

- Phys. Rev. X*, 8:031006, Jul 2018. doi: 10.1103/PhysRevX.8.031006. URL <https://link.aps.org/doi/10.1103/PhysRevX.8.031006>.
- S. Sarkar, D. Bi, J. Zhang, J. Ren, R. P. Behringer, and B. Chakraborty. Shear-induced rigidity of frictional particles: Analysis of emergent order in stress space. *Phys. Rev. E*, 93:042901, Apr 2016. doi: 10.1103/PhysRevE.93.042901. URL <https://link.aps.org/doi/10.1103/PhysRevE.93.042901>.
- R. Seto, R. Mari, J. F. Morris, and M. M. Denn. Discontinuous shear thickening of frictional hard-sphere suspensions. *Phys. Rev. Lett.*, 111:218301, Nov 2013. doi: 10.1103/PhysRevLett.111.218301. URL <https://link.aps.org/doi/10.1103/PhysRevLett.111.218301>.
- S. S. Shenoy and N. J. Wagner. Influence of medium viscosity and adsorbed polymer on the reversible shear thickening transition in concentrated colloidal dispersions. *Rheologica acta*, 44(4):360–371, 2005. ISSN 0035-4511.
- H. M. Shewan and J. R. Stokes. Analytically predicting the viscosity of hard sphere suspensions from the particle size distribution. *Journal of Non-Newtonian Fluid Mechanics*, 222:72–81, 2015. ISSN 0377-0257. doi: <https://doi.org/10.1016/j.jnnfm.2014.09.002>. URL <https://www.sciencedirect.com/science/article/pii/S0377025714001463>. Rheometry (and General Rheology): Festschrift dedicated to Professor K Walters FRS on the occasion of his 80th birthday.
- A. Singh, A. Nir, and R. Semiat. Free-surface flow of concentrated suspensions. *International Journal of Multiphase Flow*, 32(7):775–790, 2006. ISSN 0301-9322. doi: <https://doi.org/10.1016/j.ijmultiphaseflow.2006.02.018>. URL <https://www.sciencedirect.com/science/article/pii/S0301932206000486>.
- A. Singh, C. Ness, R. Seto, J. J. de Pablo, and H. M. Jaeger. Shear thickening and jamming of dense suspensions: The “roll” of friction. *Phys. Rev. Lett.*, 124:248005, Jun 2020. doi: 10.1103/PhysRevLett.124.248005. URL <https://link.aps.org/doi/10.1103/PhysRevLett.124.248005>.
- V. Sivadasan. *Microstructure Dynamics in Shear Thickening Suspensions*. Universiteit van Amsterdam, 2020. ISBN 9789402818611.
- M. Smith, R. Besseling, M. Cates, and V. Bertola. Dilatancy in the flow and fracture of stretched colloidal suspensions. *Nature communications*, 1(1):114–114, 2010. ISSN 2041-1723.

- J. J. Stickel and R. L. Powell. Fluid mechanics and rheology of dense suspensions. *Annual Review of Fluid Mechanics*, 37(1):129–149, 2005. doi: 10.1146/annurev.fluid.36.050802.122132. URL <https://doi.org/10.1146/annurev.fluid.36.050802.122132>.
- B. D. Timberlake and J. F. Morris. Particle migration and free-surface topography in inclined plane flow of a suspension. *Journal of Fluid Mechanics*, 538:309–341, 2005. doi: 10.1017/S0022112005005471.
- V. Vitelli and M. van Hecke. Soft materials: Marginal matters. *Nature (London)*, 480(7377):325, 2011. ISSN 1476-4687.
- N. J. Wagner and J. F. Brady. Shear thickening in colloidal dispersions. *Physics Today*, 62(10):27–32, 2009. doi: 10.1063/1.3248476. URL <https://doi.org/10.1063/1.3248476>.
- S. R. Waitukaitis. *Impact-Activated Solidification of Cornstarch and Water Suspensions*. Springer Theses, Recognizing Outstanding Ph.D. Research. Springer International Publishing : Imprint: Springer, Cham, 1st ed. 2015. edition, 2015. ISBN 3-319-09183-2.
- S. R. Waitukaitis and H. M. Jaeger. Impact-activated solidification of dense suspensions via dynamic jamming fronts. *Nature*, 487(7406):205, 2012. ISSN 0028-0836. doi: 10.1038/nature11187.
- S. R. Waitukaitis, L. K. Roth, V. Vitelli, and H. M. Jaeger. Dynamic jamming fronts. *EPL (Europhysics Letters)*, 102(4):44001, may 2013. doi: 10.1209/0295-5075/102/44001.
- D. Wang, J. Ren, J. A. Dijksman, H. Zheng, and R. P. Behringer. Microscopic origins of shear jamming for 2d frictional grains. *Phys. Rev. Lett.*, 120:208004, May 2018. doi: 10.1103/PhysRevLett.120.208004. URL <https://link.aps.org/doi/10.1103/PhysRevLett.120.208004>.
- M. Wyart and M. E. Cates. Discontinuous shear thickening without inertia in dense non-brownian suspensions. *Phys. Rev. Lett.*, 112:098302, Mar 2014. doi: 10.1103/PhysRevLett.112.098302. URL <https://link.aps.org/doi/10.1103/PhysRevLett.112.098302>.
- H. Xiao, O. T. Bruhns, and A. Meyers. Logarithmic strain, logarithmic spin and logarithmic rate. *Acta mechanica*, 124(1):89–105, 1997. ISSN 0001-5970.

- A. A. Zadeh, J. Barés, T. A. Brzinski, K. E. Daniels, J. Dijksman, N. Docquier, H. O. Everitt, J. E. Kollmer, O. Lantsoght, D. Wang, M. Workamp, Y. Zhao, and H. Zheng. Enlightening force chains: a review of photoelasticity in granular matter. *Granular matter*, 21(4):1–12, 2019. ISSN 1434-5021.
- I. E. Zarraga, D. A. Hill, and D. T. Leighton. The characterization of the total stress of concentrated suspensions of noncolloidal spheres in newtonian fluids. *Journal of Rheology*, 44(2):185–220, 2000. doi: 10.1122/1.551083. URL <https://doi.org/10.1122/1.551083>.
- J. Zhang, T. S. Majmudar, A. Tordesillas, and R. P. Behringer. Statistical properties of a 2d granular material subjected to cyclic shear. *Granular matter*, 12(2):159–172, 2010. ISSN 1434-5021.

Article I

---

**Getting jammed in all directions:  
Dynamic shear jamming around a  
cylinder towed through a dense  
suspension**

---

Olav Rømcke, Ivo R. Peters, R. Jason Hearst

*Published*  
*Physical Review Fluids*, **6**, 063301.



## Getting jammed in all directions: Dynamic shear jamming around a cylinder towed through a dense suspension

Olav Rømcke <sup>1</sup>, Ivo R. Peters <sup>2</sup>, and R. Jason Hearst <sup>1,\*</sup>

<sup>1</sup>*Norwegian University of Science and Technology, Department of Energy and Process Engineering, NO-7491 Trondheim, Norway*

<sup>2</sup>*University of Southampton, Faculty of Engineering and Physical Sciences, Highfield, Southampton SO17 1BJ, England, United Kingdom*



(Received 31 March 2020; accepted 17 May 2021; published 7 June 2021)

Experimental results of towing a cylinder through a dense suspension of cornstarch and sucrose-water are presented. Focus is placed on the jamming fronts that exist in such systems. The literature has concentrated on the propagation of the jammed region under pushing, pulling, or shearing conditions independently. How the different fronts interact and if the fronts are symmetric when generated simultaneously has remained unexplored. Investigating this is our main goal. With the current setup, we are able to view a continuous, quasi-two-dimensional field around the cylinder. As such, a way of generating jamming fronts is presented whereby pushing, pulling, and shearing can be examined simultaneously. In agreement with previous studies, the front propagates roughly twice as fast in the longitudinal direction compared to the transverse direction, which is attributed to a single underlying onset strain, regardless of orientation from the cylinder. Although the jamming front shows nearly perfect transverse symmetry, there is clear longitudinal asymmetry. This is evident in the velocity and strain fields, and is also detectable in the front propagation velocity and onset strain.

DOI: [10.1103/PhysRevFluids.6.063301](https://doi.org/10.1103/PhysRevFluids.6.063301)

### I. INTRODUCTION

The transient development of a dynamically jammed region has been investigated extensively in experiments where the applied stress has been in the form of pulling [1], pushing [2–5], or shearing [6–8]. In these works, the different cases have been addressed separately, but how these three scenarios interact in a single system has remained unexplored. By dragging a cylinder through a suspension of cornstarch and sucrose-water, we present a way of producing dynamic jamming fronts where the system will have coexisting regions that experience pulling, pushing, and shearing simultaneously in an observable fashion.

A granular suspension, consisting of solid particles suspended in a liquid, can exhibit both fluidlike and solidlike behavior. The observed behavior depends primarily on the volume fraction and the applied stress, but is also influenced by factors such as the deformation history [4,7,9–14], particle surface chemistry [15], confinement effects [16–18], and the shape of the particles [19,20]. Above a critical volume fraction and at low stress, a granular suspension will be in a jammed state, identified by a finite yield stress [21]. Jamming will occur at lower volume fractions under shear deformation when frictional contact between particles is present [11]. Some suspension systems, such as cornstarch-water mixtures, can switch between frictional and frictionless states depending on the applied stress. This results in the ability to flow at low stress, but a dynamic transition into

---

\*jason.hearst@ntnu.no



a jammed state at high stress, when the volume fraction is below, but close to, the critical volume fraction.

The assumption of smooth, force-free particles falls short of adequately describing this flow behavior. This is particularly true for dense suspensions where particle-particle interactions may dominate the internal force structure of the suspension. With regards to cornstarch suspensions, it has been identified that friction [22–26] and repulsive forces between particles [15,17,27] play key roles when it comes to describing the extreme shear thickening that is typically observed. The steady state behavior of such systems has been studied in both experiments [7,19,28–30] and simulations [22,31–37]. The consensus appears to be that the observed thickening and jamming is the development of a frictional contact network between grains as the amount of applied stress increases.

When a low stress is applied, the particles are not able to overcome the repulsive force, and the lubrication layer ensures that the suspension flows as if the particles were frictionless. Above a critical stress the particles come into frictional contact, resulting in an increase in resistance to flow. It is worth mentioning that potential hydrodynamic mechanisms have been proposed that do not require frictional contacts [38]. A framework for characterizing the flow of noninertial, non-Brownian, dense suspensions has been presented by Wyart and Cates [39]. Examples of the use of this model can be seen in both experimental [7,28,29] and numerical [22,31,36,37] studies. This model describes how continuous shear thickening, discontinuous shear thickening, and dynamic jamming are the results of a transition from lubricated (frictionless) interactions to frictional contacts between particles.

To explain the transient response of such systems, a few more concepts need to be introduced. How does the suspension transition from a liquidlike to a solidlike state, and how does this macroscopically propagate through the suspension? This leads us to the concept of dynamic jamming fronts, first introduced by Waitukaitis *et al.* [40]. This sparked the study of dynamic jamming fronts [1–4,6,7]. The previously mentioned works indicate the existence of an onset strain [4,7]. In dry granular systems, this is often presented as the material needing some deformation in order to build up a sufficient number of strong contacts between grains, that in turn increases the resistance to further deformation [9–12]. Large amplitude oscillatory shear experiments with cornstarch suspensions [13,14] further strengthen the evidence for an onset strain being an important parameter for the transient onset of dynamic jamming. The onset strain, which depends on how densely packed the suspension is, sets the ratio between the velocity of the jamming front and the perturbing body [2–4,6,7]. An onset strain can also be used to explain why the jamming front propagates with different speeds relative to the direction of the perturbation [4].

The study of jamming fronts has up to this point been viewed in systems where the perturbation is singularly in the form of pulling, pushing, or shearing. How the jamming front propagates around a towed body that experiences all three of these simultaneously remains unexplored. Here, we investigate the shape and the speed of the jamming front around a towed cylinder. As indicated by the literature, we link the observed behavior to an onset strain that accompanies the jamming front.

## II. EXPERIMENT

The purpose of the experimental setup is to be able to generate, visualize, and measure jamming fronts around a moving body. In this paper we present observations of how the jammed region propagates when a cylinder is towed through a suspension of cornstarch and sucrose-water solution. We begin with a description of the suspension itself in Sec. II A, followed by rheological measurements in Sec. II B in order to identify a composition capable of dynamically jamming. This is followed by a description of the setup in Sec. II C and how the measurements were conducted in Sec. II D.

### A. Suspension

The suspension used in the present paper is a mixture of cornstarch (*maizena maisstivelse*) and sucrose-water. An important parameter for characterizing the suspension is its volume fraction ( $\phi$ ) defined as the fraction of the volume occupied by a solid; in Sec. II B, we will show that it is only in a specific range of packing fractions where dynamic jamming occurs. It is important to have a suspension that does not change characteristics over the course of an experiment. Particle settling is one such effect that is typically addressed by density matching the fluid phase to the solid phase [28,30]. Depending on the nature of the experiment, perfect density matching might not be necessary [3,15,16,29]. In order to increase settling time, we use a  $50.0 \pm 0.3\%$  by weight sucrose-water solution as the liquid phase with a density of  $\rho_l = 1230 \text{ kg/m}^3$  and viscosity of  $\eta_0 = 16 \text{ mPa s}$ . Using this composition, we estimate settling to have a negligible effect over the time span of one experiment [41,42]. A cornstarch particle is porous [43], so when mixing a sample some time is needed for the starch to soak in the liquid. After a sample was homogeneously mixed, it was soaked and intermittently mixed for 1 h.

With regard to the rheometer measurements, we expect the suspension at rest to settle roughly  $6 \mu\text{m}$  in 1 min for the highest volume fraction ( $\phi = 0.362$ ). As an up or down stress ramp takes 50 s, we do not expect to observe any consequence of settling at this time scale. For a dilute suspension, drift due to settling is higher. At the lowest volume fraction ( $\phi = 0.05$ ), we estimate  $130 \mu\text{m}$  in 1 min. However, for the rheometer data presented here, no significant drift in the data was observed during the course of one experiment.

### B. Rheology

Dense cornstarch suspensions are typically characterized as noninertial, non-Brownian, frictional suspensions, and their rheological properties have been extensively investigated [13–17,28–30]. The aim of this section is to verify that our suspension is able to dynamically jam and identify in what range of volume fractions ( $\phi$ ) this will occur.

By using the framework from Wyart and Cates [39] it is possible to identify the frictionless and frictional jamming volume fractions. In this model, the predicted viscosity is given by

$$\eta \equiv \frac{\Sigma}{\dot{\gamma}} = \eta_0 \left( 1 - \frac{\phi}{\phi_{\text{eff}}} \right)^{-2}, \quad (1)$$

where

$$\phi_{\text{eff}} = f(\Sigma)\phi_m + [1 - f(\Sigma)]\phi_0 \quad (2)$$

and

$$f(\Sigma) = 1 - e^{-\Sigma/\Sigma^*}, \quad (3)$$

where  $\Sigma$  is shear stress,  $\eta$  is viscosity, and  $\phi_{\text{eff}}$  is the effective volume fraction at which viscosity diverges. The shear stress is assumed to be proportional to pressure  $\Sigma = \mu P$ , where  $\mu$  is the effective friction coefficient. As a consequence, Eqs. (1)–(3) can be written in terms of  $\Sigma$  instead of  $P$  [7]. For a detailed discussion, the reader is referred to the original paper [39], or examples of how this theory has been applied and tested [7,29,31,36]. What is important here is that in the limits of low stress ( $\Sigma \rightarrow 0$ ) and high stress ( $\Sigma \rightarrow \infty$ ) the viscosity is quasi-Newtonian, diverging at  $\phi = \phi_0$  and  $\phi = \phi_m$ , respectively [39]. In other words, when low stress is applied, the viscosity tends to infinity when approaching  $\phi = \phi_0$ . If a high stress is applied, the viscosity tends to infinity when approaching  $\phi = \phi_m$ . Evaluating (1) at the low and high stress limits results in

$$\lim_{\Sigma \rightarrow 0} \eta = \eta_0 \left( 1 - \frac{\phi}{\phi_0} \right)^{-2} \quad (4)$$

TABLE I. Physical parameters for the suspension of cornstarch and sucrose-water solution.

Parameter	Value	Uncertainty	Unit
$\rho_l$	1230	10	$\text{kg m}^{-3}$
$\rho_w$	995	10	$\text{kg m}^{-3}$
$\rho_s$	1630	20	$\text{kg m}^{-3}$
$\beta$	11.2	0.2	%
$\eta_0$	0.016	0.001	Pa s

and

$$\lim_{\Sigma \rightarrow \infty} \eta = \eta_0 \left(1 - \frac{\phi}{\phi_m}\right)^{-2}. \quad (5)$$

Following the method of Han *et al.* [7], the two critical volume fractions ( $\phi_m$  and  $\phi_0$ ) are determined by fitting these functions to the measured viscosities in their respective regimes. Most importantly, the range these two volume fractions span is the range of volume fractions where the suspension is able to dynamically jam. The characteristic stress ( $\Sigma^*$ ) controls the stress at which the transition between the two regimes occurs [7,27,39], which we find by curve fitting our data to the Wyart and Cates model described above. As the Wyart and Cates model has singularities at  $\phi \geq \phi_m$  for sufficiently high stress, some care needs to be taken in order to fit the data. Here we restrict ourselves to the data points used to find  $\phi_m$  and  $\phi_0$ , similar to the method used by [44], resulting in  $\Sigma^* = 10.2$  Pa.

An AR-G2 rheometer from TA-Instruments with a rotating parallel plate geometry with a radius of  $r = 20$  mm was used. Cornstarch granules have been reported to have a diameter of about  $d_p = 15 \mu\text{m}$  [1,7,29]. A gap size larger than  $h = 0.7$  mm was used in order to ensure that a sufficient number of particles occupy the space between the plates. The volume fraction for each sample is calculated as

$$\phi = \frac{(1 - \beta)m_s/\rho_s}{(1 - \beta)m_s/\rho_s + m_l/\rho_l + \beta m_s/\rho_w}, \quad (6)$$

where  $\beta$  is water content,  $m_s$  is the starch mass,  $\rho_s$  is the starch density,  $m_l$  is the liquid mass,  $\rho_l$  is the liquid density, and  $\rho_w$  is the density of water. The values of these parameters are listed in Table I. Note that Eq. (6) does not account for porosity. This can be adjusted for by multiplying  $\phi$  with  $1/(1 - \xi)$ , where  $\xi$  represents porosity.  $\xi$  is expected to have a value of about 0.3 in our setup [43]. Correcting for this would not change our conclusion. For every volume fraction, a sample was prepared according to Eq. (6), which typically resulted in a measurement uncertainty in  $\phi$  of  $\pm 0.005$ . The sample was presheared at the maximum stress for 60 s. Viscosity measurements were stress controlled, which was done by ramping up and down three times over roughly 50 s (dense regime) up to 400 s (diluted regime) for one ramp. Depending on the volume fraction, the stress ranged from 0.04 Pa to a maximum of 100 Pa (high  $\phi$ ), 400 Pa (medium  $\phi$ ), or 40 Pa (low  $\phi$ ). The duration and ramp range were tuned to minimize surface deformations and drift.

Finally, there are some limitations that restrict our measurement window. The rheometer itself can measure rotational speed up to 300 rad/s with a resolution of  $10^{-9}$  rad/s, and a maximum torque of 0.2 Nm with a resolution of  $10^{-9}$  N m. This puts direct restrictions on stress and strain rate. In order to ensure non-Brownian and noninertial conditions,  $\text{Pe} = \eta_0 d_p^3 \dot{\gamma} / \kappa \theta \gg 1$  and  $\text{St} = \rho_s d_p^2 \dot{\gamma} / \eta_0 \ll 1$ , respectively. Here,  $\kappa$  represents Boltzmann's constant and  $\theta$  is absolute temperature, kept at 20 °C for the entire experiment. The constraints in Peclet (Pe) and Stokes (St) number put additional restrictions on our measurement window. In addition, the surface tension should be sufficiently strong to hold the individual particles contained between the parallel plates. Here, we have used the semiempirical relation  $\Sigma_{\max} \approx 0.1\Gamma/d_p$  [7,16–18].  $\Gamma$  represents the surface

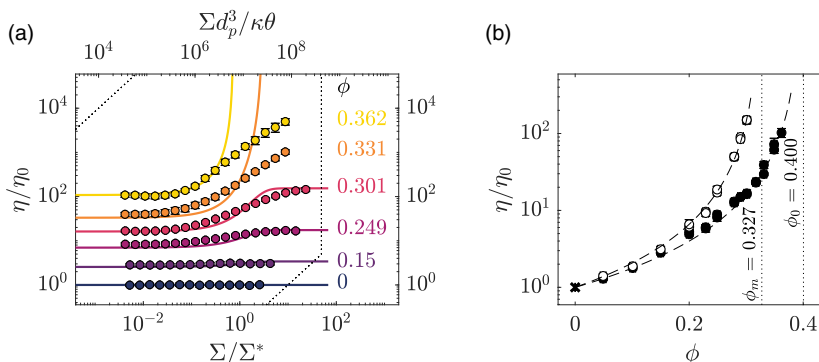


FIG. 1. Rheology of the sucrose-water-cornstarch suspensions. (a) Normalized viscosity as a function of applied stress. The volume fraction is indicated in the figure. The plotted lines are a result of a curve fit with the Wyart and Cates model described by Eqs. (1)–(3). We find  $\Sigma^*$  to be 10.2 Pa. (b) Normalized viscosity as a function of volume fraction in the frictionless low stress (filled) and frictional high stress (open) regimes. The dashed lines shows curve fits with Eqs. (4) and (5). Note that the two curves seems to diverge at different critical volume fractions  $\phi_0$  and  $\phi_m$ , respectively, represented by the dotted lines.

tension, which we set to  $75 \text{ mN m}^{-1}$  [45]. For our system, this results in a maximum of roughly 500 Pa. However, larger surface deformations were in some cases observed at lower stresses. These measurements were then discarded, and the maximum stress reduced. These restrictions reduced our measurement window, and are represented by the dotted lines in Fig. 1(a).

Figure 1(a) shows the viscosity response to applied stress for different volume fractions. Note the quasi-Newtonian regimes at high and low stress indicated by regions of constant viscosity for a change in applied stress. For  $\phi > 0.3$  we are not able to reach the high stress Newtonian regime. In Fig. 1(b) the viscosity at high and low stress has been plotted as a function of volume fraction. Note that at low stress the viscosity seems to diverge at a volume fraction of  $\phi_0 = 0.400$ , while at high stress the viscosity diverges at  $\phi_m = 0.327$ . If we consider a suspension with a volume fraction in-between these two values [vertical dashed lines in Fig. 1(b)], the suspension flows, and behaves as a fluid, if we apply low stress to the sample, but the viscosity tends to infinity as stress is increased. In this paper we choose a volume fraction of  $\phi = 0.36$ .

### C. Towed cylinder experimental configuration

A schematic of the experimental setup is given in Fig. 2(a). The cylinder is driven by a Bosch-Rexroth MKR 15-65 traverse. Two Photron FASTCAM Mini WX100s, each with a resolution of  $2048 \times 2048$  pixels, are used for capturing the movement of the suspension surface. One camera is placed in front of the cylinder, and one behind. The tank is  $360 \times 310$  mm, while the cylinder has a diameter of  $D = 30$  mm. The suspension phase is 30 mm thick, and floats on top of a 20 mm thick layer of high density fluorocarbon oil (Fluorinert, FC-74) which makes the system quasi two-dimensional (2D) [2]. By comparing force and momentum change, Peters and Jaeger [2] showed that systems like this are close to 2D. Here, we vary the cylinder depth, and do an experiment at half the suspension layer thickness to confirm that there is no change in behavior. The traverse drive is controlled through LABVIEW, and sends a trigger signal for the cameras whenever the traverse starts moving. We drive the cylinder at ten different velocities between 0.01 and 0.14 m/s. A frame rate is chosen such that the cylinder displacement between frames is roughly constant between cases. Black pepper serves as tracer particles for the particle image velocimetry (PIV) analysis [2,6,7]. The pepper particle diameter is roughly in the range 3 to 15 pixels. In postprocessing, the two resulting velocity fields are stitched together, making a continuous field around the cylinder.

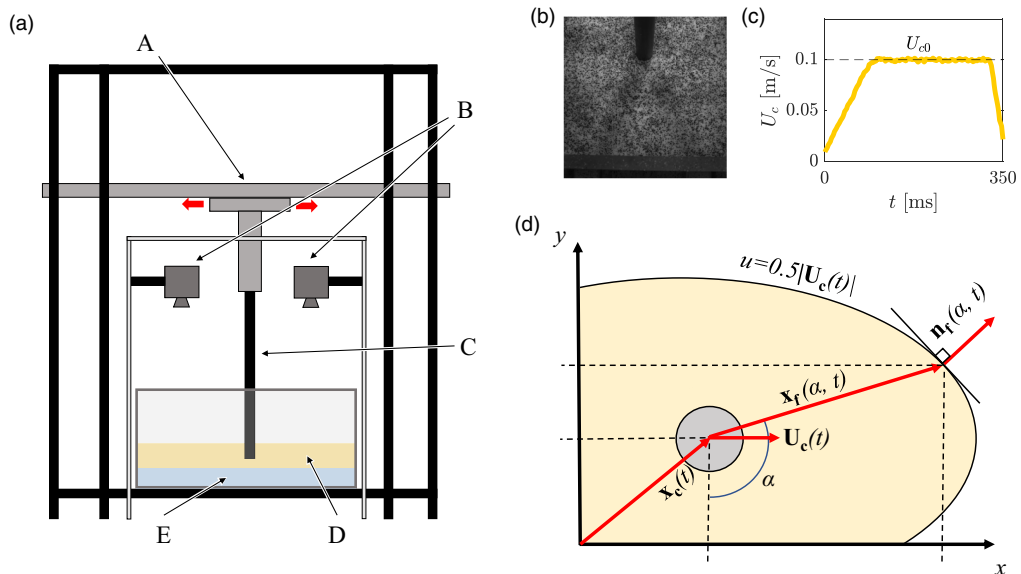


FIG. 2. (a) Schematic of the experimental setup with the traverse (A), cameras (B), cylinder (C), suspension (D), and Fluorinert (E). (b) Snapshot of the suspension surface. Black pepper is used as tracer particles for the particle image velocimetry. See Supplemental Material [46] for a sample movie of both camera views. (c) A time series of the cylinder velocity. Note that the traverse accelerates to constant velocity  $U_{c0}$ . (d) Schematic representation of the jamming front and variables where  $\mathbf{x}_c$ ,  $\mathbf{U}_c$ ,  $\mathbf{x}_f$ ,  $\mathbf{n}_f$ , and  $\alpha$  represent cylinder position, cylinder velocity, front position, front normal vector, and angle, respectively. The jamming front is identified as the velocity contour  $u = 0.5|\mathbf{U}_c(t)|$ .

The following procedure was adopted prior to the actual measurements for each test case. First, a batch of cornstarch and water-sucrose solution was prepared, as explained in Secs. II A and II B. The tank was then filled with Fluorinert, before the layer of suspension was poured on top. Finally, the cylinder was submerged 17 mm into the suspension, before black pepper was sprinkled on the suspension surface. The view from one of the cameras is provided in Fig. 2(b). In Fig. 2(b), there is an average of 10 to 11 pepper grains per  $48 \times 48$  pixel square window, which is typical. After the measurements were conducted, the suspension layer was removed, and a new batch of suspension was poured onto the Fluorinert and the experiment was repeated.

#### D. Measurement process

Measurements were conducted by traversing the cylinder back and forth. This triggers the cameras, which capture the movement of the suspension surface until the camera memory is full. A time series of the cylinder velocity can be seen in Fig. 2(c).

As mentioned, PIV was used to convert the resulting images into time-resolved velocity vector fields. In particular, LaVision Davis 8.4.0 was used. Three passes were done with square interrogation windows of  $96 \times 96$  pixels followed by two passes with circular interrogation windows with decreasing size for each pass, ending at  $48 \times 48$  pixels. This yielded one time series of the velocity field in front, and one behind the cylinder. Each set of frames was stitched together with a weighted average in the overlapping region. If the cylinder blocked one of the camera views, the weight was set to zero in that region. The result was a velocity field where the only area not visible is the location where the cylinder penetrates the suspension surface. Finally, the resulting velocity field was time filtered with a moving Hanning window of 35 frames. Note that whether the cylinder is moving

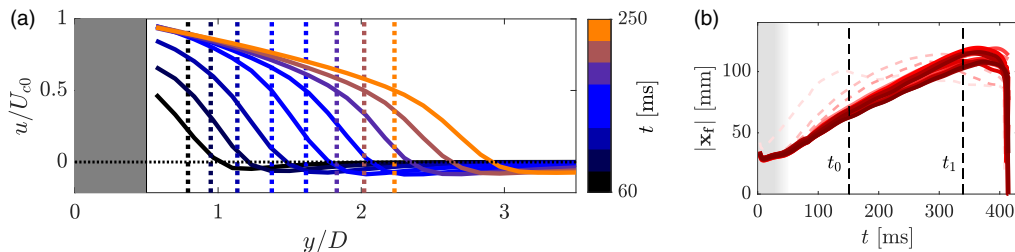


FIG. 3. The dynamic jamming front from two example experiments. (a) The velocity profiles at  $\alpha = 0$  and a cylinder velocity of  $U_{c0} = 0.14$  m/s. The black-blue-orange color scheme indicates time, and the gray region represents the cylinder. Dashed lines indicate the position of the jamming front with the corresponding color. Notice that the cylinder is accelerating for the first three profiles, but even though a constant cylinder speed is reached, the location of the front still propagates through the suspension. (b) The position of the jamming front at  $\alpha = \pi/2$  and at a cylinder velocity of  $U_{c0} = 0.08$  m/s. The pink to red color scheme indicates consecutive measurements. The vertical dashed lines indicate the range where the cylinder has a constant speed, and the front is propagating freely through the suspension. The gray shaded region near  $t = 0$  represents the region where uncertainty is significant, and thus the results therein are not treated as statistically significant; they are included in this figure only for completeness.

“back” or “forth” in the laboratory frame, the view is always rotated in postprocessing, such that the cylinder is moving in the positive  $x$  direction.

The position of the jamming front is defined as the location in the suspension that has half the velocity of the cylinder [1–4,6,7]. The first-order measures of the jamming front’s location and orientation are indicated in Fig. 2(d). Here,  $\mathbf{x}_c$ ,  $\mathbf{U}_c$ ,  $\mathbf{x}_f$ ,  $\mathbf{n}_f$ , and  $\alpha$  represent cylinder position, cylinder velocity, front position, front normal vector, and angle, respectively. It is worth noting some key aspects of these definitions. First, the front position ( $\mathbf{x}_f$ ) is always relative to the cylinder. Furthermore, the cylinder is moving in the positive  $x$  direction. Finally,  $\alpha = 0$  is orientated directly in the negative  $y$  direction. As an illustrative example, Fig. 3(a) shows the velocity profile of the suspension in the transverse cross section ( $\alpha = 0$ ). The jamming front location is indicated by the dashed vertical lines. The front propagation factor  $k_f$  will be studied in particular in Sec. III B, and is defined as the speed of the front scaled with the speed of the cylinder. A more detailed description and derivation of the front propagation based on these front measures is given in Appendix A.

Figure 3(b) shows multiple time series of the position of the jamming front in front of the cylinder. Note that from 0 to 150 ms the cylinder is accelerating, and the jamming front is starting to develop. After 350 ms, the front interacts with the boundary. The data used in the present analysis is identified by the region between the two dashed lines. In this region, the cylinder has a constant speed, and the front propagates through the suspension unimpeded. Note also that the first few runs show an earlier boundary interaction compared to the later runs. Through all cases, the first few runs differ from the later runs; the later runs are repeatable. Here, the analysis is done on the measurements in this repeatable regime, where the cylinder has a constant speed, and the front is propagating freely through the suspension. Both in dry granular materials [11] and dense frictional suspensions [7] shear history is important. By excluding the first few runs, we, in effect, only consider experiments with the same deformation history.

### III. RESULTS

As previously mentioned, jamming fronts have been studied independently under pulling, pushing, and shearing conditions [1–4,6,7]. The present setup allows for simultaneous observations of all three regimes. We begin by presenting the velocity field and the shape of the jamming front in Sec. III A. This is followed by a description of the front propagation ( $k_f$ ) and its relation to cylinder

velocity ( $U_{c0}$ ) and angle from the cylinder ( $\alpha$ ) in Sec. III B. To keep our variables in nondimensional form, we will present the cylinder velocity scaled as  $U_{c0}/U_c^* - 1$  henceforth. Here,  $U_c^*$  represents the velocity at which jamming fronts occur. At cylinder velocities lower than  $U_c^*$ , we cannot separate the front propagation factor ( $k_f$ ) from zero. How we quantify  $U_c^*$  is described in Sec. III B. We identify that there is an onset strain ( $\epsilon_c$ ) associated with the moving jamming front, not only in the longitudinal and transverse direction [4], but for all orientations about the cylinder. Furthermore, our setup makes it possible to directly compare the fore and aft half planes relative to the cylinder. We observe an asymmetry, which is also quantified.

### A. The velocity field and the jamming front

Figure 4(a) shows a time series of contours of the  $x$  component of the velocity field with velocity vectors superimposed. A region of near uniform velocity moves with the cylinder as it progresses through the suspension. This region of near uniform velocity grows over time, and is identified as the jammed region. The jammed region is separated from the unjammed region by the jamming front. The position of the jamming front ( $\mathbf{x}_f$ ) is defined as the points in the suspension where the velocity is half the velocity of the cylinder [1–4,6]. A more thorough description is given in Appendix A. Note that the jamming front itself is symmetric both in the transverse and longitudinal directions. However, in the unjammed region of the suspension, an asymmetry in longitudinal direction is observed. This can be seen by following the  $u/U_{c0} = 0$  contour.

Figures 4(b) and 4(c) represent the measures for strain rate  $\dot{\gamma}_s$  and accumulated strain  $\epsilon_s$ . In short, we use the norm of the respective tensors to represent the intensity. The tensor for strain rate is the strain rate tensor, while the tensor for accumulated strain is the Eulerian logarithmic strain tensor [47]. With regards to jamming fronts, earlier attempts at representing accumulated strain have typically been in the form of numerically integrating components of the strain rate tensor [1,4,7]. We choose to represent strain by the Eulerian logarithmic strain tensor, as it still is defined from the sum of increments, and represents deformation in the deformed configuration. The latter will be important, as we will compare the accumulated strain and the location of the jamming front. A description of how  $\dot{\gamma}_s$  and  $\epsilon_s$  are assessed can be found in Appendix B.

From Fig. 4(b) we see that a wave of high strain rate leads the way for the jamming front. As the wave passes through, it leaves behind a region of jammed material. The longitudinal asymmetry in the unjammed region mentioned earlier is also clear from this figure. At the jamming front in Fig. 4(c),  $\epsilon_s$  has an approximately constant value throughout the experiment. We have indicated this with a colorband. This is discussed further in later sections. The behavior described above is the case for  $U_{c0}/U_c^* - 1 \geq 2.2$ ; a wave of high strain rate travels in front of the jamming front. Similar behavior was observed by Peters and Jaeger [2]. This differs from dry granular study of jamming fronts, where the highest change in volume fraction almost perfectly aligns with the jamming front [40].

For lower  $U_{c0}$ , the jammed region is not as obvious. Figure 5 shows the velocity field for  $U_{c0}/U_c^* - 1 = 0.4$ . Relative to the cylinder displacement, the front does not propagate as fast through the suspension, and the close-to-uniform-velocity region is not as large as what we see in Fig. 4(a). Compared to the high velocity cases, we see a longitudinal symmetry in the unjammed region of the suspension.

From the velocity field shown in Fig. 4(a), we see that for the duration of an experiment the area enclosed by the jamming front increases. Figure 6 shows the self-similarity of the shape of the jamming front. Here, the jamming front has been scaled by  $|\mathbf{x}_f| = \frac{1}{2}(|\mathbf{x}_f|_{\alpha=\pi} + |\mathbf{x}_f|_{\alpha=0})$ . The shape of this region is approximately self-similar in the steady regime of the experiment. Note the anisotropic shape, where the longitudinal position of the front is close to a factor of 2 larger than the transverse position. Both the self-similarity and the longitudinal-transverse anisotropy of the shape are consistent with earlier observations [2,4].

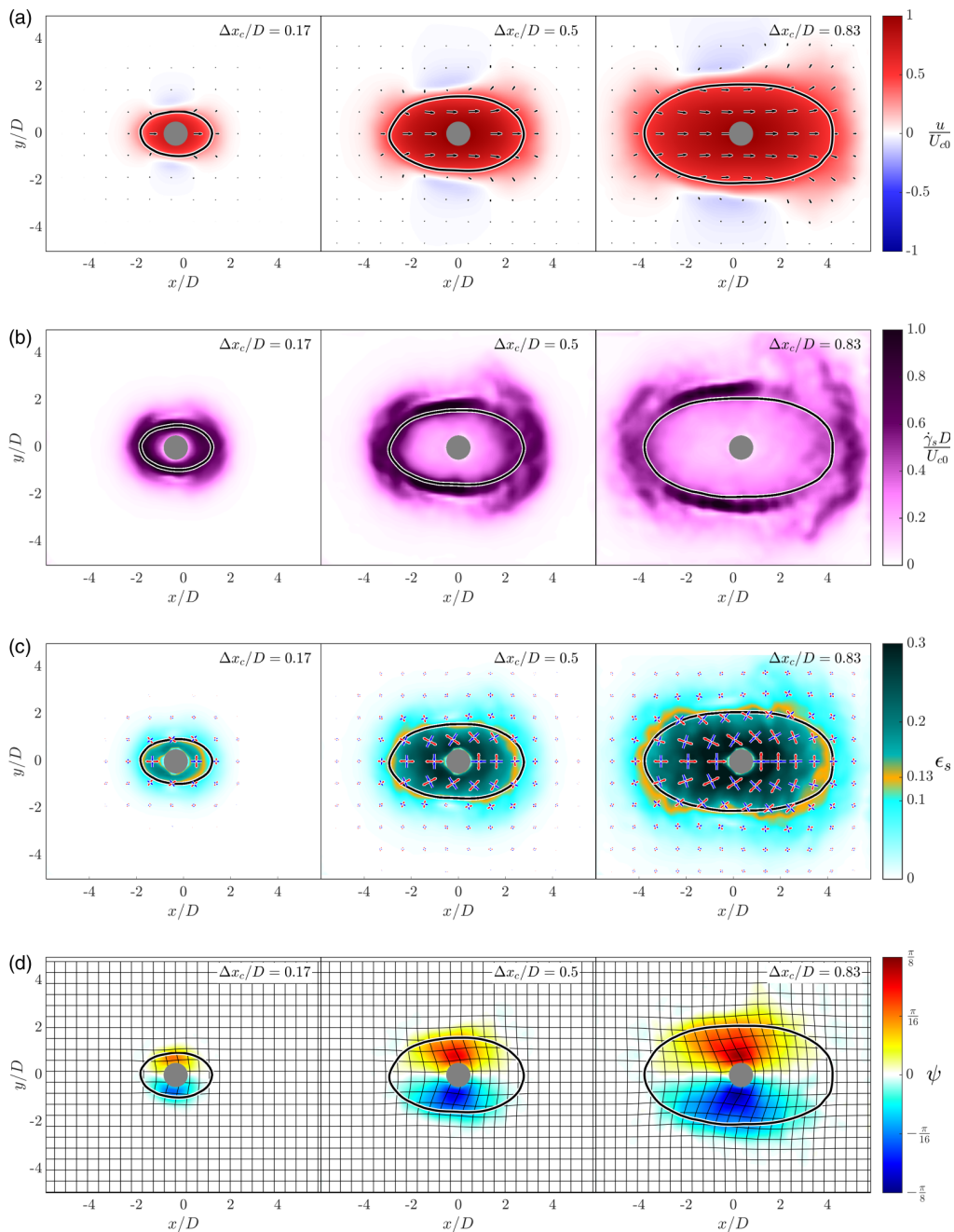


FIG. 4. Snapshots of (a) the  $x$  component of the velocity field with velocity vectors, (b) the deformation rate  $\dot{\gamma}_s$ , and (c) the accumulated strain  $\epsilon_s$ . The red arrows indicate direction of extension, while the blue arrows indicate the direction of compression. The length is scaled with  $\epsilon_s$  to indicate amount of deformation. In addition, (d) shows the rotation angle ( $\psi$ ) of the material. The grid represents the movement of the material points. In all figures, the black line represents the jamming front and the cylinder velocity is at  $U_{c0}/U_c^* - 1 = 5.4$ .  $\Delta x_c/D$  indicates the cylinder displacement normalized by the cylinder diameter. See Supplemental Material [46] for a sample movie of the four fields represented here.



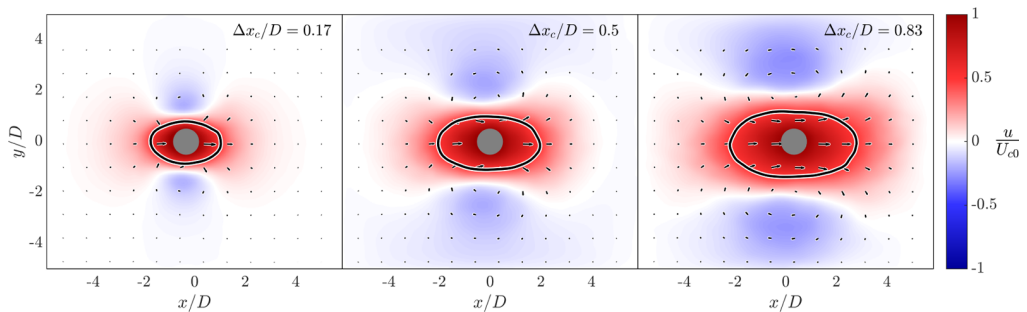


FIG. 5.  $x$  component of the velocity field at  $U_{c0}/U_c^* - 1 = 0.4$  with velocity vectors. The black line represents the jamming front.  $\Delta x_c/D$  indicates the cylinder displacement normalized by the cylinder diameter. See Supplemental Material [46] for a sample movie of the field represented here.

### B. Front propagation

The front,  $\mathbf{x}_f$ , propagates through the suspension with a certain speed. Note that the jamming front is not associated with any specific material point, but a velocity contour. Thus, defining a propagation direction can be complex. Here, we define the direction of propagation as the normal vector of the jamming front. We will focus our analysis on the front propagation factor ( $k_f$ ), which is the front propagation speed normalized by cylinder velocity, and is calculated as

$$k_f = \frac{u_f}{|\mathbf{U}_c|} = \frac{u_f}{U_c}. \quad (7)$$

Note that for a given  $\alpha$  and  $U_{c0}$ , the data for  $k_f$  presented here are averaged values, thus not a function of time. A more detailed description can be found in Appendix A.

Figure 7 shows the front propagation as a function of the angle  $\alpha$  from the cylinder. Similar to Fig. 6 showing the scaled position of the front, the fact that the front propagation is different in the longitudinal and transverse directions is evident. In Fig. 7 this manifests as the two peaks in  $k_f$  at  $\alpha = \pi/2$  (in front of the cylinder) and  $\alpha = 3\pi/2$  (behind the cylinder), respectively. The inset of Fig. 7 demonstrates that if each  $k_f$  curve is normalized by its peak value all tests with  $U_{c0}/U_c^* - 1 \geq 2$  fundamentally have the same shape. It is worth pointing out that the peak value is always at  $\alpha = 3\pi/2$ , i.e., behind the cylinder, illustrating a repeatable asymmetry in the system.

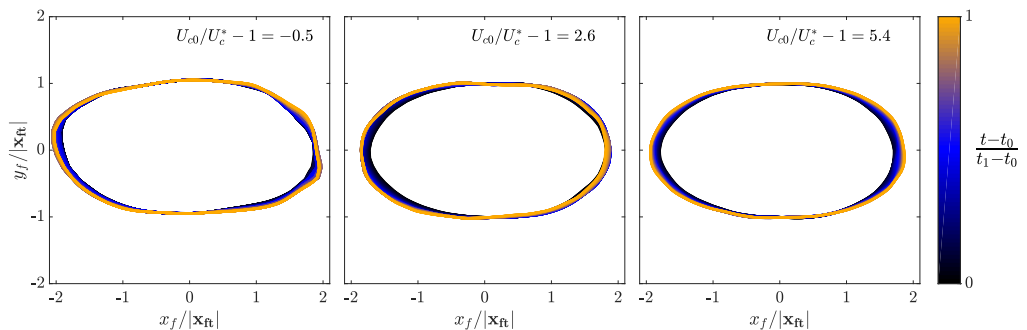


FIG. 6. The shape of the  $0.5U_c$  contour at three different velocities, indicated in the upper right in all figures. The color bar indicates time.  $t_0$  is the time at which the cylinder has accelerated to a constant speed, while  $t_1$  is when the cylinder stops, or the shape is influenced by interactions with the boundary.  $t_0$  and  $t_1$  are indicated by the dashed vertical lines in Fig. 3(b).

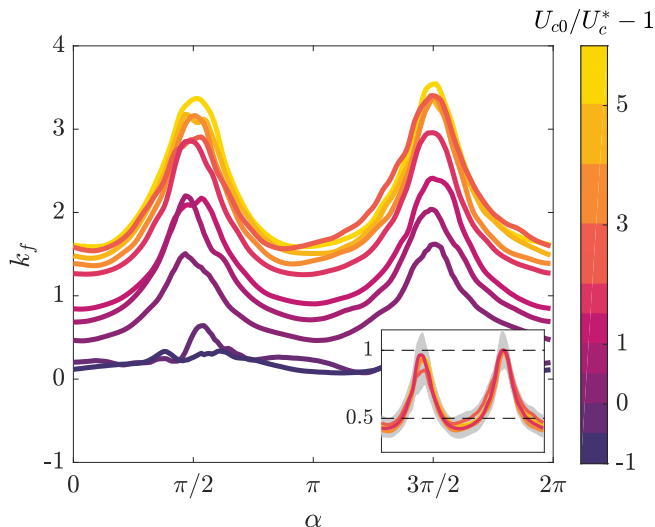


FIG. 7. Front propagation factor as a function of the angle from the cylinder. The inset shows the same plot for  $2 \leq U_{c0}/U_c^* - 1 \leq 6$ , but each curve from the main figure has been normalized with its maximum value. The gray region in the inset indicates one standard deviation from the collection of the time series. The peak at  $\alpha = 3\pi/2$  consistently has the highest value in these cases.

Another aspect of interest is how  $k_f$  develops as a function of the cylinder velocity  $U_{c0}$ . Below some nonzero cylinder velocity ( $U_c^*$ ),  $k_f \approx 0$ , meaning that the front is not propagating, thus the system is not jamming. On the other hand, as the cylinder velocity becomes sufficiently high,  $k_f$  tends towards some constant value  $k_f^*$ . That is, the  $k_f$ - $\alpha$  curves in Fig. 7 overlap for sufficiently high  $U_{c0}$ . The relationship between  $k_f$  and  $U_{c0}$  is investigated further by fitting the data to the curve [4]

$$k_f = \begin{cases} 0 & \text{for } U_{c0} \leq U_c^*, \\ k_f^*(1 - e^{1-U_{c0}/U_c^*}) & \text{for } U_{c0} > U_c^*. \end{cases} \quad (8)$$

We expand upon the work of Han *et al.* [4] by also looking at intermediate angles about the cylinder. Equation (8) has two free parameters:  $U_c^*$  and  $k_f^*$ . The physical meaning of these two values can be interpreted as follows:  $U_c^*$  represents the velocity below which jamming does not occur, and  $k_f^*$  represents the value  $k_f$  tends towards as  $U_{c0}$  becomes sufficiently high. The curve fit is performed by finding the minimum rms between the measured data and the curve from Eq. (8).

The inset in Fig. 8(a) shows  $k_f$ - $U_{c0}$  curves for two angles  $\alpha = 0$  (red) and  $\alpha = \pi/2$  (blue).  $\alpha = 0$  is an example of transverse front propagation, while  $\alpha = \pi/2$  is representative of longitudinal front propagation. Here we also see that the difference between transverse and longitudinal front propagation is roughly a factor of 2 [4]. When normalizing the data with  $k_f^*$  all data collapse on one curve as indicated in the main panel of Fig. 8(a). In Fig. 8(b), the two curve fit parameters  $U_c^*$  and  $k_f^*$  are plotted as functions of  $\alpha$ . Here,  $k_f^*$  has two strong peaks at  $\alpha = \pi/2$  and  $3\pi/2$ .  $U_c^*$ , on the other hand, does not show a strong dependence on  $\alpha$ .

Even though the front travels with different velocities in the transverse and longitudinal directions, it is noted from Fig. 4(c) that the accumulated strain ( $\epsilon_s$ ) has a roughly constant value in close proximity to the jamming front. That is, there is an onset strain associated with the transition from a liquidlike to a solidlike state. We quantify this onset strain by limiting our analysis to experiments where  $k_f$  is independent of  $U_{c0}$ . In our case, this is when  $U_{c0}/U_c^* - 1 \geq 2.2$ . By looking at the strain history associated with a material point, we define the onset strain ( $\epsilon_c$ ) as the point in time where  $u = 0.5U_c$ , that is, when the jamming front passes through the material point. This can be seen in Fig. 9(a). In order to check for dependence with the

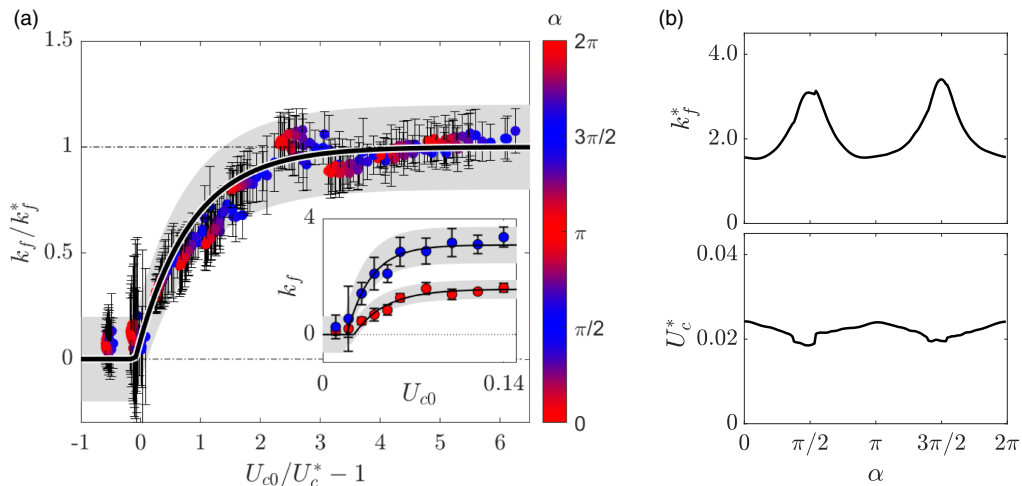


FIG. 8. (a) Scaled front propagation as a function of scaled cylinder velocity  $U_{c0}/U_c^* - 1$ . The curve fit with Eq. (8) is indicated by the solid black curve, while the shaded area represents the rms from the curve fit. The error bar associated with each point is one standard deviation from the collection of time series used at a specific  $\alpha$  and  $U_{c0}$ . The inset shows the front propagation compared to the cylinder velocity for  $\alpha = 0$  and  $\pi/2$ . (b) Resulting parameters for the curve fit in (a) as a function of  $\alpha$ .

location of the material points, we look at the mean and spread of  $\epsilon_c$  as a function of the angle the material points initially have with the cylinder ( $\alpha_0$ ). We do this by bundling the data for the onset strain in  $\approx 18^\circ$  intervals, and calculating the mean and standard deviation. This can be seen in Fig. 9(b) together with the global mean. As shown by Han *et al.* [4], the fact that the jamming front propagates with different speeds in the longitudinal and transverse directions is a direct consequence of the existence of an onset strain. By following the material points, we show that the accumulated strain at the jamming front has an approximately constant value for all angles about the cylinder. This shows that there is an underlying strain controlling the liquidlike to solidlike transition in the material, as is expected for systems of similar nature

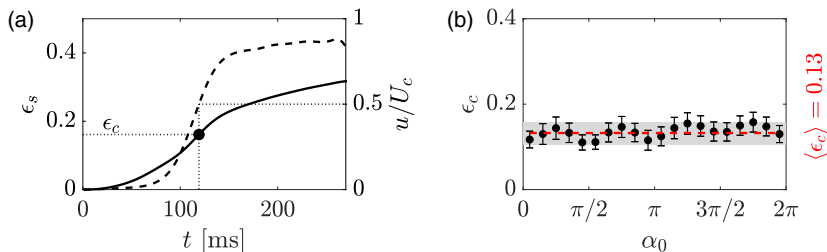


FIG. 9. Onset strain. (a) This plot shows the definition of  $\epsilon_c$ . The dashed line indicates velocity, while the solid line indicates accumulated strain. The dotted lines are simply for reference. This onset strain is defined as the strain at the point in time where the jamming front passes through that specific material point. The plot shows velocity and accumulated strain of a specific material point. As seen in the figure,  $\epsilon_c = \epsilon_s|_{u=0.5U_c}$ . (b) Onset strain as a function of initial angle the material point has with the cylinder ( $\alpha_0$ ). The data are taken from all cases where  $U_{c0}/U_c^* - 1 > 2.2$ . The onset strain is approximately independent of position relative to the cylinder compared to the front propagation, which has a clear transverse-longitudinal anisotropy as seen in Fig. 7. We do note that there is a weak longitudinal asymmetry in the accumulated strain. The onset strain is observed to be slightly higher behind the cylinder. This is also evident from the color band in Fig. 4(c).

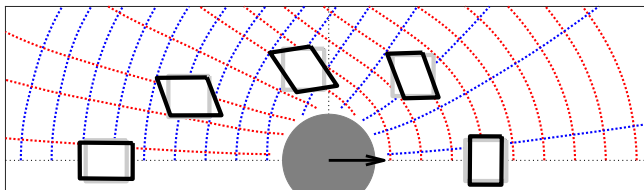


FIG. 10. Schematic representation of the deformation around the cylinder. This schematic is drawn using real data from the  $U_{c0}/U_c^* - 1 = 5.4$  case, at the end of the experiment where the region shown here has jammed. The scaled fluid parcels follow the flow. The dashed lines show the direction of principle elongation (red) and compression (blue). Note that the fluid parcel in the transverse position has rotated more than what one would expect from a simple shear. See [46] for a time resolved representation of the schematic.

[4,7,9–14]. We do note, however, that the onset strain shows slightly higher values behind the cylinder.

For the quasi-one-dimensional (1D), transient, simple shear system described in [7,8], a model linking the front propagation  $k$  with the packing fraction  $\phi$  was developed. In the experiment described here, we observe many of the phenomena expected from experiment of similar nature [2–6], that is, a constant front propagation with a relation  $\approx 1 : 2$  between the transverse and longitudinal direction. However, using the formula  $1/k^* = -\gamma^* \ln(\Phi)$  [7,8] ( $\Phi$  being a rescaled packing fraction) yields a value of  $k^* = 6.6$  which is significantly different from our value of  $k_f^* = 1.6$  in the transverse direction. Neither the variance in our measured  $k$  nor the uncertainty in  $\phi$  explains this discrepancy. However, in our system the perturbation is both back and forth in the laboratory frame. Even though the suspension has come to rest before it is perturbed again, we expect the distribution of particles in the suspension to still retain some anisotropy due to the strain history from the previous perturbation. This anisotropy manifests itself as the numerical value  $\gamma^*$  not being applicable in our case. It is also worth pointing out that our system is 2D, and we have no estimation for the full stress state in our system, as is the case in the quasi-1D, transient, simple shear system described in [7,8]. Two-dimensional effects can be seen in Fig. 4(d), showing the rotation and the movement of the material points. Notice from the deformed grid that the material in the transverse direction seems to have rotated more than one would expect from a simple shear in the laboratory frame. In the transverse direction it is primarily the velocity gradient component  $\partial u/\partial y$  that dominates, but an extra rotation comes from the fact that material is being pushed out in front of the cylinder, and sucked into the wake. This creates a  $\partial v/\partial x$  component with an opposite sign than the  $\partial u/\partial y$  component. As we calculate strain rate as the sum  $\approx \partial v/\partial x + \partial u/\partial y$  and rotation rate as  $\approx \partial v/\partial x - \partial u/\partial y$ , in an accumulated sense we expect the material points to have rotated more than one would expect from a simple shear, as seen from the deformed grids in Fig. 4(d) and the schematic in Fig. 10.

Although our results are symmetric in the transverse direction, a fore-aft asymmetry has been consistently observed throughout this paper. We quantify this asymmetry by mirroring the velocity ( $u$ ), strain rate ( $\dot{\gamma}_s$ ), and strain ( $\epsilon_s$ ) fields from Fig. 4 about the cylinder position and plotting the difference (Fig. 11). The mirrored fields are denoted with the subscript  $m$ . While the fore-aft difference in the onset strain ( $\epsilon_c$ ) and the front propagation factor ( $k_f$ ) is roughly the same magnitude as the measurement variance, there are significant and consistent differences in the mirrored kinematic fields as illustrated in Fig. 11. Specifically, the peak differences between the fore and aft regions of the cylinder are approximately 20, 50, and 50% for the velocity, strain rate, and accumulated strain, respectively. These differences are computed relative to the cylinder velocity, the strain rate defined by  $U_{c0}/D$ , and the onset strain, respectively. This indicates that while the magnitudes of  $k_f$  and  $\epsilon_c$  may only be mildly asymmetric, the spatial orientation of the fields is strongly asymmetric. This finding is accessible in the present experimental configuration, as the current set-up allows us to view the full field surrounding the cylinder.

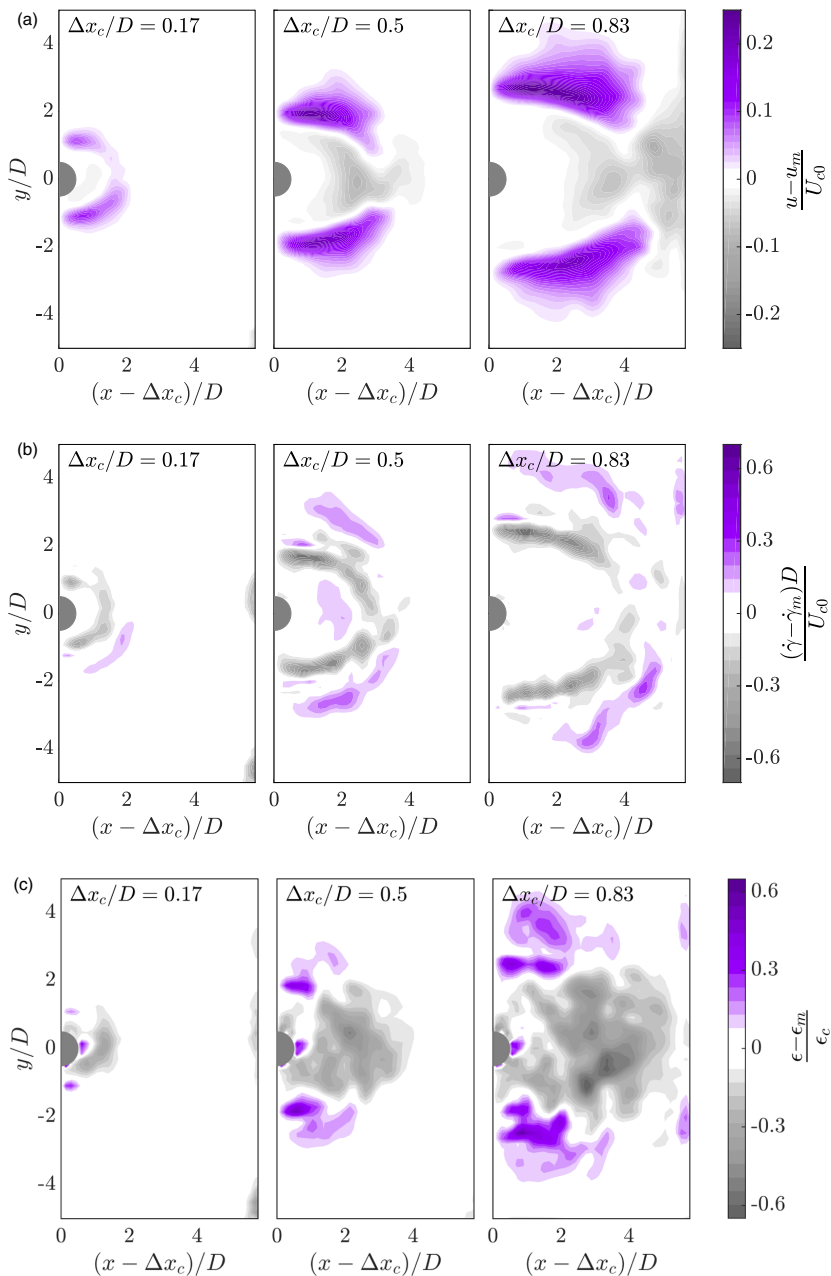


FIG. 11. Fore-aft asymmetry for the (a) velocity, (b) strain rate, and (c) accumulated strain. The asymmetry is computed by mirroring the fields in Fig. 4 about the center of the cylinder and plotting the difference between the fore and aft fields.

#### IV. CONCLUSION AND DISCUSSION

Experiments of a cylinder towed through a cornstarch–sucrose–water suspension were presented. The main goal was to investigate how the suspension behaved around a towed body in the domain where dynamic jamming occurs. By capturing high-speed images of the suspension surface, PIV

was used to compute 2D, time-resolved velocity fields. The full field surrounding the cylinder is visualized and pulling, pushing, and shearing are observed simultaneously. Here, we present measures of overall strain and rotation acquired from a polar decomposition of the deformation gradient tensor, inspired by common deformation measures in solid mechanics. This paper focused on the region in time where the cylinder was moving with a constant speed, and the front propagated through the suspension unaffected by the boundary.

Though the setup is different from previous studies, we see several similarities. For a sufficiently high cylinder velocity, the dimensionless front propagation speed is independent of cylinder velocity, and the front travels roughly twice as fast in the longitudinal compared to the transverse direction. In addition, an onset strain of  $\epsilon_c = 0.13$  accompanies the jamming front as it propagates through the suspension regardless of position relative to the cylinder.

Even though our results are symmetrical in the transverse direction, a longitudinal (fore-aft) asymmetry has been consistently observed throughout this paper. Particularly, the velocity ( $u$ ), strain rate ( $\dot{\gamma}_s$ ), strain ( $\epsilon_s$ ), and rotation ( $\psi$ ) in Fig. 4 all indicate this. By mirroring the fields about the cylinder position, the asymmetry is quantified in Fig. 11. The fore-aft asymmetry is also visible in the front propagation factor  $k_f$  and the onset strain  $\epsilon_c$  [Fig. 9(b)], to a lesser degree.

As noted in the discussion above, it has been shown how strain influences the flow for simpler systems [8], where strain reduces down to a scalar. Other experiments investigating shear jamming fronts in more complex systems focus only on the behavior in front of [2,4,5] or behind [1] the perturbing body separately, thus the jamming front produced in these studies propagates in the fore or aft half planes only. Given the moderately large strains observed in our experiment (larger than a few percent [48]) there is no *a priori* basis to assume fore-aft symmetry. With our system, we are able to observe and quantify a fore-aft asymmetry.

Data supporting this paper are openly available from the University of Southampton repository [49].

## ACKNOWLEDGMENTS

R.J.H. acknowledges the financial support of the Research Council of Norway (Grant No. 288046). I.R.P. acknowledges financial support from the Royal Society (Grant No. RG160089).

## APPENDIX A: JAMMING FRONT AND FRONT PROPAGATION

From the PIV analysis we get a transient 2D velocity field  $\mathbf{u} = \{u, v\}$ . The jamming front is defined as the points in the suspension where the velocity is half the velocity of the cylinder [1–4,6]. The cylinder is moving in the positive  $x$  direction with velocity  $U_c$ , such that  $\mathbf{U}_c = \{U_c, 0\}$ . From Fig. 2(d) we define the location of the jamming front relative to the cylinder as

$$\mathbf{x}_f = \mathbf{x}|_{u=0.5U_c} - \mathbf{x}_c. \quad (\text{A1})$$

This involves a Galilean transformation; that is, we look at the location of the jamming front relative to the cylinder. Furthermore, the velocity of the jamming front is defined as

$$u_f = \left( \frac{d}{dt} \mathbf{x}_f \right) \cdot \mathbf{n}_f \quad (\text{A2a})$$

$$= \left[ \frac{d}{dt} (\mathbf{x}|_{u=0.5U_c} - \mathbf{x}_c) \right] \cdot \mathbf{n}_f \quad (\text{A2b})$$

$$= \left( \frac{d\mathbf{x}|_{u=0.5U_c}}{dt} - \mathbf{U}_c \right) \cdot \mathbf{n}_f, \quad (\text{A2c})$$

where the jamming front normal vector  $\mathbf{n}_f$  is calculated as

$$\mathbf{n}_f = \begin{pmatrix} 0 & 1 \\ -1 & 0 \end{pmatrix} \frac{d\mathbf{x}_f}{d\alpha} \frac{1}{\left| \frac{d\mathbf{x}_f}{d\alpha} \right|}. \quad (\text{A3})$$

As the jamming front does not correspond to material points, but a velocity contour, we define its propagation direction to be in the direction of the jamming front normal vector  $\mathbf{n}_f$ . Figure 3(a) shows the connection between the velocity profile and the location of the jamming front.

The front propagation factor ( $k_f$ ) is defined in Eq. (7). We will focus on averaged results. For a given  $\alpha$  and  $U_c$ , the front propagation  $k_f$  is presented as an average over the time window of analysis for all relevant cases [see Fig. 3(b)]. This is calculated from a minimum of 13 cases for each set of  $\alpha$  and  $U_c$ .

In regions where the front normal vector is pointing in the transverse ( $\mathbf{n}_f = \{0, 1\}$ ) or longitudinal ( $\mathbf{n}_f = \{1, 0\}$ ) direction, the relations

$$k_{ft} = \frac{1}{U_c} \frac{d}{dt} (y|_{u=0.5U_c}), \quad (\text{A4a})$$

$$k_{fl} = \frac{1}{U_c} \frac{d}{dt} (x|_{u=0.5U_c}) - 1 \quad (\text{A4b})$$

are recovered, similar to Han *et al.* [4].

## APPENDIX B: STRAIN, STRAIN RATE, AND ROTATION

Data for strain and strain rate are presented as scalar fields in the main text. We define the scalar strain rate as the shear rate magnitude [48]

$$\dot{\gamma}_s = \sqrt{2\|\mathbf{D}\|^2}, \quad (\text{B1})$$

and the strain as

$$\epsilon_s = \sqrt{\|\mathbf{e}\|^2}. \quad (\text{B2})$$

Here,  $\mathbf{D} = \frac{1}{2}(\frac{\partial \mathbf{u}}{\partial \mathbf{x}} + \frac{\partial \mathbf{u}^T}{\partial \mathbf{x}})$  represents the strain rate tensor, and  $\mathbf{e}$  is the Eulerian logarithmic strain measure. Logarithmic strain is defined based on the strain increment  $d\epsilon = dl/l$  and is calculated as [48]

$$\epsilon = \int \frac{dl}{l} = \ln\left(\frac{l_f}{l_0}\right) = \ln(\lambda). \quad (\text{B3})$$

Here,  $l_f$  and  $l_0$  are the final and initial lengths of a line segment, while  $\lambda$  is a principle stretch. This definition of strain is in some sources referred to as Hencky, natural, or true strain [48,50–52]. Here, we use the definition of logarithmic strain from [47], which has the spectral representation

$$\mathbf{e} = \sum_i \ln(\lambda_i) \mathbf{n}_i \otimes \mathbf{n}_i. \quad (\text{B4})$$

$\lambda_i$  and  $\mathbf{n}_i$  are the principle values and principle directions of the left stretch tensor  $\mathbf{V}$ . Note that  $\mathbf{V}$  is a positive definite symmetric tensor with positive real principle values. The following steps are taken when calculating the left stretch tensor, and ultimately  $\epsilon_s$ .

(1) In order to calculate the stretch in the material, an estimate of the movement of the material points is needed.  $\mathbf{X} = \{X, Y\}$  refers to a material point in our initial configuration at  $t = 0$ . At any

time  $t$ , a material point, located at  $\mathbf{X}$  in the initial configuration, has moved to the point  $\mathbf{x}_p(\mathbf{X}, t) = \{x_p(t), y_p(t)\}$ . The movement of a material point is estimated from the PIV data as [53]

$$x_p(t_n) = X + \sum_{t_i=0}^{t_n} u[x_p(t_i), y_p(t_i), t_i] \Delta t, \quad (\text{B5a})$$

$$y_p(t_n) = Y + \sum_{t_i=0}^{t_n} v[x_p(t_i), y_p(t_i), t_i] \Delta t, \quad (\text{B5b})$$

where  $\Delta t$  is given by the framerate.

(2) With the movement of the material points, we are able to calculate the deformation gradient tensor ( $\mathbf{F} = \frac{\partial \mathbf{x}_p}{\partial \mathbf{X}}$ ). The left stretch tensor  $\mathbf{V}$  is acquired by a polar decomposition  $\mathbf{F} = \mathbf{V}\mathbf{R} = \mathbf{R}\mathbf{U}$  [47,48,52].

(3) The principle values ( $\lambda_i$ ) and principle directions ( $\mathbf{n}_i$ ) of  $\mathbf{V}$  are calculated. We order the principle values such that  $\lambda_1 > \lambda_2$ , which results in  $\lambda_1$  and  $\mathbf{n}_1$  signifying the amount and direction of extension, while  $\lambda_2$  and  $\mathbf{n}_2$  signify the amount and direction of compression. By closer inspection of Eqs. (B2) and (B4), we calculate the strain as  $\epsilon_s = \sqrt{[\ln(\lambda_1)]^2 + [\ln(\lambda_2)]^2}$ .

We choose the left stretch tensor  $\mathbf{V}$  rather than the right stretch tensor  $\mathbf{U}$ , as the strain will be presented in the deformed configuration. This has no consequence for Eq. (B2), as the principal values of  $\mathbf{U}$  and  $\mathbf{V}$  are equal. It is the principal directions that differ. The principal direction of  $\mathbf{U}$  signifies the axis of principal stretch relative to the initial configuration, while the principal direction of  $\mathbf{V}$  signifies the axis of principal stretch relative to the deformed configuration.

We also present the rotation of the material points  $\psi$ . This angle is calculated from the rotation matrix obtained from the polar decomposition above. As seen from the formulas  $\mathbf{U} = \mathbf{R}^T \mathbf{V} \mathbf{R}$  and  $\mathbf{R}^T \mathbf{R} = \mathbf{I}$ ,  $\mathbf{R}$  represents a change of basis between the principle stretches viewed in the reference configuration and the deformed configuration. In two dimensions, the elements of  $\mathbf{R}$  are

$$\mathbf{R} = \begin{pmatrix} \cos(\psi) & -\sin(\psi) \\ \sin(\psi) & \cos(\psi) \end{pmatrix}, \quad (\text{B6})$$

and the rotation angle of the material points is simply calculated as  $\cos(\psi) = \frac{1}{2} \text{tr } \mathbf{R}$ .

- 
- [1] S. Majumdar, I. R. Peters, E. Han, and H. M. Jaeger, Dynamic shear jamming in dense granular suspensions under extension, *Phys. Rev. E* **95**, 012603 (2017).
  - [2] I. R. Peters and H. M. Jaeger, Quasi-2D dynamic jamming in cornstarch suspensions: Visualization and force measurements, *Soft Matter* **10**, 6564 (2014).
  - [3] S. R. Waitukaitis and H. M. Jaeger, Impact-activated solidification of dense suspensions via dynamic jamming fronts, *Nature (London)* **487**, 205 (2012).
  - [4] E. Han, I. R. Peters, and H. M. Jaeger, High-speed ultrasound imaging in dense suspensions reveals impact-activated solidification due to dynamic shear jamming, *Nat. Commun.* **7**, 12243 (2016).
  - [5] E. Han, L. Zhao, N. Van Ha, S. T. Hsieh, D. B. Szyld, and H. M. Jaeger, Dynamic jamming of dense suspensions under tilted impact, *Phys. Rev. Fluids* **4**, 063304 (2019).
  - [6] I. R. Peters, S. Majumdar, and H. M. Jaeger, Direct observation of dynamic shear jamming in dense suspensions., *Nature (London)* **532**, 214 (2016).
  - [7] E. Han, M. Wyart, I. R. Peters, and H. M. Jaeger, Shear fronts in shear-thickening suspensions, *Phys. Rev. Fluids* **3**, 073301 (2018).
  - [8] E. Han, N. M. James, and H. M. Jaeger, Stress Controlled Rheology of Dense Suspensions using Transient Flows, *Phys. Rev. Lett.* **123**, 248002 (2019).



- [9] D. Wang, J. Ren, J. A. Dijksman, H. Zheng, and R. P. Behringer, Microscopic Origins of Shear Jamming for 2D Frictional Grains, *Phys. Rev. Lett.* **120**, 208004 (2018).
- [10] R. Pastore, M. P. Ciamarra, and A. Coniglio, “Flow and jam” of frictional athermal systems under shear stress, *Philos. Mag.* **91**, 2006 (2011).
- [11] D. Bi, J. Zhang, B. Chakraborty, and R. P. Behringer, Jamming by shear, *Nature (London)* **480**, 355 (2011).
- [12] T. S. Majmudar and R. P. Behringer, Contact force measurements and stress-induced anisotropy in granular materials, *Nature (London)* **435**, 1079 (2005).
- [13] S. Khandavalli and J. P. Rothstein, Large amplitude oscillatory shear rheology of three different shear-thickening particle dispersions, *Rheol. Acta* **54**, 601 (2015).
- [14] A. Fall, F. Bertrand, G. Ovarlez, and D. Bonn, Shear thickening of cornstarch suspensions, *J. Rheol.* **56**, 575 (2012).
- [15] N. M. James, E. Han, R. A. L. Cruz, J. Jureller, and H. M. Jaeger, Interparticle hydrogen bonding can elicit shear jamming in dense suspensions, *Nat. Mater.* **17**, 965 (2018).
- [16] E. Brown and H. M. Jaeger, The role of dilation and confining stresses in shear thickening of dense suspensions, *J. Rheol.* **56**, 875 (2012).
- [17] E. Brown and H. M. Jaeger, Shear thickening in concentrated suspensions: Phenomenology, mechanisms and relations to jamming, *Rep. Prog. Phys.* **77**, 046602 (2014).
- [18] I. R. Peters, Q. Xu, and H. M. Jaeger, Splashing Onset in Dense Suspension Droplets, *Phys. Rev. Lett.* **111**, 028301 (2013).
- [19] E. Brown, H. Zhang, N. A. Forman, B. W. Maynor, D. E. Betts, J. M. DeSimone, and H. M. Jaeger, Shear thickening and jamming in densely packed suspensions of different particle shapes, *Phys. Rev. E* **84**, 031408 (2011).
- [20] N. M. James, H. Xue, M. Goyal, and H. M. Jaeger, Controlling shear jamming in dense suspensions via the particle aspect ratio, *Soft Matter* **15**, 3649 (2019).
- [21] A. J. Liu and S. R. Nagel, The jamming transition and the marginally jammed solid, *Annu. Rev. Condens. Matter Phys.* **1**, 347 (2010).
- [22] A. Singh, R. Mari, M. M. Denn, and J. F. Morris, A constitutive model for simple shear of dense frictional suspensions, *J. Rheol.* **62**, 457 (2018).
- [23] V. Sivasadan, E. Lorenz, A. G. Hoekstra, and D. Bonn, Shear thickening of dense suspensions: The role of friction, *Phys. Fluids* **31**, 103103 (2019).
- [24] F. Tapia, O. Pouliquen, and E. Guazzelli, Influence of surface roughness on the rheology of immersed and dry frictional spheres, *Phys. Rev. Fluids* **4**, 104302 (2019).
- [25] Y. Madraki, S. Hormozi, G. Ovarlez, E. Guazzelli, and O. Pouliquen, Enhancing shear thickening, *Phys. Rev. Fluids* **2**, 033301 (2017).
- [26] N. Fernandez, R. Mani, D. Rinaldi, D. Kadau, M. Mosquet, H. Lombois-Burger, J. Cayer-Barrioz, H. J. Herrmann, N. D. Spencer, and L. Isa, Microscopic Mechanism for Shear Thickening of Non-Brownian Suspensions, *Phys. Rev. Lett.* **111**, 108301 (2013).
- [27] B. M. Guy, M. Hermes, and W. C. K. Poon, Towards a Unified Description of the Rheology of Hard-Particle Suspensions, *Phys. Rev. Lett.* **115**, 088304 (2015).
- [28] Z. Pan, H. de Cagny, B. Weber, and D. Bonn, S-shaped flow curves of shear thickening suspensions: Direct observation of frictional rheology, *Phys. Rev. E* **92**, 032202 (2015).
- [29] M. Hermes, M. Guy, W. C. K. Poon, G. Poy, M. E. Cates, and M. Wyart, Unsteady flow and particle migration in dense, non-Brownian suspensions, *J. Rheol.* **60**, 905 (2016).
- [30] B. Saint-Michel, T. Gibaud, and S. Manneville, Uncovering Instabilities in the Spatiotemporal Dynamics of a Shear-Thickening Cornstarch Suspension, *Phys. Rev. X* **8**, 031006 (2018).
- [31] R. Mari, R. Seto, J. F. Morris, and M. M. Denn, Nonmonotonic flow curves of shear thickening suspensions, *Phys. Rev. E* **91**, 052302 (2015).
- [32] R. Seto, R. Mari, J. F. Morris, and M. M. Denn, Discontinuous Shear Thickening of Frictional Hard-Sphere Suspensions, *Phys. Rev. Lett.* **111**, 218301 (2013).
- [33] R. Mari, R. Seto, J. F. Morris, and M. M. Denn, Shear thickening, frictionless and frictional rheologies in non-Brownian suspensions, *J. Rheol.* **58**, 1693 (2014).

- [34] T. Kawasaki and L. Berthier, Discontinuous shear thickening in Brownian suspensions, *Phys. Rev. E* **98**, 012609 (2018).
- [35] C. Heussinger, Shear thickening in granular suspensions: Interparticle friction and dynamically correlated clusters, *Phys. Rev. E* **88**, 050201(R) (2013).
- [36] B. M. Guy, C. Ness, M. Hermes, L. J. Sawiak, J. Sun, and W. C. K. Poon, Testing the Wyart-Cates model for non-Brownian shear thickening using bidisperse suspensions, *Soft Matter* **16**, 229 (2020).
- [37] J. F. Morris, Lubricated-to-frictional shear thickening scenario in dense suspensions, *Phys. Rev. Fluids* **3**, 110508 (2018).
- [38] S. Jamali and J. F. Brady, Alternative Frictional Model for Discontinuous Shear Thickening of Dense Suspensions: Hydrodynamics, *Phys. Rev. Lett.* **123**, 138002 (2019).
- [39] M. Wyart and M. E. Cates, Discontinuous Shear Thickening without Inertia in Dense Non-Brownian Suspensions, *Phys. Rev. Lett.* **112**, 098302 (2014).
- [40] S. R. Waitukaitis, L. K. Roth, V. Vitelli, and H. M. Jaeger, Dynamic jamming fronts, *Europhys. Lett.* **102**, 44001 (2013).
- [41] J. Garside and M. R. Al-Dibouni, Velocity-voidage relationships for fluidization and sedimentation in solid-liquid systems, *Ind. Eng. Chem. Process. Des. Dev.* **16**, 206 (1977).
- [42] J. Richardson and W. Zaki, Sedimentation and fluidisation: Part 1, *Chem. Eng. Res. Des.* **75**, S82 (1997).
- [43] E. Han, N. Van Ha, and H. M. Jaeger, Measuring the porosity and compressibility of liquid-suspended porous particles using ultrasound, *Soft Matter* **13**, 3506 (2017).
- [44] A. S. Baumgarten and K. Kamrin, A general constitutive model for dense, fine-particle suspensions validated in many geometries, *Proc. Natl. Acad. Sci. USA* **116**, 20828 (2019).
- [45] T. Schmidt, Viskositäts- und oberflächenspannungsverhalten von reinen und technischen saccharoselösungen, Ph.D. thesis, Technische Universität Berlin, Fakultät III–Prozesswissenschaften, Berlin, 2000.
- [46] See Supplemental Material at <http://link.aps.org/supplemental/10.1103/PhysRevFluids.6.063301> for example movie snippets.
- [47] S. Nemat-Nasser, *Plasticity: A Treatise on Finite Deformation of Heterogeneous Inelastic Materials*, Cambridge Monographs on Mechanics (Cambridge University Press, Cambridge, 2004).
- [48] F. Irgens, *Continuum Mechanics* (Springer-Verlag, Berlin, 2008).
- [49] Data available from the University of Southampton repository, <https://doi.org/10.5258/SOTON/D1835>.
- [50] Z. P. Bazant, Easy-to-compute tensors with symmetric inverse approximating Hencky finite strain and its rate, *J. Eng. Mater. Technol.* **120**, 131 (1998).
- [51] J. E. Fitzgerald, A tensorial Hencky measure of strain and strain rate for finite deformations, *J. Appl. Phys.* **51**, 5111 (1980).
- [52] D. Rees, *Basic Engineering Plasticity: An Introduction with Engineering and Manufacturing Applications* (Elsevier, Amsterdam, 2006).
- [53] D. Boutelier, C. Schrank, and K. Regenauer-Lieb, 2-D finite displacements and strain from particle imaging velocimetry (PIV) analysis of tectonic analogue models with TecPIV, *Solid Earth* **10**, 1123 (2019).



Article II

---

**Characterizing the surface texture of a  
dense suspension undergoing dynamic  
jamming**

---

Olav Rømcke, Ivo R. Peters, R. Jason Hearst

*Published*  
*Experiments in Fluids*, **62**, 226.





# Characterizing the surface texture of a dense suspension undergoing dynamic jamming

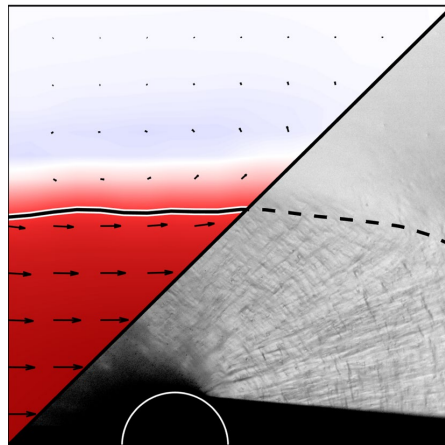
Olav Rømcke<sup>1</sup> · Ivo R. Peters<sup>2</sup> · R. Jason Hearst<sup>1</sup>

Received: 28 June 2021 / Revised: 3 September 2021 / Accepted: 16 September 2021  
© The Author(s) 2021

## Abstract

Measurements of the surface velocity and surface texture of a freely propagating shear jamming front in a dense suspension are compared. The velocity fields are captured with particle image velocimetry (PIV), while the surface texture is captured in a separated experiment by observing a direct reflection on the suspension surface with high-speed cameras. A method for quantifying the surface features and their orientation is presented based on the fast Fourier transform of localized windows. The region that exhibits strong surface features corresponds to the solid-like jammed region identified via the PIV measurements. Moreover, the surface features within the jammed region are predominantly oriented in the same direction as the eigenvectors of the strain tensor. Thus, from images of the free surface, our analysis is able to show that the surface texture contains information on the principle strain directions and the propagation of the jamming front.

## Graphic Abstract



## 1 Introduction

Suspensions of hard spheres in a Newtonian fluid are known to jam at a critical volume fraction (Krieger 1972). That is, beyond a critical concentration of particles, flow ceases, and a finite yield stress is observed Brown and Jaeger (2014). However, for some suspensions, such as cornstarch and water, a jammed state is accessible for volume fractions lower than the critical volume fraction when stress is applied

✉ R. Jason Hearst  
jason.hearst@ntnu.no

<sup>1</sup> Department of Energy and Process Engineering, Norwegian University of Science and Technology, Kolbjørn Hejes vei 2, NO-7491 Trondheim, Norway

<sup>2</sup> Faculty of Engineering and Physical Sciences, University of Southampton Highfield, Southampton SO17 1BJ, UK

(Wyart and Cates 2014; Peters et al 2016). This rather counter intuitive phenomenon is called dynamic jamming or shear jamming, where the suspension appears fluid-like at low stress, but shear thickens and even jams with sufficiently high stress. As such, a sudden impact causes the suspension to jam (Waitukaitis and Jaeger 2012; Jerome et al 2016), which explains how it is possible to stay afloat while running over a cornstarch suspension (Mukhopadhyay et al 2018; Baumgarten and Kamrin 2019).

The assumption of smooth, force free particles in non-Brownian, non-inertial systems, where viscosity is only a function of the volume fraction,  $\phi$  (Stickel and Powell 2005), does not capture this behavior. In real suspensions, particle-particle interactions are an important contributor to the observed behavior (Lin et al 2015; Gadala-Maria and Acrivos 1980; Brown and Jaeger 2014). Between particles, it has been identified that friction (Mari et al 2014; Singh et al 2018; Sivadasan et al 2019; Tapia et al 2019; Madraki et al 2017; Fernandez et al 2013) and repulsive forces (Brown and Jaeger 2014; James et al 2018; Guy et al 2015) are underlying mechanisms for understanding this phenomenon. With a sufficient amount of applied stress, the particles overcome the repulsive force and are brought into frictional contact. At sufficiently high particle concentrations, the contacts form a network capable of supporting the applied stresses.

In sufficiently large domains, the transition from fluid-like to solid-like is observed as a front of high shear rate that propagates from the perturbing body through the suspension and leaves a jammed state in its wake (Waitukaitis and Jaeger 2012; Peters and Jaeger 2014; Han et al 2016; Peters et al 2016; Majumdar et al 2017; Han et al 2018, 2019b; Baumgarten and Kamrin 2019; Rømcke et al 2021). In these works, the jamming front is defined by the velocity contour at half the velocity of the perturbing body, i.e.,  $0.5U_c$ . A normalized front propagation factor is used to quantify how fast the front moves, defined by the relation between the speed of the  $0.5U_c$ -contour and the perturbing body. The front propagation factor is observed to increase with volume fraction and is independent of perturbing speed for sufficiently high velocities (Han et al 2016; Rømcke et al 2021). This phenomenology is caused by an intrinsic strain (Han et al 2019a; Baumgarten and Kamrin 2019) which is needed in order for the material to build a frictional contact network capable of supporting the applied stresses. The strain level decreases with increasing volume fraction and has an inverse relationship with the front propagation factor (Han et al 2019a).

Most measurement set-ups employed to investigate this problem have a free surface, and as such, the effects of the free surface have been identified as an important question in suspension flow (Denn et al 2018). One interesting feature is the existence of two statically stable states (Cates et al 2005; Cates and Wyart 2014) known as granulation. The material can exist as a flowable droplet with a shiny

surface, or in a stressed state as a jammed, pasty granule upheld by capillary forces. A closely linked observable surface feature in dense suspension flow is dilation (Brown and Jaeger 2012; Jerome et al 2016; Maharjan et al 2021). For a sufficiently dense suspension, the granular structure expands under shear, which sets up a suction in the liquid phase. Dilation can thus be observed at the free surface as a transition from reflective to matte as individual particles protrude through the liquid-air interface. Dilation is associated with a large increase in stress (Maharjan et al 2021), and coupled with the suspending fluid pressure (Jerome et al 2016) is able to explain the fluid-solid transition observed in impact experiments with a solid sphere. For a shear jamming front under extension, a reflective-matte transition is observed when the front interacts with the wall (Majumdar et al 2017).

A corrugated free surface has been reported for a wide range of particle sizes and packing fractions and in several experimental setups (Loimer et al 2002; Timberlake and Morris 2005; Singh et al 2006; Kumar et al 2016). In the inclined plane experiment by Timberlake and Morris (2005), two dimensional (2D) power spectra of free surface images indicate that the features exhibit anisotropy, specifically, the corrugations are shorter in the flow direction. Probably more applicable to the work herein is that of Loimer et al (2002) who conducted experiments in an approximately 2D belt driven shear cell with the free surface normal in the vorticity direction. Power spectra in the flow and gradient directions, respectively, also indicate anisotropy. However, how these features appear in the full 2D power spectra remains unclear. The deformation of the free surface is a result of shear induced normal stresses (Timberlake and Morris 2005; Brown and Jaeger 2012), typically observed in dense suspensions (Brown and Jaeger 2014; Guazzelli and Pouliquen 2018; Denn et al 2018). That is, upon shearing, the material responds with a force normal to the confining boundary. Although several experiments investigating the dynamic jamming front phenomenon exhibit a large free surface (Peters and Jaeger 2014; Han et al 2018; Rømcke et al 2021), few studies have dedicated attention to the developing surface texture as the front propagates through the suspension (Allen et al 2018).

In this work, we present observations of the free surface texture as the jamming front propagates unimpeded through the suspension. The aim of the method presented here is to draw quantifiable information from high-speed photographs of the free surface alone, without the need for more complex techniques, e.g., particle image velocimetry (PIV). The result from the free surface images is compared with the velocity field, front propagation and the strain tensor acquired from PIV measurements.

**Fig. 1** Schematic of the experimental set-up. **a** PIV set-up with two cameras, **b** texture set-up with the backlit acrylic plate and **c** birds-eye-view of the suspension surface with the dotted square indicating the investigation region of the present study. In the images, the beige layer represents the suspension, and the blue layer beneath it represents a layer of Fluorinert

## 2 Experimental procedure

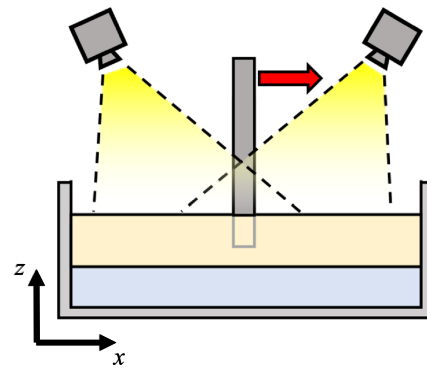
The data used here are collected from two different experiments. A single cylinder is traversed through a layer of cornstarch and sucrose-water suspension. First, as a reference, the free surface was seeded with black pepper. High-speed images of the suspension surface were captured under indirect lighting. PIV was conducted on these particle images, resulting in a time resolved velocity field. Secondly, by minor adjustments to the set-up, we record the free surface. In this case, the suspension is not seeded, while the camera was positioned such that it observed a direct reflection on the free surface, enhancing the visibility of any surface features.

The experimental set-ups are shown in Fig. 1. Both experiments are conducted in a 1 m × 0.5 m tank. The tank is first filled with a 15-mm-layer of high density, low viscosity Fluorinert oil (FC74) (Loimer et al 2002; Peters and Jaeger 2014; Han et al 2018; Rømcke et al 2021), followed by a 15-mm-thick suspension layer consisting of cornstarch (*Mai-zena maisstivelse*) and a sucrose-water solution (50% wt) at a nominal volume fraction of  $\phi = 0.36$  (Rømcke et al 2021), defined as

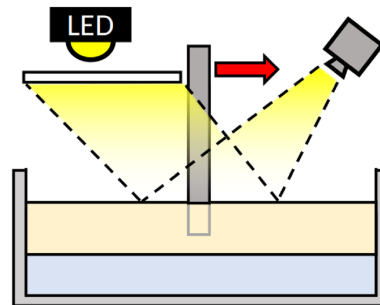
$$\phi = \frac{(1 - \beta)m_s / \rho_s}{(1 - \beta)m_s / \rho_s + m_l / \rho_l + \beta m_s / \rho_w} \tag{1}$$

Here,  $\beta = 11\%$  is the water content in the starch, while  $m_s$  and  $m_l$  are the measured mass of starch and sucrose solution, respectively. The densities of the starch, sucrose solution and water are  $\rho_s = 1.63$  g/ml,  $\rho_l = 1.23$  g/ml and  $\rho_w = 1.0$  g/ml, respectively. We mix the suspension for two hours before it is loaded into the tank. The suspension floats atop the denser Fluorinert ( $\sim 1.8$  g/ml), which ensures a near stress free bottom boundary and makes the system approximately 2D (Peters and Jaeger 2014). A 25-mm-diameter ( $D$ ) cylinder is submerged in the suspension and is traversed at a velocity of  $U_c = 0.14$  m/s; the effect of changing  $U_c$  is the subject of a previous study (Rømcke et al 2021). Both the cylinder velocity ( $U_c > 0.06$  m/s) and volume fraction ( $\phi_m < \phi < \phi_0$ ) are in a range where dynamic jamming is known to occur for this suspension (Rømcke et al 2021).

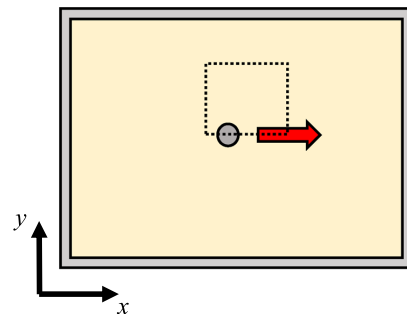
The suspension is pre-sheared by towing the cylinder back and forth equivalent to an actual run, before any measurements are taken. When capturing particle images for the PIV, two 4 megapixel high-speed cameras (Photron FAST-CAM Mini WX100) view the suspension surface in front



(a)



(b)



(c)



and behind the traversing cylinders (Fig. 1a). Pulsed LED lighting was used to illuminate the surface and was synchronized with the camera acquisition at 750 Hz. The particle images were converted to velocity fields with LaVision DaVis 8.4.0 PIV software. An initial pass was performed with 96 pixels  $\times$  96 pixels square interrogation windows, followed by two passes with circular interrogation windows with decreasing size ending at 48 pixels  $\times$  48 pixels. For all passes, the interrogation windows have a 50% overlap. The resulting instantaneous velocity fields are stitched together in post processing, masking out the cylinder in each frame. This results in a velocity field fully surrounding the cylinder.

As mentioned above, only minor adjustments to the setup are needed in order to observe the surface features. This is illustrated in Fig. 1b. Here, a single camera is positioned such that it views a direct reflection of a backlit, semi-transparent, acrylic sheet on the suspension surface. This enhances any surface features not captured by the PIV; note that the tracer particles used for PIV also interfere with the detection of the surface topology, which is why a separate campaign was used for surface texture measurements. Figure 1c gives a birds eye view of the suspension surface. For the scope of this work, we focus on the region indicated by the dotted square. See Rømcke et al (2021) for details on the full velocity field.

For the texture images, LaVision Davis 8.4.0 was used to find a third order calibration polynomial, mapping the image coordinates  $(i, j)$  to the lab coordinates  $(x, y)$ . MATLAB was used for all further processing of the texture images. Here, for consistency, the results are always plotted in the calibrated lab coordinate system  $(x, y)$ . However, calculations on the surface features are done in pixel coordinates  $(i, j)$ , and the results in  $(i, j)$  are mapped to  $(x, y)$  with the calibration polynomial.

Examples of both the PIV and texture images are shown in Fig. 2. The cylinder position is denoted  $x_c$ , which starts as  $x = 0$  and moves in the positive  $x$ -direction. The raw particle images (Fig. 2a–d) do not provide any information on the suspension texture. The resulting velocity fields from the PIV analysis of these images are shown in Fig. 2e–h. Note the sharp transition in velocity that propagates away from the cylinder as it moves through the flow. By the end of an experimental run, the whole field of view is moving with the cylinder as shown in Fig. 2h. The  $0.5U_c$  contour is represented by the black line and used as a proxy for the position of the jamming front as is common in previous studies (Waitukaitis and Jaeger 2012; Peters and Jaeger 2014; Peters et al 2016; Han et al 2016, 2018, 2019b, a; Rømcke et al 2021).

From the velocity data, we estimate the local accumulated strain. The strain is shown to be an important parameter with regards to jamming. Given that the suspension is subjected to a sufficient amount of stress, an intrinsic onset strain dictates the amount of strain needed before the suspension transitions into a jammed state (Majumdar et al 2017; Han et al 2016, 2019a; Rømcke et al 2021). The nominal value of the onset strain depends on the volume fraction (Han et al 2016, 2018, 2019a). We define the strain in the same manner as Rømcke et al (2021). In short, by estimating the movement of the material points  $\mathbf{x}_p(\mathbf{X}, t) = \mathbf{X} + \int_0^t \mathbf{u}(\mathbf{x}_p(\tau), \tau) d\tau$ , we calculate the deformation gradient tensor  $\mathbf{F} = \frac{\partial \mathbf{x}_p}{\partial \mathbf{X}}$ , where  $\mathbf{X}$  is the position of the material points at  $t = 0$ . From the deformation gradient, the left stretch tensor  $\mathbf{V}$  is acquired from a polar decomposition  $\mathbf{F} = \mathbf{V}\mathbf{R}$ . The tensor  $\mathbf{V}$  has eigenvalues and eigenvectors,  $\lambda$  and  $\mathbf{n}$ , respectively. Here, we employ the Eulerian logarithmic strain tensor (Nemat-Nasser 2004)

$$\boldsymbol{\epsilon} = \sum_i \ln(\lambda_i) \mathbf{n}_i \otimes \mathbf{n}_i. \quad (2)$$

Eigenvalues are ordered  $\lambda_1 > \lambda_2$ , such that  $\mathbf{n}_1$  and  $\mathbf{n}_2$  signify the direction of stretch and compression, respectively;  $\mathbf{n}_1$  and  $\mathbf{n}_2$  are orthogonal. Figure 2i–l shows the evolution of the norm of the strain tensor  $\epsilon = ||\boldsymbol{\epsilon}||$ . The strain ( $\epsilon$ ) at the jamming front is relatively constant throughout an experiment (Rømcke et al 2021) and measured to be  $\sim 0.14$  in the case presented here. In the current work, we will focus on the orientation of the eigenvectors. Though the strain field is relatively homogeneous by the end of an experimental run (Fig. 2l), the superimposed eigenvectors show that the direction in which the suspension is stretched and compressed depends on the location in the flow.

Finally, a time series of the texture experiment is presented in Fig. 2m–p. Due to the specific lighting conditions explained above, this experiment reveals features not visible in the PIV particle images. Two key observations form the scope of this work. First, like the velocity field, there is a sharp transition between the regions with and without surface structures. This transition propagates from the cylinder, into the suspension, leaving a textured surface in its wake. We observe a change from a reflective to a matte surface indicative of a dilated suspension (Brown and Jaeger 2012; Maharjan et al 2021; Bischoff White et al 2010; Smith et al 2010). Second, by comparing the eigenvectors of the strain tensor (Fig. 2i–l) and the orientation of the surface features (Fig. 2m–p), there appears to be a connection. More specifically, the eigenvectors and surface features appear to be oriented in the same direction at the same locations in the flow, suggesting the raw surface images may hold quantifiable information akin to the PIV. This is explored further below.

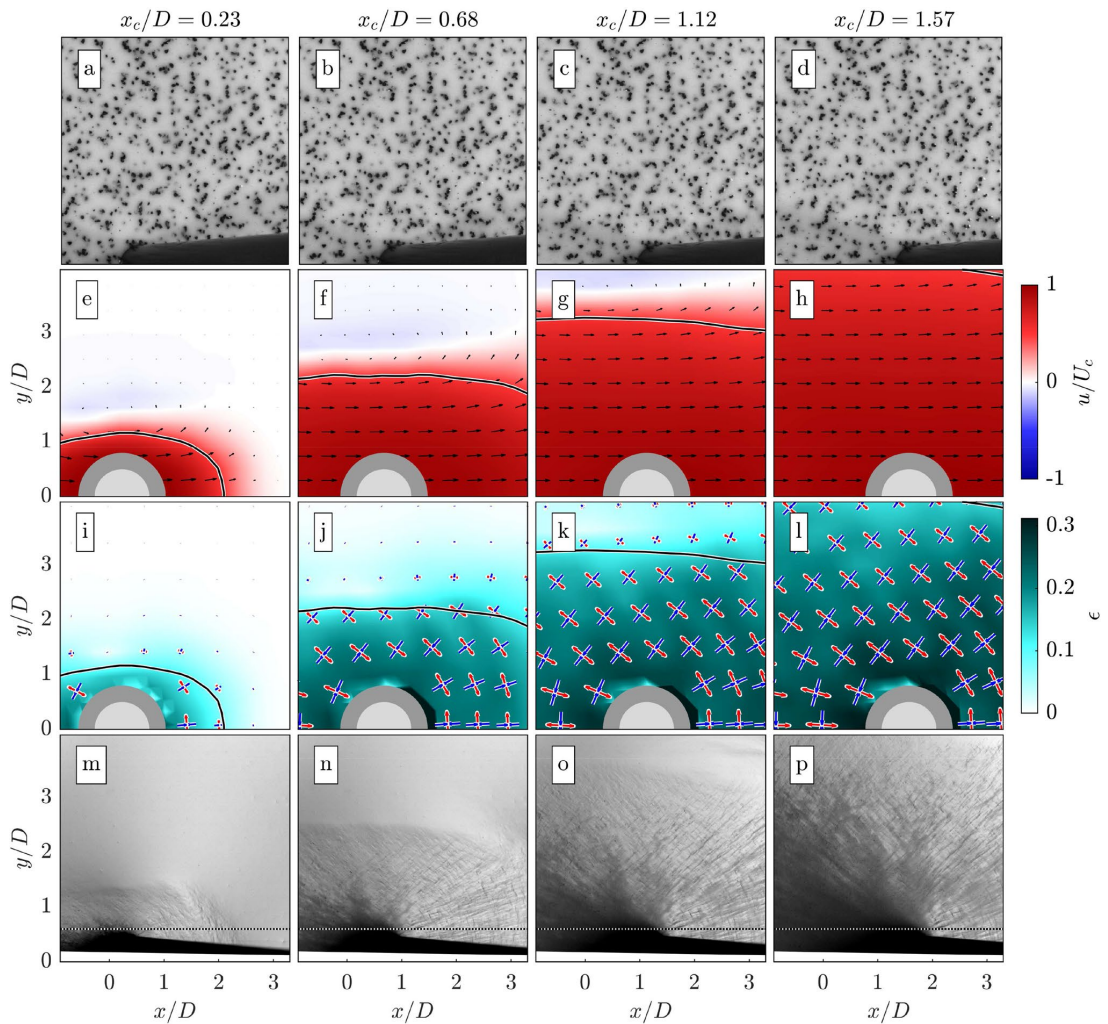


**Fig. 2** Time series comparison between PIV and texture images.  $x_c$  represents the location of the cylinder. **a–d** Raw PIV particle images. **e–h** Resulting PIV velocity fields with superimposed velocity vectors. **i–l** Accumulated strain ( $\epsilon$ ) with superimposed eigenvectors. Red represents the direction of stretch ( $\mathbf{n}_1$ ), while blue indicates the direc-

tion of compression ( $\mathbf{n}_2$ ). For clarity,  $\mathbf{n}_1$  are scaled with  $\epsilon$ . In **e–l**, the jamming front ( $0.5U_c$  contour) is represented by the black line. **m–p** Surface features as the front propagates. In order to avoid the cylinder shadow, the analysis is restricted to the region above the dotted line

### 3 Analysis methodology

The aim of this study is to quantify the structures observed at the free surface of a dense suspension undergoing dynamic jamming. In this section, we present a method that is able to identify surface features and their orientation. In short, images of the free surface are divided into interrogation windows, and the 2D fast Fourier transform (FFT) of the local windows is used as a basis for quantifying these structures,

which is presented in Sect. 3.1. Section 3.2 establishes a basis by which this process can be optimized and determines the optimal parameter values used in the remainder of this work.

#### 3.1 FFT and sector averaging

Here, in order to extract local information from the texture images, such as how dominant the features are and what

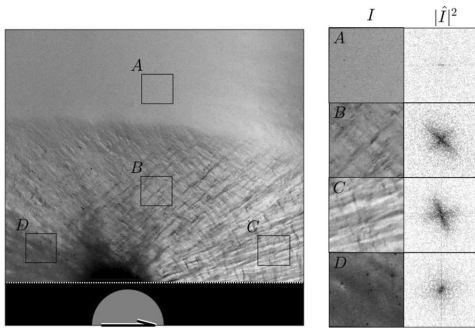


**Fig. 3** A snapshot of the suspension surface. Example interrogation windows are presented in the right columns with both the pixel intensity ( $I$ ) and the 2D power spectra ( $|\hat{I}|^2$ ). The intensity scale of the power spectra is plotted logarithmically.  $200 \times 200$  pixel interrogation windows representing A no features, B and C distinct features, D weak features

orientation they have, we divide the frame into interrogation windows. Figure 3 gives examples of four representative windows, which we will focus on in this section. As a first step toward quantifying the surface features, we take a 2D FFT of each window ( $I(i, j) \rightarrow \hat{I}(k_i, k_j)$ ); using an FFT to gain information on the surface texture is a common practice for interfacial flows, e.g., (Zhang 1996; Loimer et al 2002; Timberlake and Morris 2005; Singh et al 2006). The mean pixel intensity of the interrogation window is subtracted before calculating the FFT. Here,  $I$  and  $\hat{I}$  represent the intensity in the image and wave number domain, respectively.

The resulting FFTs of the interrogation windows are seen in the right column of Fig. 3 represented here by the power spectral density  $|\hat{I}|^2$ . Notice how the streaks in the interrogation windows are reflected in the corresponding power spectra. For B and C, the power spectra show clear features orthogonal to the streaks observed in the image. This trend is also observed for D, though clustered at lower wave numbers. Window A, however, has an almost perfectly homogeneous intensity, which is reflected in the power spectrum by predominantly exhibiting values at the noise level. An unwanted feature is also revealed by the FFT. As seen in the power spectra of A and D, a signal is observed along the lines  $k_i = 0$  and  $k_j = 0$ . Though the background subtraction removes most of these features, they are still significant for low signal-to-noise ratio regions, e.g., A and D. For any further processing, this issue is addressed by masking out the values at the lines  $k_i = 0$  and  $k_j = 0$ .

The general shape of the power spectra encodes both how dominant the features are and in what direction they are oriented. We extract the shape of a power spectrum by taking a sectional average. First, we denote the wave vector  $\mathbf{k} = (k_i, k_j)$ , so that in polar coordinates,  $k = |\mathbf{k}|$  with the angle

$\theta = \tan^{-1}(k_j/k_i)$ . The averaging procedure is taken over the wave number  $k$  ranging from 0 to  $0.5 \text{ pixel}^{-1}$  in sectors of size  $\Delta\theta$ . In polar coordinates, the average over a sector is represented by the integral

$$f(\theta, \Delta\theta) = \frac{8}{\Delta\theta} \int_0^{1/2} \int_{\theta-\Delta\theta/2}^{\theta+\Delta\theta/2} |\hat{I}|^2(k, \theta) k \, d\theta \, dk. \quad (3)$$

Numerically, given the discrete values of  $|\hat{I}|^2$ , the circle is divided into a number ( $N$ ) of equally spaced angular sectors with a relative overlap  $\xi$ , shown schematically in Fig. 4a. Note that  $\Delta\theta = 2\pi/(N(1 - \xi))$ . The sector average is calculated as the mean of  $|\hat{I}|^2$  contained within the sector. Figure 4b and c show how the trend in the power spectra is reflected in the resulting curve  $f$ .

We use the sector average curve,  $f$ , to extract key features of a power spectrum. First, we calculate the shape factor,  $S$ , of the sector average curve in order to distinguish between an interrogation window with and without surface structure.  $S$  is a measure of how much a shape resembles a circle. The shape factor is defined such that it compares the perimeter ( $\delta$ ) of  $f$  with the circumference of a circle with the same area ( $\alpha$ ) as  $f$ , i.e.,

$$S = \frac{2\sqrt{\pi}\sqrt{\alpha}}{\delta}. \quad (4)$$

The shape factor  $S$  is in the range 0 to 1, where 1 represents a perfect circle. The power spectrum of window A from Fig. 3 is relatively uniform and is expected to show values of  $S$  close to unity. This can also be seen by substituting in a constant value for  $|\hat{I}|^2$  in (4) resulting in  $f(\theta) = \text{constant}$ . Window C, on the other hand, is expected to show values distinguishable from a perfect circle as we observe clear angular dependencies. Secondly, we take the orientation of the peak of  $f$  to represent the orientation of the dominant surface features. In the image coordinates ( $i, j$ ), we denote the orientation of the peak  $\theta_p^*$  which defines the unit

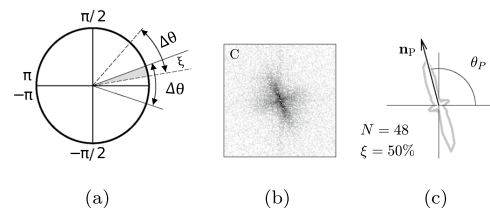


**Fig. 4** Schematics of the sector averaging. **a** Two neighbouring sectors with overlap. **b** Power spectra of interrogation window C with **c** resulting sector average curve ( $f$ ) calculated with  $N = 48$  sectors and  $\xi = 50\%$  overlap. The vector  $\mathbf{n}_p$  and the angle  $\theta_p$  represent the orientation of the peak

vector  $\mathbf{n}_p^* = (\cos \theta_p^*, \sin \theta_p^*)$ . The unit vector is mapped to the spatial coordinate system with the calibration, such that  $\mathbf{n}_p = (\cos(\theta_p), \sin(\theta_p))$ , where  $\theta_p$  represents the orientation of the peak in the  $(x, y)$ -system. Note that the Fourier transform is symmetric about the origin, thus two equal sized peaks separated by an angle  $\pi$  are observed in Fig. 4c. As a representation of the main direction of the structures, we only focus on peaks in the upper half plane  $0 \leq \theta_p < \pi$ .

### 3.2 Determining processing parameters

Some parameters have been presented in the previous section that affect the sector average curve  $f$ . Here, we focus on the size of the interrogation window, as well as the number of sectors ( $N$ ) and the sector overlap ( $\xi$ ). Adjusting these parameters will consequently have an impact on  $S$  and  $\theta_p$ . As one of our aims is to be able to distinguish between regions with surface features (such as window C) from regions without surface features (such as window A), we choose to use a set of processing parameters that will maximize the difference in  $S$  between these two scenarios.

Trends of  $S$  for window A and C over a range of processing parameters ( $N$  and  $\xi$ ) are presented in Fig. 5. As expected, the sector average curve,  $f$ , for window A (Fig. 5a) takes on a circular shape, while for window C (Fig. 5b), the curve indicates clear peaks orthogonal to the streaks on the surface. This is also reflected by the values of  $S$  showing higher values for window A compared to C.

However, in the extreme cases, the difference in  $S$  tends to be small. For example, choosing a large number of sectors and a small overlap, even though the the resulting sector average curve from C shows clear peaks and a low shape factor, the shape factor of A is also reduced. On the other hand, choosing few sectors with a large overlap yields an almost perfect circular result for window A, but the peaks in C are no longer clear and the shape factor is higher. Figure 5 indicates that there is an optimal combination of  $N$  and  $\xi$  that would maximize the difference in shape factor  $S$ , such that the shape factor yields a clear distinction between the two scenarios.

We point out that the result presented in Fig. 5 only compares two locations in the flow (A and C) for one window size ( $256 \times 256$  pixels) from a specific snapshot of the flow. However, the trend is the same when comparing window A with window B and D over a range of window sizes from  $64 \times 64$  to  $512 \times 512$  pixels. After considering different window sizes and values for  $N$  and  $\xi$ , the overall difference in  $S$  appears to converge with increasing window size at  $256 \times 256$  pixels. Setting  $N = 128$  and  $\xi = 75\%$  gives a sufficiently large difference in  $S$ , while simultaneously ensuring a satisfactory angular resolution for establishing  $\theta_p$ . For the remainder of this work, we will use a window size of  $256 \times 256$  pixels, with  $N = 128$  and  $\xi = 75\%$  when computing the sector average curve,  $f$ . It would be important to note that the “optimal” is dependent on the specific experimental set-up and that the results found here would

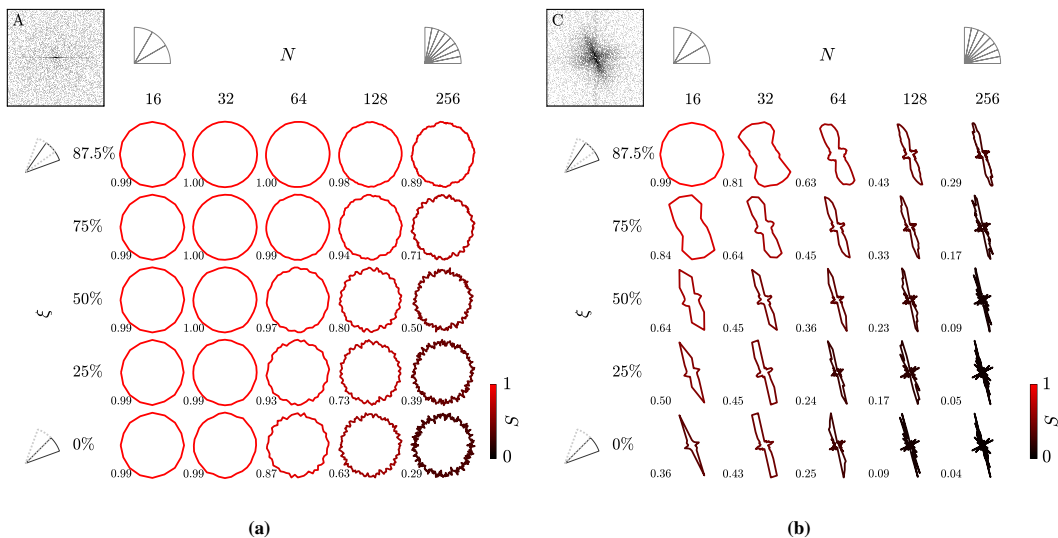


**Fig. 5** Sector average curves ( $f$ ) for  $256 \times 256$  pixels interrogation windows of **a** A and **b** C over a range of overlap ( $\xi$ ) and number of sectors ( $N$ ). The resulting shape factor ( $S$ ) is indicated by the

color scheme and also presented numerically for each curve. For the remainder of this work, we choose  $N = 128$  and  $\xi = 75\%$

not be universally optimal akin to how PIV processing parameters are optimized individually for each experiment.

### 4 Results

The method outlined in Sect. 3 is now applied to the full texture images. Section 4.1 presents results from the texture images alone. By setting a threshold value for  $S$ , we identify the textured region, and in Sect. 4.2, we give an estimate of how fast this region propagates into the suspension. In Sect. 4.3, the data extracted from analysing the texture images are directly compared to the PIV data. First, we present the combined evolution of the shape factor and velocity field. We then show that in certain regions of the flow, the direction of the texture and the eigenvectors of the strain tensor are predominantly oriented in the same direction.

#### 4.1 Quantifying the texture for the full field

From the method presented above, we are capable of identifying if the surface shows features ( $S$ ), and in what direction the features are oriented ( $\mathbf{n}_p$ ). Both  $S$  and  $\mathbf{n}_p$ , are presented in Fig. 6. The analysis is conducted on the full field of the time series shown in Fig. 2m–p, with the processing parameters found in Sect. 3.2. In addition, we let neighbouring interrogation windows overlap with 75%.

Figure 6a shows that the shape factor clearly separates the flow into two regions. Five iso-contours,  $S = 0.6, 0.7, 0.8, 0.85$  and  $S = 0.9$ , are superimposed on the  $S$ -field. Here, these contours tend to cluster at the transition between the textured and texture-free surface. Analogous to the  $0.5U_c$  contour being used to identify the position of the jamming front from PIV data, a contour level between  $S = 0.6$  and  $S = 0.9$  identifies the position of the front from the texture data. In the later stages of an experimental run, dilation renders the surface matte. Due to the increase in  $S$  observed

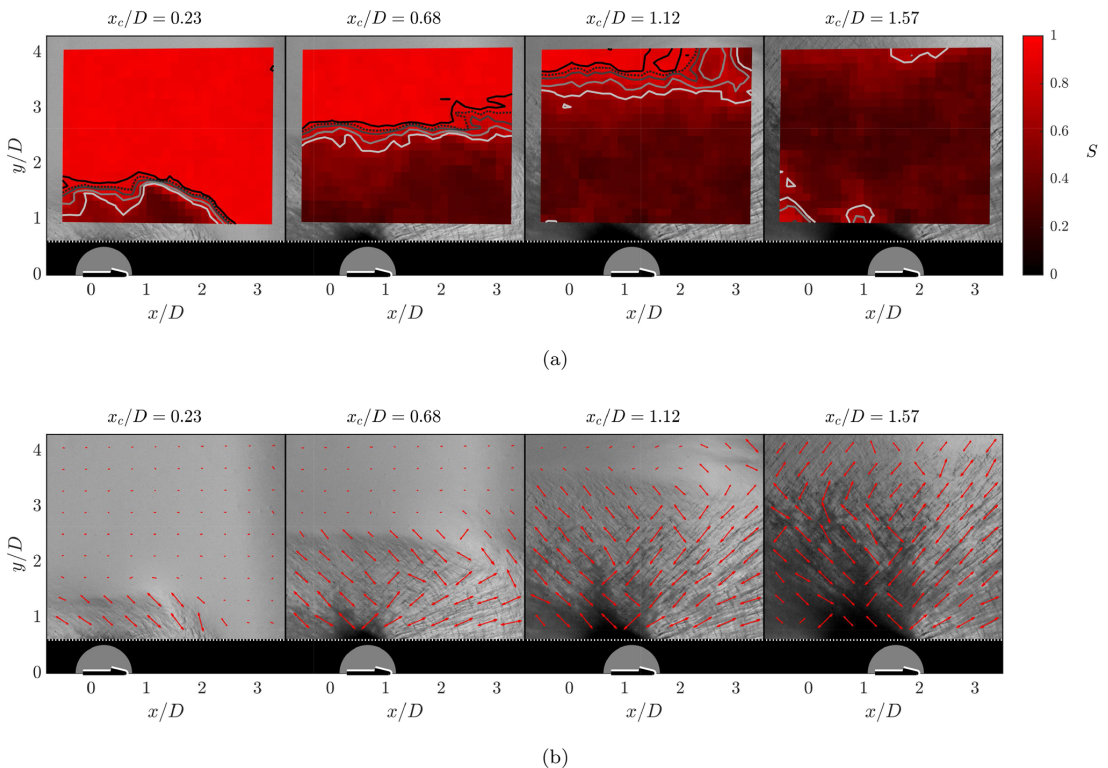


**Fig. 6** Texture analysis on the full field of the snapshots in Fig. 2m–p. **a** Shape factor  $S$ . The contours represent  $S = 0.6, 0.7, 0.8, 0.85$  and  $0.9$ , where the  $0.85$  is represented by the dotted line. **b** Orientation of the peak ( $\mathbf{n}_p$ ) from the sector average, which is represented by the

vectors superimposed on the corresponding surface image. Every third vector is plotted to reduce clutter, and scaled with  $1 - S$ . In addition,  $\mathbf{n}_p$  is rotated by  $\pi/2$  such that the vectors point in the same direction as the surface streaks rather than normal to them

in Fig. 6a, it becomes increasingly difficult to identify the preferred texture orientation in some parts of the flow. This is most noticeable in the wake of the cylinder.

The corresponding orientation of the surface features are indicated in Fig. 6b. As noted in Figs. 4 and 5, the peak in  $f$  is oriented normal to the direction of the dominant streaks in the texture image. For clarity in Fig. 6b, the vectors indicating the peak angle,  $\mathbf{n}_p$ , are rotated by  $\pi/2$  such that they are oriented parallel to the surface streaks. Here, we plot both  $\mathbf{n}_p$  and  $-\mathbf{n}_p$ , representing the symmetry of the power spectra.

The orientation of the vectors can be directly compared to the actual texture image. Notice that fore (aft) of the cylinder, the vectors generally tend to be forward (backward) leaning, reflecting the dominant streaks in the region. The region roughly around the same  $x$ -location as the cylinder, exhibits a crosshatch pattern (Chang et al 1990; Albrecht et al 1995). This is more clearly indicated in Fig. 3 by window B. As we only report the most dominant peak in  $f$ , the vectors  $\mathbf{n}_p$  generally show a mix of forward-leaning and backward-leaning in this region. Notice the similarity with the eigenvectors plotted in Fig. 2i–l;  $\mathbf{n}_1$ , representing direction of stretch, is backwards-leaning, while  $\mathbf{n}_2$ , representing compression, forward leaning. The similarity between  $\mathbf{n}_p$  and the strain eigenvectors will be addressed in greater detail in Sect. 4.3.

### 4.2 Propagation of the texture transition

Figure 7 establishes the location of the texture transition and estimates its propagation velocity into the suspension. Here, we focus on the transverse direction relative to the cylinder velocity. As with the jamming front position being identified by the  $0.5U_c$  contour, we will identify the texture transition by a contour value in  $S$ . We will compare how fast the jamming front and texture transition propagates into the suspension.

The front propagation factor, denoted here by  $\kappa$ , is defined as the relation between the speed of the jamming front and the speed of the perturbing body. In the transverse direction relative to the cylinder velocity, the front propagation factor is the time derivative of the jamming front’s  $y$ -position ( $y_f$ ) relative to the speed of the cylinder ( $U_c$ ). Since

$$\kappa = \frac{dy_f/dt}{U_c} \approx \frac{\Delta y_f/\Delta t}{\Delta x_c/\Delta t} = \frac{\Delta y_f}{\Delta x_c}, \tag{5}$$

rather than estimating a time derivative, we will focus on the equivalent relation  $\Delta y_f/\Delta x_c$ . As such, for the texture data, we start by establishing the position of the texture transition.

As seen by the superimposed contours in Fig. 6a, the position of the texture transition depends on the choice of contour level. Figure 7a shows vertical cross sections of the shape factor taken as the cylinder translate in the  $x$ -direction

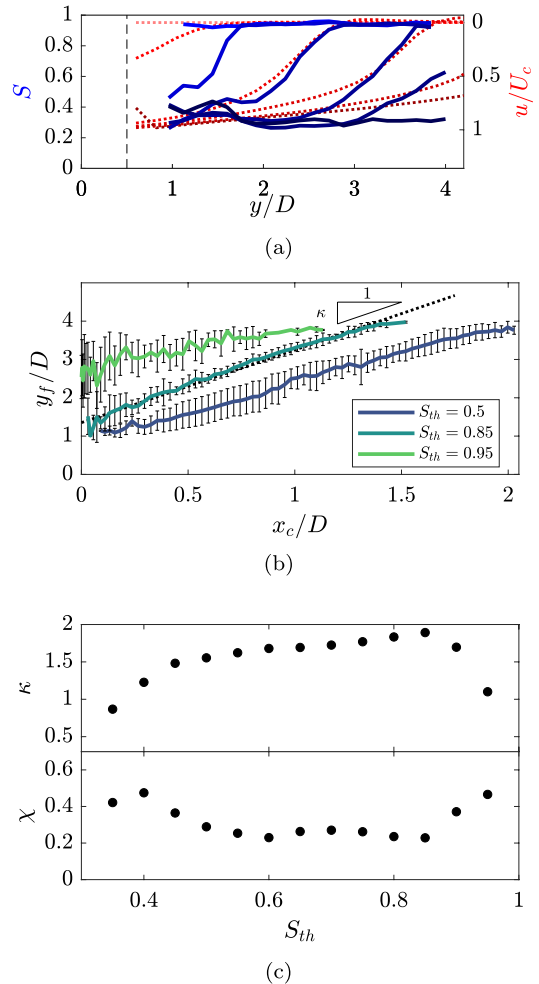


**Fig. 7** **a** Profiles of the shape factor (solid blue lines) and velocity (dotted red lines) for an experimental run in vertical cross sections taken at the location of the cylinder ( $x = x_c$ ). The black dashed line indicates the location of the cylinder surface. The color intensity indicates different  $x_c$  as the cylinder moves through the flow. Velocity profiles are flipped to emphasize the similarity between  $S$  and  $u$  **b** Position of the front,  $y_f$ , for three different threshold values of the shape factor. The slope of the linear regression line is denoted  $\kappa$ . **c** Slope,  $\kappa$ , and RMS of the error of the regression line,  $\chi$ , as functions of the threshold value,  $S_{th}$

( $S(x = x_c, y)$ , where  $x_c$  represents the instantaneous cylinder position). As with the velocity profiles (indicated by the dotted lines in Fig. 7a),  $S$  is not a perfect step, and as pointed out above, the position of the front will depend on the choice of the contour level. We use  $y_f$  to denote the position of the texture transition and is given implicitly from the shape factor profiles as  $S_{th} = S(x = x_c, y_f)$ . Here,  $S_{th}$  represents the

contour level, or the threshold value for  $S$  separating textured from texture free surface. Numerically, the front position is acquired by linearly interpolating the shape factor profiles, e.g., Fig. 7a.

The resulting front position ( $y_f$ ) from all experimental runs is plotted in Fig. 7b for three different values of  $S_{th}$ . Due to variation in the front position shown in Fig. 7b, calculating the relation  $\Delta y_f / \Delta x_c$  directly has large uncertainties associated with it. Instead, we report the slope of the linear regression line through the data, with the root mean square of the error denoted as  $\chi$ . Figure 7c shows  $\kappa$  and  $\chi$  as functions of  $S_{th}$ . The error tends to show a minimum in the range  $0.5 < S_{th} < 0.9$  with values  $\chi \approx 0.2$ . Note that this range of shape factor values are generally where we see the sharpest gradients in the  $S$ -profiles plotted in Fig. 7a and also indicated by the superimposed contours in Fig. 6a.

The minimum error is found at  $S_{th} = 0.85$  where the slope is  $\kappa = 1.89$ . From the velocity field, we measure a front propagation factor in the transverse direction as  $\kappa_{PIV} = 1.96 \pm 0.4$ . It should be noted that the speed estimated from the PIV is from the  $0.5U_c$  contour, which is itself a surrogate, albeit a commonly used one (Waitukaitis and Jaeger 2012; Peters and Jaeger 2014; Han et al 2016; Peters et al 2016; Majumdar et al 2017; Han et al 2018, 2019b; Baumgarten and Kamrin 2019; Römcke et al 2021). Thus, our method shows that the propagation of the texture transition and the propagation of the jamming front are comparable.

### 4.3 Comparing texture and PIV data for the full field

Similarities between the texture measurements and the PIV data have been noted in the previous sections. Here, we address the full field of view explicitly. Most notably, the evolution of the region exhibiting surface features (that is  $S < 0.85$  in Fig. 6a) and the region traversing with the cylinder (that is  $u/U_c > 0.5$  in Fig. 2e–h). In addition, it is observed that the surface features (Fig. 6b) and the eigenvectors of the strain tensor ( $\mathbf{n}_1$  and  $\mathbf{n}_2$  in Fig. 2i–l) are

approximately oriented in the same directions. This section aims to quantify these observations.

The combined evolution of the shape factor and velocity are plotted in Fig. 8. As indicated in Figs. 2 and 6a, the overall trend of the data is to transition from a state of low velocity ( $u/U_c < 0.5$ ) and high shape factor ( $S > 0.85$ ) to a state of high velocity ( $u/U_c > 0.5$ ) and low shape factor ( $S < 0.85$ ). In other words, the suspension transitions from a quiescent suspension with no notable surface features, to moving with the cylinder while exhibiting observable surface features. Importantly, Fig. 8 shows that the transition between these two states occurs at the same time in the experiment.

In addition, we seek to rigorously confirm that the surface features and eigenvectors are oriented in the same direction. This analysis is only relevant where the suspension has deformed sufficiently, and the surface exhibit clear surface features. As such, the data will be separated into regions where the analysis is conducted separately.

As a first step toward identifying the relevant region, Fig. 9a shows the histogram of  $S$  and  $u/U_c$  similar to Fig. 8 for the full time series and all experimental runs. By using the threshold value  $S_{th} = 0.85$  for the shape factor (see Sect. 4.2) and the definition of the jamming front ( $u/U_c = 0.5$ ), we divide the data into quadrants. Here,  $Q1$  represents a slow moving texture free state,  $Q2$  represents the transition, while  $Q3$  represents the suspension moving with the cylinder exhibiting measurable surface features. It is worth noting that  $Q1$ ,  $Q2$  and  $Q3$  contain roughly 35, 15 and 50% of the data, respectively. The unlabeled quadrant in Fig. 9a contains less than 1% of the data, and its contribution is negligible. An example of where these regions are located in the flow is presented in Fig. 9b. This figure compares the velocity field in Fig. 2f with the result of the shape factor  $S$  acquired from Fig. 2n.

A representation of the texture orientation and the strain eigenvectors are presented in Fig. 10a. The orientations are arbitrary, and the figure is only meant to be illustrative. The vectors are normalized to unit vectors.  $\mathbf{n}_p$  is defined in Sect. 3.1 and represents the orientation of the texture. As a

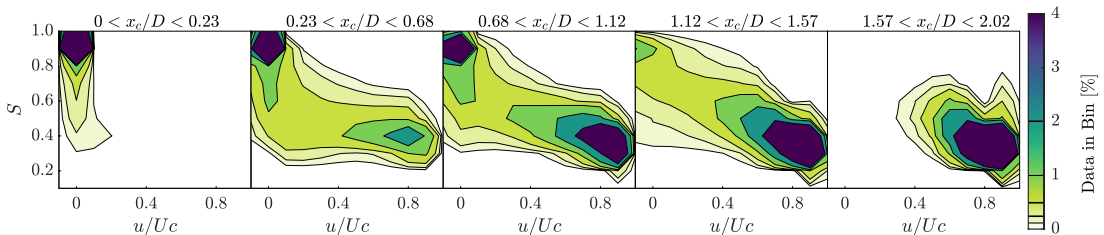


**Fig. 8** Evolution of the velocity,  $u$ , from the PIV experiment and shape factor,  $S$ , from the texture experiment. The figures are 2D histograms indicating where the data points tend to cluster for different stages in the experiment

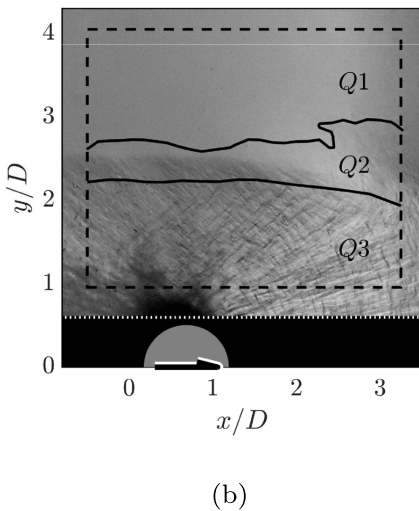
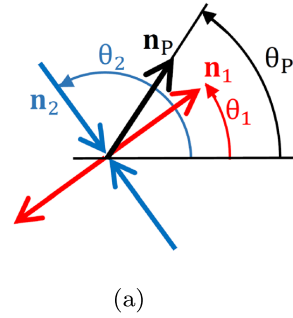
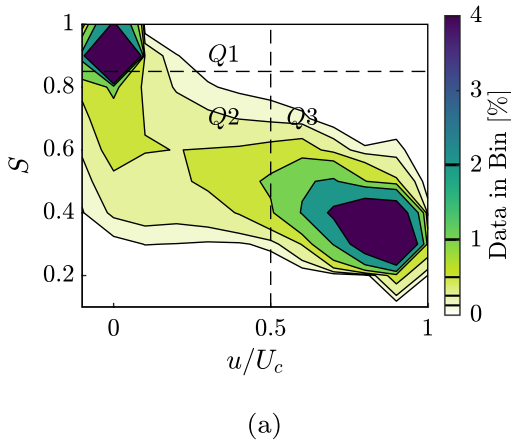


**Fig. 9** **a** Histogram of  $S$  and  $u/U_c$  similar to Fig. 8 for the whole time series for all experimental runs. The dashed lines separate the data into quadrants  $Q1$ ,  $Q2$  and  $Q3$ . **b** Example of how the quadrants represent different regions of the system. This particular snapshot compares the velocity field and texture from Fig. 2f to n

basis for comparing texture and eigenvector orientation, we will use the dot products  $\mathbf{n}_1 \cdot \mathbf{n}_p$  and  $\mathbf{n}_2 \cdot \mathbf{n}_p$ . Since all three vectors are unit vectors, these dot products represent the cosine of the angle separating them.

Figure 10b shows probability density functions (PDF) of  $\cos^{-1}(|\mathbf{n}_i \cdot \mathbf{n}_p|)$  for the regions  $Q1$ ,  $Q2$  and  $Q3$ , respectively. The absolute value of the dot product is used here, thus representing the angle separating  $\mathbf{n}_p$  and the span of the eigenvectors  $\mathbf{n}_i$  with a positive value. As a result,  $\cos^{-1}(|\mathbf{n}_i \cdot \mathbf{n}_p|) = 0$  indicates  $\mathbf{n}_p \parallel \mathbf{n}_i$ , while  $\cos^{-1}(|\mathbf{n}_i \cdot \mathbf{n}_p|) = \pi/2$  indicates  $\mathbf{n}_p \perp \mathbf{n}_i$ . As seen

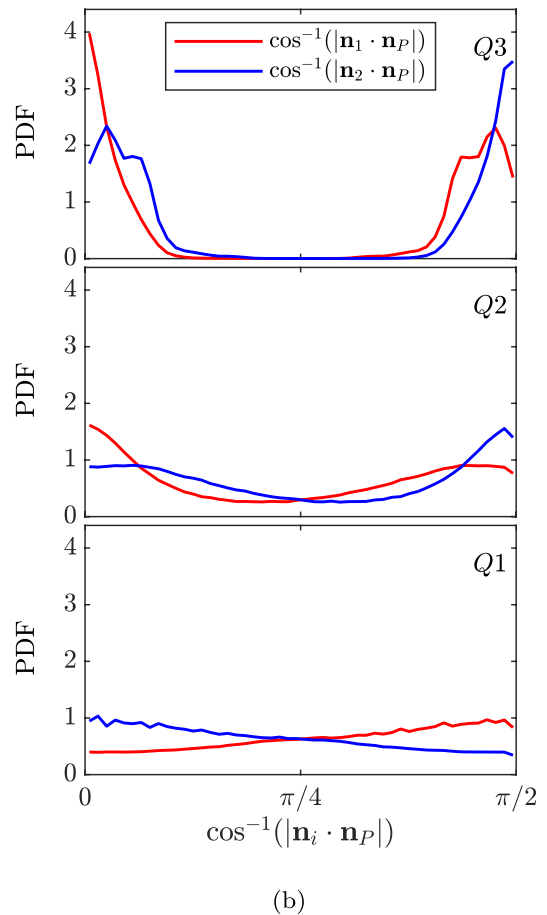


**Fig. 10** **a** Schematic representation of texture orientation,  $\mathbf{n}_p$ , and strain eigenvectors where  $\mathbf{n}_1$  represents stretch, and  $\mathbf{n}_2$  represents compression. **b** PDFs of the angle separating  $\mathbf{n}_p$  and  $\mathbf{n}_i$  for the regions  $Q1$ ,  $Q2$  and  $Q3$ , respectively



in Fig. 10b, the texture vectors are somewhat biased toward  $\mathbf{n}_2$  in the  $Q1$  region. In the transition region,  $Q2$ , the texture  $\mathbf{n}_p$  starts to favor the  $\parallel$  and  $\perp$  directions relative to the strain. For  $Q3$ , the PDFs are  $\approx 0$  in the region  $\pi/8 < \cos^{-1}(|\mathbf{n}_i \cdot \mathbf{n}_p|) < 3\pi/8$  with strong peaks at 0 and  $\pi/2$ . In other words, the PDFs from region  $Q3$  clearly show that the texture observed at the free surface has a strong connection with the orientation of the eigenvectors of the strain tensor.

## 5 Conclusion

Measurements of how surface texture evolves on a dense suspension of cornstarch and water with a freely propagating shear jamming front have been presented. The surface texture is captured by high-speed images of the free surface looking into a direct reflection. PIV measurements are used as a reference. From images of the surface texture, a 2D fast Fourier transform of local interrogation windows is used as a basis for analysing the surface structure. By taking a sector average of the power spectra, we are able to identify whether surface features are observed and the direction that they are oriented.

The PIV and texture measurements are two separate experiments, however, we show that the region of the suspension that shows clear surface features overlaps with the jammed region. In addition, we show that in the jammed, textured region of the flow, the eigenvectors of the strain tensor, and the observed surface features are oriented in the same direction. Hence, our analysis reveals that pictures of the free surface contain quantifiable information not previously directly accessed.

Dilation (Brown and Jaeger 2012; Jerome et al 2016; Majumdar et al 2017; Maharjan et al 2021) as well as surface corrugations (Loimer et al 2002; Timberlake and Morris 2005) have been observed at the free surface of dense suspensions before. However, few studies have investigated the surface texture at a freely propagating shear jamming front (Allen et al 2018). The results presented in the current work, particularly the relation between the eigenvectors of the strain tensor and the orientation of the surface features, will provide insight for future model development and understanding of dense suspensions as well as a valuable measurement tool for future investigations.

**Acknowledgements** RJH is funded by the Research Council of Norway through Project No. 288046. IRP acknowledges financial support from the Royal Society (Grant No. RG160089). Data supporting this study are openly available from the University of Southampton repository (<https://doi.org/10.5258/SOTON/D1973>).

**Funding** Open access funding provided by NTNU Norwegian University of Science and Technology (incl. St. Olavs Hospital - Trondheim University Hospital).

**Open Access** This article is licensed under a Creative Commons Attribution 4.0 International License, which permits use, sharing, adaptation, distribution and reproduction in any medium or format, as long as you give appropriate credit to the original author(s) and the source, provide a link to the Creative Commons licence, and indicate if changes were made. The images or other third party material in this article are included in the article's Creative Commons licence, unless indicated otherwise in a credit line to the material. If material is not included in the article's Creative Commons licence and your intended use is not permitted by statutory regulation or exceeds the permitted use, you will need to obtain permission directly from the copyright holder. To view a copy of this licence, visit <http://creativecommons.org/licenses/by/4.0/>.

## References

- Albrecht M, Christiansen S, Michler J, Dorsch W, Strunk HP, Hansson PO, Bauser E (1995) Surface ripples, crosshatch pattern, and dislocation formation: cooperating mechanisms in lattice mismatch relaxation. *Appl Phys Lett* 67(9):1232–1234. <https://doi.org/10.1063/1.115017>
- Allen B, Sokol B, Mukhopadhyay S, Maharjan R, Brown E (2018) System-spanning dynamically jammed region in response to impact of cornstarch and water suspensions. *Phys Rev E* 97(052):603. <https://doi.org/10.1103/PhysRevE.97.052603>
- Baumgarten AS, Kamrin K (2019) A general constitutive model for dense, fine-particle suspensions validated in many geometries. *Proc National Academy Sci* 116(42):20,828–20,836. <https://doi.org/10.1073/pnas.1908065116>
- Bischoff White EE, Chellamuthu M, Rothstein JP (2010) Extensional rheology of a shear-thickening cornstarch and water suspension. *Rheol Acta* 49(2):119–129
- Brown E, Jaeger HM (2012) The role of dilation and confining stresses in shear thickening of dense suspensions. *J Rheol* 56(4):875–923. <https://doi.org/10.1122/1.4709423>
- Brown E, Jaeger HM (2014) Shear thickening in concentrated suspensions: phenomenology, mechanisms and relations to jamming. *Reports Prog Phys* 77(4):046,602
- Cates ME, Wyart M (2014) Granulation and bistability in non-brownian suspensions. *Rheol Acta* 53(10):755–764
- Cates ME, Haw MD, Holmes CB (2005) Dilatancy, jamming, and the physics of granulation. *J Phys: Condens Matter* 17(24):S2517–S2531. <https://doi.org/10.1088/0953-8984/17/24/010>
- Chang KH, Gilbala R, Srolovitz DJ, Bhattacharya PK, Mansfield JF (1990) Crosshatched surface morphology in strained iii–v semiconductor films. *J Appl Phys* 67(9):4093–4098. <https://doi.org/10.1063/1.344968>
- Denn MM, Morris JF, Bonn D (2018) Shear thickening in concentrated suspensions of smooth spheres in Newtonian suspending fluids. *Soft Matter* 14:170–184. <https://doi.org/10.1039/C7SM00761B>
- Fernandez N, Mani R, Rinaldi D, Kadau D, Mosquet M, Lombois-Burger H, Cayer-Barrioz J, Herrmann HJ, Spencer ND, Isa L (2013) Microscopic mechanism for shear thickening of non-Brownian suspensions. *Phys Rev Lett* 111(108):301. <https://doi.org/10.1103/PhysRevLett.111.108301>
- Gadala-Maria F, Acrivos A (1980) Shear-induced structure in a concentrated suspension of solid spheres. *J Rheol* 24(6):799–814. <https://doi.org/10.1122/1.549584>
- Guazzelli E, Pouliquen O (2018) Rheology of dense granular suspensions. *J Fluid Mech* 852:P1. <https://doi.org/10.1017/jfm.2018.548>

- Guy BM, Hermes M, Poon WCK (2015) Towards a unified description of the rheology of hard-particle suspensions. *Phys Rev Lett* 115(088):304. <https://doi.org/10.1103/PhysRevLett.115.088304>
- Han E, Peters IR, Jaeger HM (2016) High-speed ultrasound imaging in dense suspensions reveals impact-activated solidification due to dynamic shear jamming. *Nature Commun* 7(1), <https://doi.org/10.1038/ncomms12243>
- Han E, Wyart M, Peters IR, Jaeger HM (2018) Shear fronts in shear-thickening suspensions. *Phys Rev Fluids* 3(073):301. <https://doi.org/10.1103/PhysRevFluids.3.073301>
- Han E, James NM, Jaeger HM (2019a) Stress controlled rheology of dense suspensions using transient flows. *Phys Rev Lett* 123(248):002. <https://doi.org/10.1103/PhysRevLett.123.248002>
- Han E, Zhao L, Van Ha N, Hsieh ST, Szydl DB, Jaeger HM (2019b) Dynamic jamming of dense suspensions under tilted impact. *Phys Rev Fluids* 4(063):304. <https://doi.org/10.1103/PhysRevFluids.4.063304>
- James NM, Han E, Cruz RAL, Jureller J, Jaeger HM (2018) Interparticle hydrogen bonding can elicit shear jamming in dense suspensions. *Nature Mater* 17. <https://doi.org/10.1038/s41563-018-0175-5>
- Jerome JJS, Vandenberghe N, Forterre Y (2016) Unifying impacts in granular matter from quicksand to cornstarch. *Phys Rev Lett* 117(098):003. <https://doi.org/10.1103/PhysRevLett.117.098003>
- Krieger IM (1972) Rheology of monodisperse latices. *Adv Coll Interface Sci* 3(2):111–136. [https://doi.org/10.1016/0001-8686\(72\)80001-0](https://doi.org/10.1016/0001-8686(72)80001-0)
- Kumar AA, Medhi BJ, Singh A (2016) Experimental investigation of interface deformation in free surface flow of concentrated suspensions. *Phys Fluids* 28(11):113,302. <https://doi.org/10.1063/1.4967739>
- Lin NYC, Guy BM, Hermes M, Ness C, Sun J, Poon WCK, Cohen I (2015) Hydrodynamic and contact contributions to continuous shear thickening in colloidal suspensions. *Phys Rev Lett* 115(228):304. <https://doi.org/10.1103/PhysRevLett.115.228304>
- Loimer T, Nir A, Semiat R (2002) Shear-induced corrugation of free interfaces in concentrated suspensions. *J Non-Newtonian Fluid Mech* 102(2):115–134. [https://doi.org/10.1016/S0377-0257\(01\)00173-2](https://doi.org/10.1016/S0377-0257(01)00173-2), <https://www.sciencedirect.com/science/article/pii/S0377025701001732>, a Collection of Papers Dedicated to Professor ANDREAS ACRIVOS on the Occasion of his Retirement from the Benjamin Levich Institute for Physicochemical Hydrodynamics and the City College of the CUNY
- Madraki Y, Hormozi S, Ovarlez G, Guazzelli E, Pouliquen O (2017) Enhancing shear thickening. *Phys Rev Fluids* 2(033):301. <https://doi.org/10.1103/PhysRevFluids.2.033301>
- Maharjan R, O'Reilly E, Postiglione T, Klimentko N, Brown E (2021) Relation between dilation and stress fluctuations in discontinuous shear thickening suspensions. *Phys Rev E* 103(012):603. <https://doi.org/10.1103/PhysRevE.103.012603>
- Majumdar S, Peters IR, Han E, Jaeger HM (2017) Dynamic shear jamming in dense granular suspensions under extension. *Phys Rev E* 95(012):603. <https://doi.org/10.1103/PhysRevE.95.012603>
- Mari R, Seto R, Morris JF, Denn MM (2014) Shear thickening, frictionless and frictional rheologies in non-Brownian suspensions. *J Rheol* 58(6):1693–1724. <https://doi.org/10.1122/1.4890747>
- Mukhopadhyay S, Allen B, Brown E (2018) Testing constitutive relations by running and walking on cornstarch and water suspensions. *Phys Rev E* 97(052):604. <https://doi.org/10.1103/PhysRevE.97.052604>
- Nemat-Nasser S (2004) *Plasticity : a treatise on finite deformation of heterogeneous inelastic materials*. Cambridge monographs on mechanics. Cambridge University Press, Cambridge
- Peters IR, Jaeger HM (2014) Quasi-2d dynamic jamming in cornstarch suspensions: visualization and force measurements. *Soft Matter* 10:6564–6570. <https://doi.org/10.1039/C4SM00864B>
- Peters IR, Majumdar S, Jaeger HM (2016) Direct observation of dynamic shear jamming in dense suspensions. *Nature* 532(7598):214–217. <http://search.proquest.com/docview/1781536995/>
- Römcke O, Peters IR, Hearst RJ (2021) Getting jammed in all directions: dynamic shear jamming around a cylinder towed through a dense suspension. *Phys Rev Fluids* 6(063):301. <https://doi.org/10.1103/PhysRevFluids.6.063301>
- Singh A, Nir A, Semiat R (2006) Free-surface flow of concentrated suspensions. *Int J Multiphase Flow* 32(7):775–790
- Singh A, Mari R, Denn MM, Morris JF (2018) A constitutive model for simple shear of dense frictional suspensions. *J Rheol* 62(2):457–468. <https://doi.org/10.1122/1.4999237>
- Sivadasan V, Lorenz E, Hoekstra AG, Bonn D (2019) Shear thickening of dense suspensions: The role of friction. *Physics of Fluids* 31(10):103,103. <https://doi.org/10.1063/1.5121536>
- Smith M, Besseling R, Cates M, Bertola V (2010) Dilatancy in the flow and fracture of stretched colloidal suspensions. *Nature Commun* 114. <https://doi.org/10.1038/ncomms1119>
- Stickel JJ, Powell RL (2005) Fluid mechanics and rheology of dense suspensions. *Annu Rev Fluid Mech* 37(1):129–149. <https://doi.org/10.1146/annurev.fluid.36.050802.122132>
- Tapia F, Pouliquen O, Guazzelli E (2019) Influence of surface roughness on the rheology of immersed and dry frictional spheres. *Phys Rev Fluids* 4(104):302. <https://doi.org/10.1103/PhysRevFluids.4.104302>
- Timberlake BD, Morris JF (2005) Particle migration and free-surface topography in inclined plane flow of a suspension. *J Fluid Mech* 538:309–341. <https://doi.org/10.1017/S0022112005005471>
- Waitukaitis SR, Jaeger HM (2012) Impact-activated solidification of dense suspensions via dynamic jamming fronts. *Nature* 487(7406):205. <https://doi.org/10.1038/nature11187>
- Wyart M, Cates ME (2014) Discontinuous shear thickening without inertia in dense non-Brownian suspensions. *Phys Rev Lett* 112(098):302. <https://doi.org/10.1103/PhysRevLett.112.098302>
- Zhang X (1996) An algorithm for calculating water surface elevations from surface gradient image data. *Exp Fluids* 21(1):43–48

**Publisher's Note** Springer Nature remains neutral with regard to jurisdictional claims in published maps and institutional affiliations.



Article III

---

# **Collision of Dynamic Jamming Fronts in a Dense Suspension**




---

Olav Rømcke, Ivo R. Peters, R. Jason Hearst

*Published*  
*Physical Review Fluids*, **6**, 103301.



## Collision of dynamic jamming fronts in a dense suspension

Olav Rømcke <sup>1</sup>, Ivo R. Peters <sup>2</sup>, and R. Jason Hearst <sup>1,\*</sup>

<sup>1</sup>*Department of Energy and Process Engineering, Norwegian University of Science and Technology, NO-7491 Trondheim, Norway*

<sup>2</sup>*Faculty of Engineering and Physical Sciences, University of Southampton, Highfield, Southampton SO17 1BJ, United Kingdom*



(Received 21 April 2021; accepted 10 September 2021; published 21 October 2021)

Dynamic jamming is a phenomenon whereby a dense suspension switches from a fluidlike to a solidlike state when subjected to sufficient stress and deformation. Large enough systems show that this transition is accompanied by a distinct jamming front. We present an experimental study where two jamming fronts are created simultaneously using two cylinders moving in parallel. We focus our observations on the collision of the jammed regions when the two fronts meet. Surprisingly, our measurements, combining surface texture visualization and time-resolved particle image velocimetry, show the formation of an unjammed region contained within the otherwise jammed suspension.

DOI: [10.1103/PhysRevFluids.6.103301](https://doi.org/10.1103/PhysRevFluids.6.103301)

### I. INTRODUCTION

Densely packed suspensions of solid particles exhibit phenomena such as discontinuous shear thickening [1–3], a dilating particle structure [4], and the ability to jam [5–7], that is, a switch to a solidlike state. In some systems, the transition from a fluidlike to a solidlike state is observed to give rise to the phenomena of dynamic shear jamming fronts [8–14]. A region of high shear rate, initiated from a perturbing body, propagates through the suspension and leaves a jammed state in its wake. Although there has been recent progress in macroscale continuum modeling capturing dynamic shear jamming fronts [15,16], studies of this phenomenon have typically been limited to relatively simple flows and geometries. More specifically, previous experimental configurations generated jamming fronts from a single perturbing body, and thus the idea of jamming fronts interacting has not been previously investigated. What happens when jamming fronts collide is an open question.

A well-known example of a suspension capable of dynamic jamming is a mixture of cornstarch and water [11,17,18]. Such a suspension flows when subjected to low stress, but shear thickens or jams at high stress. Once the stress is released, the suspension relaxes back to a fluidlike state [4,7,19]. Physically, the underlying mechanism causing discontinuous shear thickening and dynamic jamming is understood as a transition from a viscous to frictional interaction between particles, which changes the effective jamming volume fraction and subsequently the viscosity at a given volume fraction [1,20,21]. Repulsive forces between particles establish an onset stress [22,23], below which the particles are separated by a lubrication layer. However, when the suspension is subjected to a sufficiently high stress, capable of overcoming the repulsive force, the particles are

---

\*jason.hearst@ntnu.no

*Published by the American Physical Society under the terms of the [Creative Commons Attribution 4.0 International](https://creativecommons.org/licenses/by/4.0/) license. Further distribution of this work must maintain attribution to the author(s) and the published article's title, journal citation, and DOI.*

brought into a friction-dominated contact network [1,24], which greatly increases the resistance to flow. It has been shown that particle surface chemistry [22], shape [25,26], and polydispersity [27] affect this behavior. The framework presented by Wyart and Cates [1] identifies that a dynamically jammed state is accessible in the range of volume fractions where flow is possible for viscous, but not for frictional, interactions [11,14,23].

A finite amount of strain as well as stress is required to build a frictional contact network capable of resisting flow [15,16]. As a consequence, large systems do not homogeneously turn into a jammed state, but transition locally once the suspension has strained sufficiently. This is observed as a front of high shear rate originating from the perturbing source that propagates through the suspension, leaving a jammed region in its wake [8–14]. The stress is applied by the local acceleration of the suspension [16], while an intrinsic onset strain is observed to accompany the liquid-solid transition [14,28], depending on volume fraction [9,12,16]. For cornstarch suspensions, this transient phenomenon has been observed in domains ranging from 30 mm [10] to 300 mm [13], where the transition into the jammed state can propagate unimpeded through the suspension before confinement effects from solid boundaries influence the behavior [4,7]. It is worth noting that the jamming front phenomenon has also been observed at a geological (kilometer) scale [29]. These examples are larger than typical millimeter-sized rheometer configurations, as it is necessary to have a domain large enough to observe the front propagation. In summary, dynamic shear jamming fronts are observed in large systems when the suspension has a high enough volume fraction and is subjected to a sufficient amount of stress and strain to establish a force bearing contact network.

As mentioned above, the local stress is an important factor in determining if the suspension jams. Though Han *et al.* [16] have demonstrated how the stress is related to the speed of the jamming front in the case of simple shear, we have no rigorous way of determining the local stresses in the general case. Instead, the dilating property of dense suspensions will be utilized here. Dilatancy is the ability of dense granular structures to increase in volume when sheared. In a suspension, the expansion of the solid phase causes a suction in the liquid phase [4,7,17,28,30]. This can be observed at the free surface as a change in surface texture from reflective to matte as the liquid phase is sucked into the voids in the expanding granular structure [25,31–33]. A connection between free-surface texture change, dilation, and jamming in dense suspensions has been previously observed [4,25,28,30,31,33], even showing solidlike behavior such as cracking [32–35], followed by a relaxation back to a fluidlike state [33,34]. This visual change has also been shown to correlate with the stress response [4,31]. Thus, observing the surface texture directly can be a means of characterizing different regions of the flow that do not appear obvious from velocity field data alone.

While earlier studies on dynamic shear jamming fronts have been limited to a single propagating front and its interaction with a solid boundary, this study presents observations of colliding jamming fronts. The jamming fronts are generated by two cylinders moving in parallel. We show that after collision, a diamond-shaped region between the cylinders is formed that relaxes back to its quiescent state, while still being surrounded by jammed material.

## II. EXPERIMENTAL PROCEDURE

Our experimental setup, shown in Fig. 1, is similar to that described in Ref. [14]. Experiments were conducted in a 1 m × 0.5 m tank with two 25-mm-diameter ( $D$ ) cylinders submerged into a 15-mm-thick suspension consisting of cornstarch and a sucrose-water solution. The suspension floated atop a 15-mm layer of Fluorinert (FC-74). Fluorinert is a high-density ( $\rho = 1.8$  g/ml), low-viscosity ( $\nu = 0.75$  cSt) oil. This results in a close to stress-free bottom boundary, such that the jamming front propagates in a two-dimensional (2D) manner [12–14]. Microscopically, the jamming mechanism is fully three dimensional as the suspension layer thickness used in these experiments is several orders of magnitude larger than the particle size. However, macroscopically, the jamming front propagation is approximately 2D in the suspension layer [12–14]. Earlier laboratory scale observations of the jamming front phenomenon have been observed in domains

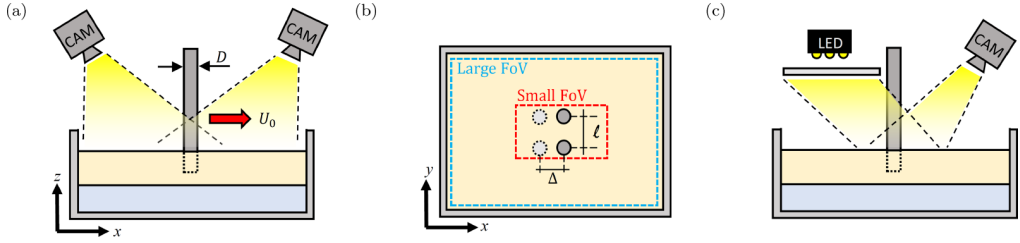


FIG. 1. Schematic of the experimental configuration. (a) PIV setup with cylinder diameter ( $D$ ) and direction and speed of travel ( $U_0$ ) indicated. (b) The top view shows the two cylinders moving in parallel. The PIV fields of view are also indicated along with the cylinder position ( $\Delta$ ) and separation ( $\ell$ ). (c) Surface texture imaging configuration. The two side views (a) and (c) show the suspension floating on a layer of Fluorinert.

up to  $\sim 300$  mm [13]. The present configuration is more than three times larger than this, making it one of the physically largest laboratory scale experiments targeted at measuring shear jamming fronts, in order to reduce confinement effects.

The cylinder velocity ( $U_0$ ) and the volume fraction ( $\phi$ ) are chosen to ensure that we reach the dynamic shear jamming regime. The volume fraction is defined as

$$\phi = \frac{(1 - \beta)m_s/\rho_s}{(1 - \beta)m_s/\rho_s + m_l/\rho_l + \beta m_s/\rho_w}, \quad (1)$$

where  $m_s$  and  $m_l$  are the starch and suspending fluid mass, respectively.  $\rho_s = 1.63$  g/ml and  $\rho_w = 1.00$  g/ml are the starch and water densities, respectively. The suspending liquid is a 50 wt % sucrose solution with density  $\rho_l = 1.23$  g/ml and viscosity  $\eta_0 = 0.016$  Pa s. The sucrose is added to the water in order to reduce the impact of settling [14]. Due to the difficulty in precisely determining the nominal value of the volume fraction of cornstarch suspensions, earlier studies have used measured quantities such as onset strain rate [19] or front propagation [13] as the control parameter rather than the volume fraction. We use the same approach here, as the behavior was highly consistent within a batch of suspension. The discrepancy in the volume fractions was accounted for by a 2% variation in the starch water content  $\beta$  and was nominally  $9\% \leq \beta \leq 11\%$ . Thus, the  $\phi$  reported here reflects the trend in the front propagation. At sufficiently low  $U_0$  no propagating jamming front is observed [9,14]. At sufficiently high perturbing speeds or stresses, yielding and buckling of the suspension have been reported [13,16]. The results presented here are for  $U_0 = 0.14$  m/s where the suspension is known to jam and the front propagation factor is independent of the  $U_0$  [14]. Ancillary tests at  $U_0 = 0.11$  and  $0.18$  m/s confirm this.

The suspension is mixed for a minimum of 2 h before it is poured onto the Fluorinert in the tank. It is then presheared before any measurements are performed. The surface is seeded with black pepper and for every batch, the measurements are repeated 12 times. The time from when the suspension is poured until the experiment is complete and the suspension is discarded is approximately 15 min, which results in an estimated settling distance on the order of the particle diameter, and is thus negligible [36,37]. Two high-speed cameras (Photron FASTCAM Mini WX100) view the suspension surface in front and behind the traversing cylinders [Fig. 1(a)]. Particle image velocimetry (PIV) is used to convert the image series to velocity fields with LaVision DaVis 8.4.0. An initial pass was performed with  $96 \text{ pixels} \times 96 \text{ pixels}$  square interrogation windows, followed by two passes with circular interrogation windows with decreasing size ending at  $48 \text{ pixels} \times 48 \text{ pixels}$ . For all passes, the interrogation windows have a 50% overlap. The final velocity fields are made up of the two fields, one from each camera, stitched together, to provide a complete view around the cylinders. PIV measurements were conducted at two magnifications using different lenses. A 50-mm lens was used to image the entire flow field around the pair of cylinders, and in a separate experiment a 180-mm lens was used to specifically focus on the area between the two cylinders. The resulting PIV fields of view are represented schematically in Fig. 1(b).



Only minor adjustments to the setup were needed to enhance the visibility of the surface texture. The surface texture measurement campaign was performed in order to provide a second method for identifying jammed regions in the flow. Here, a light-emitting diode (LED) array covered by a semitransparent acrylic sheet served as the light source. The camera was positioned such that it captured the direct reflection of the light source in the suspension surface [31]. A rough surface, caused by dilation, diffuses the light reflected off the suspension surface and thus changes the observed intensity. As such a matte surface indicates that the suspension is jammed while a reflective surface indicates that the suspension is in a quiescent unjammed state [4,7,30,31]. The size of the acrylic sheet ensured that the reflection in the suspension surface covered the field of view of the camera [Fig. 1(c)]. In order to get as clear a view of the surface as possible, we did not seed the sample with tracer particles for this experiment.

### III. RESULTS

Both the cylinders and the suspension start at rest. The cylinders are initially located at  $x = 0$ . Once cylinder movement is initiated, large velocity gradients are observed at the surface of each cylinder, which propagate into the surrounding suspension. At some point, depending on the speed of the front and the distance between the cylinders  $\ell$ , the fronts collide. By the end of an experimental run, the region between the two cylinders moves at approximately the perturbing speed. In addition to the velocity field ( $\mathbf{u}$ ), we also present the strain rate magnitude ( $\dot{\gamma}$ ) and the accumulated strain ( $\epsilon$ ). The strain rate magnitude is calculated as

$$\dot{\gamma} = \sqrt{2\mathcal{D}_{ij}\mathcal{D}_{ij}}, \quad \text{where} \quad \mathcal{D}_{ij} = \frac{1}{2} \left( \frac{\partial u_i}{\partial x_j} + \frac{\partial u_j}{\partial x_i} \right). \quad (2)$$

The accumulated strain ( $\epsilon$ ) is calculated as the norm of the Eulerian logarithmic strain tensor [14,38]. This is estimated from the velocity field by first calculating the movement of the material points as  $\mathbf{x}_p(\mathbf{X}, t) = \mathbf{X} + \int_0^t \mathbf{u}(\mathbf{x}_p(\tau), \tau) d\tau$ , from which the deformation gradient tensor is acquired as  $\mathbf{F} = \partial \mathbf{x}_p / \partial \mathbf{X}$ . Here,  $\mathbf{X}$  is the position of the material points at  $t = 0$ . A polar decomposition of the deformation gradient ( $\mathbf{F} = \mathbf{V}\mathbf{R}$ ) gives the left stretch tensor  $\mathbf{V}$ , which has eigenvalues and eigenvectors,  $\lambda_i$  and  $\mathbf{n}_i$ , respectively. The strain tensor has the spectral representation [38]

$$\mathbf{e} = \sum_i \ln(\lambda_i) \mathbf{n}_i \otimes \mathbf{n}_i, \quad (3)$$

where we order eigenvalues  $\lambda_1 > \lambda_2$ , such that the direction of stretch and compression is denoted  $\mathbf{n}_1$  and  $\mathbf{n}_2$ , respectively.  $\mathbf{n}_1$  and  $\mathbf{n}_2$  are orthogonal. The norm of the strain tensor  $\epsilon = \|\mathbf{e}\|$  is used as a scalar measure of the accumulated strain.

PIV results are presented in Fig. 2 which shows both the large and small fields of view at  $\Delta/D = 1.87$ , which is close to the end of an experimental run. In particular we look at different cylinder separations ( $\ell$ ) with the single cylinder case as a reference. The velocity vectors are plotted in Figs. 2(a)–2(d), and the  $0.5U_0$  contour, typically used to identify the jamming front [8–13,16], is indicated by the black line in all fields. Some aspects of the system behavior are independent of both the number of cylinders and their separation. Relative to the perturbing body, the front has propagated twice as fast in the longitudinal direction compared to the transverse direction. This 1:2 propagation relationship is a direct consequence of an underlying onset strain [9,14], and does not change by introducing a second cylinder. A notable difference with the reference case, however, occurs in the collision region between the two cylinders. A uniform velocity field has been used in previous studies to indicate the jammed region [9,13]. Here, the velocity fields in Figs. 2(b)–2(d) [seen in more detail in Figs. 3(c)–3(e)] might suggest a uniformly jammed suspension after the fronts have collided. Though the velocity is relatively uniform, the strain rate magnitude ( $\dot{\gamma}$ ) in Figs. 2(j)–2(l) shows traces of a diamond-like structure in the collision region. The accumulated strain ( $\epsilon$ ) reveals a slightly different picture. As seen in Figs. 2(f)–2(h),  $\epsilon$  indicates the presence of a slit of material that has not sufficiently deformed to transition into the jammed

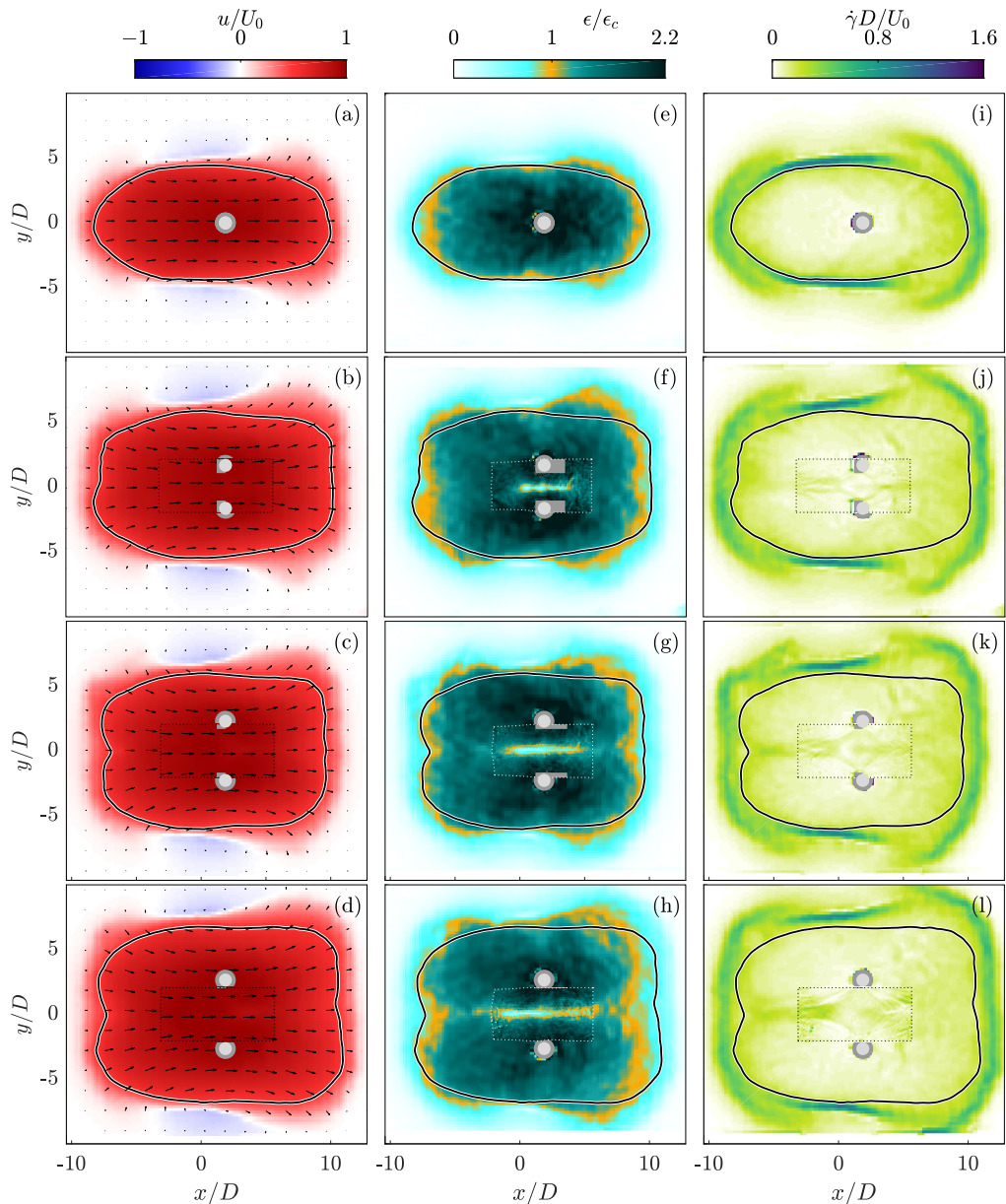


FIG. 2. Snapshots of the flow field at  $\Delta/D = 1.87$  and  $\phi = 0.36$  for several cylinder separations. From top to bottom  $\ell/D = 0, 3.3, 4.5,$  and  $5.3$ . Results from the small field of view are placed as an overlay in the center region indicated by the dotted border. The cylinders are moving from left to right. (a)–(d) Velocity ( $u$ ) with velocity vectors, indicating that the suspension is moving with the cylinder(s). (e)–(h) Accumulated strain ( $\epsilon$ ). The accumulated strain is normalized by the onset strain ( $\epsilon_c$ ) accompanying the jamming front found to be  $0.14 \pm 0.03$  from the single cylinder reference case at this specific volume fraction. (i)–(l) Strain rate magnitude ( $\dot{\gamma}$ ). The light gray circles identify the cylinders. Dark gray regions cover the region obstructed from view by the cylinders themselves. For the accumulated strain, the impacted region is larger because we are unable to track the full deformation history due to the obstructions to the field of view. An animated version is available in the Supplemental Material [39].

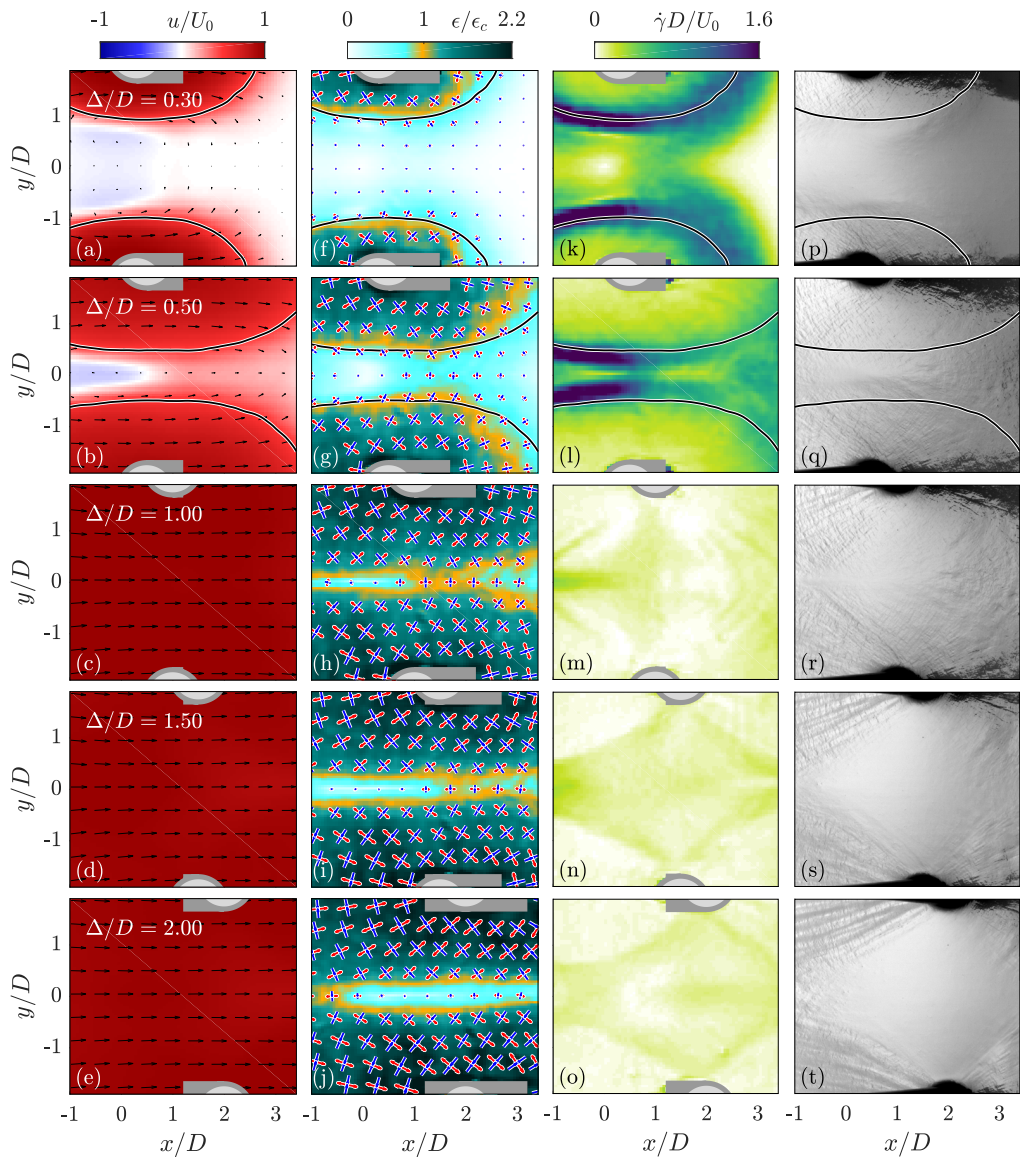


FIG. 3. Snapshots of the colliding jamming fronts for  $\ell/D = 4.5$  and  $\phi = 0.36$ . The rows show different displacement of the cylinders,  $\Delta/D$ . (a)–(e) are the velocity fields. (f)–(j) are the accumulated strain  $\epsilon$ , with superimposed eigenvectors,  $\mathbf{n}_1$  (red) and  $\mathbf{n}_2$  (blue), from Eq. (3). (k)–(o) are the strain rate  $\dot{\gamma}$  from Eq. (2). (p)–(t) show the result of the surface texture experiment. The black line superimposed on all fields represents the  $0.5U_0$  contour from the PIV data, which is a surrogate for the jamming front. The contour lies outside of the presented fields for  $\Delta/D \geq 1.00$ . The masked regions are the same as in Fig. 2. An animated version is available in the Supplemental Material [39].

state. This suggests that there is a region between the two cylinders that is unjammed while the surrounding suspension is jammed.

Figure 3 compares PIV data with the high-speed imaging of the suspension surface texture. The texture measurements have no direct information about the velocity field. However, as the example

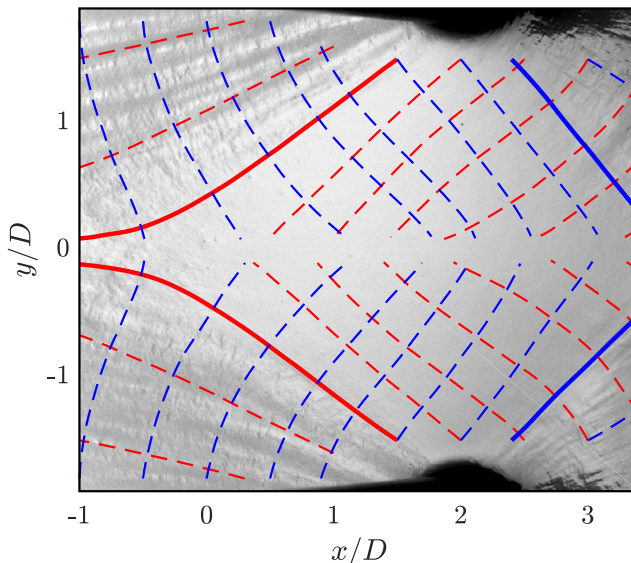


FIG. 4. Lines of principle strain superimposed on the texture image at  $\Delta/D = 2.00$ . Stretch ( $\mathbf{x}_1$ ) and compression ( $\mathbf{x}_2$ ) lines are represented by the red and blue lines, respectively. Here, we have emphasized the lines that roughly outline the unjammed region in the texture image.

shown here is at the same volume fraction, cylinder configuration, and speed, the  $0.5U_0$  contour from the PIV data is superimposed on both PIV and texture images. At later stages in an experimental run (here,  $\Delta/D \geq 1.00$ ), the contour lies outside of the field of view shown in Fig. 3. In the  $\dot{\gamma}$  fields it can be seen that the  $0.5U_0$  contour corresponds to a strong shear front propagating away from the cylinders as the flow evolves. After the two fronts collide, the suspension moves with the cylinders as indicated by the uniform velocity field [Figs. 3(c)–3(e)]. The accumulated stain [Figs. 3(f)–3(j)] shows the development of the undeformed slit. Interestingly, the region between the two cylinders is populated by a diamondlike shape visible in both the shear rate magnitude [Figs. 3(m)–3(o)] and the surface texture images [Figs. 3(r)–3(t)]. Based on the surface texture, we infer that the suspension between the cylinders, which appears to be reflective, has relaxed back to a quiescent, unstressed state, thus confirming that indeed the region between the cylinders is unjammed.

From previous studies where the front propagates freely through the suspension, it has been shown that the accumulated strain can be used to quantify when the suspension transitions into a solidlike state. However, in the collision region, the strain does not account for the subsequent relaxation of the suspension revealed by the texture images. As a consequence, there is a discrepancy between the shape of the unjammed region revealed by the accumulated strain and the texture images. Traces of the diamond shape observed in the texture image exist in the strain rate. This is presented in Fig. 3. Though the accumulated strain ( $\epsilon$ ) does not show a diamond shape as observed in the texture images, the eigenvectors of the strain tensor reveal an interesting feature. These eigenvectors seem to roughly align with the boundary of the diamond shape [see Figs. 3(f)–3(j)].

We further investigate the apparent discrepancy by plotting the lines of principle strain [14] superimposed on a texture image in Fig. 4. For an instantaneous strain field the principle strain lines are acquired numerically by solving  $d\mathbf{x}_1/d\sigma = \mathbf{n}_1$  for principle stretch and  $d\mathbf{x}_2/d\sigma = \mathbf{n}_2$  for principle compression, which ensures that the lines  $\mathbf{x}_1(\sigma)$  and  $\mathbf{x}_2(\sigma)$  are tangential to the eigenvectors  $\mathbf{n}_1$  and  $\mathbf{n}_2$ , respectively.  $\sigma$  is an arbitrary parametrization of the lines. Solving for  $\mathbf{x}_1$  and  $\mathbf{x}_2$  for multiple initial positions is presented in Fig. 4. We avoid the center slit when calculating  $\mathbf{x}_1$  and  $\mathbf{x}_2$ , as the accumulated strain is small in this region. Here, we have highlighted the lines that roughly correspond to the diamond shape revealed by the texture image. Note that in the fore half

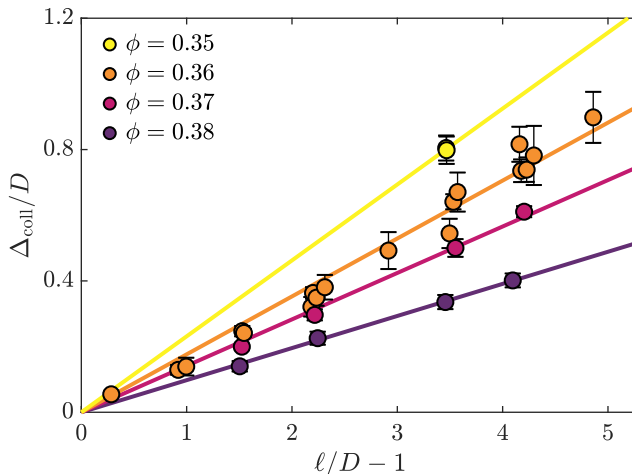


FIG. 5. Cylinder displacement at the time of front collision  $\Delta_{\text{coll}}/D$  compared to the effective surface-to-surface cylinder separation  $\ell/D - 1$ . Linear fits are meant only for reference.

plane, it is the compression line  $\mathbf{x}_2$  that outlines the diamond boundary, while in the aft half it is the stretch line  $\mathbf{x}_1$ .

As discussed in the Introduction, both the stress and the accumulated strain need to be sufficiently high to achieve (or remain in) a jammed state [15,16]. The slit in the center revealed by the accumulated strain never transitions into a jammed state as the strain level is not sufficiently high. The subsequent relaxation of the surrounding diamond shaped follows, as stresses are no longer transmitted through this region, revealed by the texture images.

Additional PIV measurements at different volume fractions within the dynamic jamming range confirm the same qualitative behavior. A slit of material between the two cylinders does not deform the amount expected for jamming to occur even though the velocity field appears uniform. With increasing volume fraction, the accumulated strain needed for the jamming transition to occur decreases, while the front propagates faster through the suspension [11–13]. This is summarized in Fig. 5 showing how the moment of collision of the jamming fronts varies with volume fraction ( $\phi$ ) and cylinder separation ( $\ell$ ). We define the collision as the event when the jamming front transitions from separate contours around each cylinder to one contour enveloping both cylinders. This is quantified by the distance the cylinder has traveled from its starting point to when collision occurs ( $\Delta_{\text{coll}}$ ). The lines are a guide for the eye, but a linear trend is evident. The points are expected to fall onto a straight line as long as the relation between front and cylinder movement is constant, which Fig. 5 confirms.

#### IV. CONCLUSIONS

We have presented observations of colliding jamming fronts. These fronts were generated by two cylinders moving in unison, and PIV has been used to calculate the velocity and deformation fields. The suspension between the cylinders moves uniformly after front collision. High-speed observations of the free-surface texture show that after collision a diamondlike region is formed between the cylinders which relaxes back to its quiescent, unjammed state. The accumulated strain does not portray this diamond-shaped region. However, we show that the edges of the diamond shape revealed by the texture images align with the direction of principle strain. We attribute this apparent discrepancy between the two approaches to the fact that the accumulated strain does not account for the relaxation of the suspension.

Although the region between the cylinders appears unjammed, there still must be a force-bearing structure connected to the two cylinders to drive the jamming front that continues to propagate through the suspension away from the bodies. This structure would effectively be protecting the region between the cylinders, allowing it to remain unjammed, and has a diamond shape in the present configuration. By utilizing a combination of PIV and surface texture measurements we have thus identified the phenomena associated with colliding jamming fronts. Surprisingly, our results reveal that colliding jamming fronts unjam a region between the perturbing bodies, providing another way geometry can be used to control where jamming occurs and where it does not.

Data supporting this study are openly available from the University of Southampton repository [40].

#### ACKNOWLEDGMENT

R.J.H. acknowledges the financial support of the Research Council of Norway (Grant No. 288046). I.R.P. acknowledges financial support from the Royal Society (Grant No. RG160089).

---

- [1] M. Wyart and M. E. Cates, Discontinuous Shear Thickening without Inertia in Dense Non-Brownian Suspensions, *Phys. Rev. Lett.* **112**, 098302 (2014).
- [2] H. A. Barnes, Shear-thickening (“dilatancy”) in suspensions of nonaggregating solid particles dispersed in Newtonian liquids, *J. Rheol.* **33**, 329 (1989).
- [3] R. Seto, R. Mari, J. F. Morris, and M. M. Denn, Discontinuous Shear Thickening of Frictional Hard-Sphere Suspensions, *Phys. Rev. Lett.* **111**, 218301 (2013).
- [4] E. Brown and H. M. Jaeger, The role of dilation and confining stresses in shear thickening of dense suspensions, *J. Rheol.* **56**, 875 (2012).
- [5] A. J. Liu and S. R. Nagel, Jamming is not just cool any more, *Nature (London)* **396**, 21 (1998).
- [6] A. J. Liu and S. R. Nagel, The jamming transition and the marginally jammed solid, *Annu. Rev. Condens. Matter Phys.* **1**, 347 (2010).
- [7] E. Brown and H. M. Jaeger, Shear thickening in concentrated suspensions: Phenomenology, mechanisms and relations to jamming, *Rep. Prog. Phys.* **77**, 046602 (2014).
- [8] S. R. Waitukaitis and H. M. Jaeger, Impact-activated solidification of dense suspensions via dynamic jamming fronts, *Nature (London)* **487**, 205 (2012).
- [9] E. Han, I. R. Peters, and H. M. Jaeger, High-speed ultrasound imaging in dense suspensions reveals impact-activated solidification due to dynamic shear jamming, *Nat. Commun.* **7**, 12243 (2016).
- [10] E. Han, L. Zhao, N. Van Ha, S. T. Hsieh, D. B. Szyld, and H. M. Jaeger, Dynamic jamming of dense suspensions under tilted impact, *Phys. Rev. Fluids* **4**, 063304 (2019).
- [11] I. R. Peters, S. Majumdar, and H. M. Jaeger, Direct observation of dynamic shear jamming in dense suspensions, *Nature (London)* **532**, 214 (2016).
- [12] E. Han, M. Wyart, I. R. Peters, and H. M. Jaeger, Shear fronts in shear-thickening suspensions, *Phys. Rev. Fluids* **3**, 073301 (2018).
- [13] I. R. Peters and H. M. Jaeger, Quasi-2D dynamic jamming in cornstarch suspensions: Visualization and force measurements, *Soft Matter* **10**, 6564 (2014).
- [14] O. Rømcke, I. R. Peters, and R. J. Hearst, Getting jammed in all directions: Dynamic shear jamming around a cylinder towed through a dense suspension, *Phys. Rev. Fluids* **6**, 063301 (2021).
- [15] A. S. Baumgarten and K. Kamrin, A general constitutive model for dense, fine-particle suspensions validated in many geometries, *Proc. Natl. Acad. Sci. USA* **116**, 20828 (2019).
- [16] E. Han, N. M. James, and H. M. Jaeger, Stress Controlled Rheology of Dense Suspensions using Transient Flows, *Phys. Rev. Lett.* **123**, 248002 (2019).
- [17] A. Fall, F. Bertrand, G. Ovarlez, and D. Bonn, Shear thickening of cornstarch suspensions, *J. Rheol.* **56**, 575 (2012).

- [18] M. Hermes, M. Guy, W. C. K. Poon, G. Poy, M. E. Cates, and M. Wyart, Unsteady flow and particle migration in dense, non-Brownian suspensions, *J. Rheol.* **60**, 905 (2016).
- [19] R. Maharjan and E. Brown, Giant deviation of a relaxation time from generalized Newtonian theory in discontinuous shear thickening suspensions, *Phys. Rev. Fluids* **2**, 123301 (2017).
- [20] R. Mari, R. Seto, J. F. Morris, and M. M. Denn, Shear thickening, frictionless and frictional rheologies in non-Brownian suspensions, *J. Rheol.* **58**, 1693 (2014).
- [21] Z. Pan, H. de Cagny, B. Weber, and D. Bonn, S-shaped flow curves of shear thickening suspensions: Direct observation of frictional rheology, *Phys. Rev. E* **92**, 032202 (2015).
- [22] N. M. James, E. Han, R. A. L. de la Cruz, J. Jureller, and H. M. Jaeger, Interparticle hydrogen bonding can elicit shear jamming in dense suspensions, *Nat. Mater.* **17**, 965 (2018).
- [23] B. M. Guy, M. Hermes, and W. C. K. Poon, Towards a Unified Description of the Rheology of Hard-Particle Suspensions, *Phys. Rev. Lett.* **115**, 088304 (2015).
- [24] A. Singh, R. Mari, M. M. Denn, and J. F. Morris, A constitutive model for simple shear of dense frictional suspensions, *J. Rheol.* **62**, 457 (2018).
- [25] E. Brown, H. Zhang, N. A. Forman, B. W. Maynor, D. E. Betts, J. M. DeSimone, and H. M. Jaeger, Shear thickening and jamming in densely packed suspensions of different particle shapes, *Phys. Rev. E* **84**, 031408 (2011).
- [26] N. M. James, H. Xue, M. Goyal, and H. M. Jaeger, Controlling shear jamming in dense suspensions via the particle aspect ratio, *Soft Matter* **15**, 3649 (2019).
- [27] B. M. Guy, C. Ness, M. Hermes, L. J. Sawiak, J. Sun, and W. C. K. Poon, Testing the Wyart-Cates model for non-Brownian shear thickening using bidisperse suspensions, *Soft Matter* **16**, 229 (2020).
- [28] S. Majumdar, I. R. Peters, E. Han, and H. M. Jaeger, Dynamic shear jamming in dense granular suspensions under extension, *Phys. Rev. E* **95**, 012603 (2017).
- [29] I. R. Peters, J. M. Amundson, R. Cassotto, M. Fahnestock, K. N. Darnell, M. Truffer, and W. W. Zhang, Dynamic jamming of iceberg-choked fjords, *Geophys. Res. Lett.* **42**, 1122 (2015).
- [30] J. J. S. Jerome, N. Vandenberghe, and Y. Forterre, Unifying Impacts in Granular Matter from Quicksand to Cornstarch, *Phys. Rev. Lett.* **117**, 098003 (2016).
- [31] R. Maharjan, E. O'Reilly, T. Postiglione, N. Klimenko, and E. Brown, Relation between dilation and stress fluctuations in discontinuous shear thickening suspensions, *Phys. Rev. E* **103**, 012603 (2021).
- [32] E. E. Bischoff White, M. Chellamuthu, and J. P. Rothstein, Extensional rheology of a shear-thickening cornstarch and water suspension, *Rheol. Acta* **49**, 119 (2010).
- [33] M. Smith, R. Besseling, M. Cates, and V. Bertola, Dilatancy in the flow and fracture of stretched colloidal suspensions, *Nat. Commun.* **1**, 114 (2010).
- [34] M. Roché, E. Myftiu, M. C. Johnston, P. Kim, and H. A. Stone, Dynamic Fracture of Nonglassy Suspensions, *Phys. Rev. Lett.* **110**, 148304 (2013).
- [35] B. Allen, B. Sokol, S. Mukhopadhyay, R. Maharjan, and E. Brown, System-spanning dynamically jammed region in response to impact of cornstarch and water suspensions, *Phys. Rev. E* **97**, 052603 (2018).
- [36] J. Garside and M. R. Al-Dibouni, Velocity-voidage relationships for fluidization and sedimentation in solid-liquid systems, *Ind. Eng. Chem. Process Des. Dev.* **16**, 206 (1977).
- [37] J. Richardson and W. Zaki, Sedimentation and fluidisation: Part 1, *Chem. Eng. Res. Des.* **75**, S82 (1997).
- [38] S. Nemat-Nasser, *Plasticity: A Treatise on Finite Deformation of Heterogeneous Inelastic Materials* (Cambridge University Press, Cambridge, UK, 2004).
- [39] See Supplemental Material at <http://link.aps.org/supplemental/10.1103/PhysRevFluids.6.103301> for example movie snippets.
- [40] doi:10.5258/SOTON/D1962.